

## GALAXY PROPERTIES AT THE FAINT END OF THE HI MASS FUNCTION

KRISTEN B. W. MCQUINN,<sup>1</sup> ANJANA K. TELIDEVARA,<sup>2,3</sup> JACKSON FUSON,<sup>4</sup> ELIZABETH A. K. ADAMS,<sup>5,6</sup>  
JOHN M. CANNON,<sup>4</sup> EVAN D. SKILLMAN,<sup>3</sup> ANDREW E. DOLPHIN,<sup>7,8</sup> MARTHA P. HAYNES,<sup>9</sup> KATHERINE L. RHODE,<sup>10</sup>  
JOHN. J. SALZER,<sup>10</sup> RICCARDO GIOVANELLI,<sup>9</sup> AND ALEX J. R. GORDON<sup>4</sup>

<sup>1</sup>*Rutgers University, Department of Physics and Astronomy, 136 Frelinghuysen Road, Piscataway, NJ 08854, USA*

<sup>2</sup>*University of Texas at Austin, McDonald Observatory, 2515 Speedway, Stop C1400, Austin, Texas 78712, USA*

<sup>3</sup>*University of Minnesota, Minnesota Institute for Astrophysics, School of Physics and Astronomy, 116 Church Street, S.E., Minneapolis, MN 55455, USA*

<sup>4</sup>*Department of Physics and Astronomy, Macalester College, Saint Paul, MN 55105, USA*

<sup>5</sup>*ASTRON, The Netherlands Institute for Radio Astronomy, Oude Hoogeveensedijk 4, 7991 PD, Dwingeloo, The Netherlands*

<sup>6</sup>*Kapteyn Astronomical Institute, University of Groningen Postbus 800, 9700 AV Groningen, The Netherlands*

<sup>7</sup>*Raytheon Company, 1151 E. Hermans Road, Tucson, AZ 85756, USA*

<sup>8</sup>*University of Arizona, Steward Observatory, 933 North Cherry Avenue, Tucson, AZ 85721, USA*

<sup>9</sup>*Center for Astrophysics and Planetary Science, Space Sciences Building, Cornell University, Ithaca, NY 14853, USA*

<sup>10</sup>*Department of Astronomy, Indiana University, 727 East Third Street, Bloomington, IN 47405, USA*

### ABSTRACT

The Survey of HI in Extremely Low-mass Dwarfs (SHIELD) includes a volumetrically complete sample of 82 gas-rich dwarfs with  $M_{HI} \lesssim 10^{7.2} M_{\odot}$  selected from the ALFALFA survey. We are obtaining extensive follow-up observations of the SHIELD galaxies to study their gas, stellar, and chemical content, and to better understand galaxy evolution at the faint end of the HI mass function. Here, we investigate the properties of 30 SHIELD galaxies using Hubble Space Telescope imaging of their resolved stars and Westerbork Synthesis Radio Telescope observations of their neutral hydrogen. We measure tip of the red giant branch (TRGB) distances, star formation activity, and gas properties. The TRGB distances are up to  $4\times$  greater than estimates from flow models, highlighting the importance of velocity-independent distance indicators in the nearby universe. The SHIELD galaxies are in underdense regions, with 23% located in voids; one galaxy appears paired with a more massive dwarf. We quantify galaxy properties at low masses including stellar and HI masses, SFRs, sSFRs, SFEs, birthrate parameters, and gas fractions. The lowest mass systems lie below the mass thresholds where stellar mass assembly is predicted to be impacted by reionization. Even so, we find the star formation properties follow the same trends as higher mass gas-rich systems, albeit with a different normalization. The HI disks are small ( $\langle r \rangle < 0.7$  kpc) making it difficult to measure the HI rotation using standard techniques; we develop a new methodology and report the velocity extent, and its associated spatial extent, with robust uncertainties.

*Keywords:* galaxies: dwarf irregular galaxies – galaxies: star formation history – stars: Hertzsprung-Russell diagram – galaxies: distances – galaxies: galaxy rotation

### 1. INTRODUCTION

#### 1.1. *On the Cosmological Importance of Extremely Low-mass Galaxies*

In the current paradigm, galaxies are formed hierarchically, and the numbers of galaxies increase as galaxy stellar mass decreases. Large surveys support this

framework and the galaxy mass function (as traced by stellar luminosity) continues to rise at lower masses. At small enough masses, galaxy counts should eventually decline (e.g., due to the combined loss of baryons from blow-out, ram pressure stripping, tidal interactions, and reionization at the earliest epochs). Identifying this turnover in the galaxy luminosity function and its environmental dependence would place strong constraints on the limits of structure formation in the early universe.

The present-day masses of ‘turnover galaxies’, while a subject of debate, are expected to be low ( $M_* \lesssim 10^{7.5} M_\odot$ ) with shallow potentials and correspondingly low rotation velocities ( $V_{\text{rot}} \lesssim 30 \text{ km s}^{-1}$ ; e.g., Rees 1986; Gnedin 2000; Hoesft et al. 2006; Okamoto et al. 2008, and references therein). The existence of *gas-rich* galaxies with such very shallow potential wells poses interesting puzzles for the  $\Lambda$ CDM paradigm and for our understanding of baryon physics (Bullock & Boylan-Kolchin 2017, and references therein). Star formation activates feedback mechanisms that result in gas loss via superwinds (McQuinn et al. 2019b). Metagalactic UV radiation inhibits gas accretion and cooling. A hot IGM should vaporize a small, unshielded cold gas mass within less than a Hubble time (e.g., Ikeuchi & Ostriker 1986; Rees 1986; Mac Low & Ferrara 1999; Ferrara & Tolstoy 2000; Hoesft et al. 2006). How gas is retained in these very low mass systems is under debate; it might depend on the protection provided by a shielding envelope of warm, ionized gas, as shown in the models of Sternberg et al. (2002), and/or environment, i.e., low-mass galaxies can be found outside the immediate vicinity of dense coronal gas. There is also speculation about whether such systems will have different properties than more massive dwarfs due to the impacts of the same internal and external processes, or if their properties will simply extend well-established galaxy scaling relations.

In sum, there are numerous open questions about galaxies at the faint end of the luminosity function, particularly for gas-rich systems, including (i) their number counts, (ii) their overall properties, and (iii) the ability for at least some systems with such shallow potentials to retain their gas until the present day.

### 1.2. Finding Extremely Low-Mass Gas-Rich Galaxies

Observationally, a main challenge to counting and characterizing very low-mass galaxies and, subsequently, testing the various predictions, has been finding large enough samples of these systems. As one moves to lower and lower masses, the systems host fewer stars and thus are intrinsically faint in the optical, infrared, and ultraviolet regimes with correspondingly low surface brightnesses. There are numerous, on-going efforts to search for low-mass galaxies including, for example, searches for ultra-faint dwarfs within the Local Group (e.g., the Dark Energy Survey; Drlica-Wagner et al. 2020), searches for low surface brightness and satellite galaxies outside the Local Group but within the Local Volume (e.g., Smercina et al. 2018; Greco et al. 2018; Carlsten et al. 2020), and searches for satellites of more massive galaxies outside the Local Volume in a statis-

tical sample of galaxies (the SAGA Survey; Geha et al. 2017; Mao et al. 2020).

As our interests lie in the faint end of the galaxy luminosity function populated with *gas-rich, star-forming galaxies*, rather than searching for the faint emission from their stellar populations, we take a different approach and search for galaxies via their neutral hydrogen. The Arecibo Legacy Fast ALFA (ALFALFA) survey (Giovannelli et al. 2005; Haynes et al. 2011) is an extragalactic survey that mapped neutral hydrogen (HI) over  $\sim 7000 \text{ deg}^2$  of high Galactic latitude sky in the nearby universe. ALFALFA was designed to populate the faint end of the HI mass function with an HI mass detection limit of  $\sim 10^6 M_\odot$  in the local universe and  $10^{9.5}$  at the edge of the survey volume at  $z \sim 0.06$ . Because of the higher sensitivity of the ALFALFA survey, low-mass galaxies can be detected over a volume  $4\times$  larger than the HI Parkes All Sky Survey (HIPASS Barnes et al. 2001; Meyer et al. 2004), despite the smaller areal coverage (Jones et al. 2018). The full ALFALFA catalog includes over 30,000 extragalactic HI sources (Haynes et al. 2018).

From the rich ALFALFA catalog of HI sources, we selected low-mass systems in the Local Volume ( $D \lesssim 4-11 \text{ Mpc}$ ; see §2 for specific criteria) that also have stellar counterparts identified in optical imaging of SDSS for detailed follow-up in the Survey of HI in Extremely Low-mass Dwarfs (SHIELD; Cannon et al. 2011). The full SHIELD sample includes 82 galaxies, many of which were discovered by the ALFALFA survey, and span the range of halo masses over which the interesting transition from the cosmic baryon fraction ( $f_b$ ) value of  $\sim 0.16$  to  $< 0.01$  takes place (see, e.g., Hoesft et al. 2006; McGaugh & Wolf 2010). Here, we present results for 30 galaxies in the SHIELD sample, including incorporating results from the initial study of 12 systems (hereafter the SHIELD I galaxies) and new results for an additional 18 systems (hereafter the SHIELD II galaxies).

As the SHIELD galaxies are an HI selected sample, the expectation is that the majority of the systems will be located in a field environment based on the low frequency of gas-rich satellites of the Milky Way and M 31. While a full exploration of the environment of the SHIELD sample requires accurate distances to all 82 galaxies, the present results for the first 30 systems allow us to produce initial statistics regarding whether the systems are in under-dense environments and the distances to their nearest neighbors.

Using the SHIELD galaxies, we work toward quantifying the physical properties in very low-mass galaxies at the faint end of the HI mass function, understanding their environments, and testing galaxy formation and



evolution theories. We begin in §2 with a comparison to some of the existing surveys of low-mass galaxies, including an exploration of HI mass detections as a function of distance in the Local Volume. We present new HST optical imaging for 18 galaxies and WSRT HI observations for 16 galaxies, including introducing a new approach for measuring the velocity and extent of HI from velocity fields with limited spatial sampling in §3, measurements of the TRGB distances to the galaxies in §4, and measurements of their star formation properties in §5. Using the TRGB distances, we explore the galaxies' surrounding neighborhoods in §6. Galaxy properties at the faint end of the HI mass function, including stellar and gas content and star formation properties of the SHIELD galaxies are discussed in §7, with comparisons to results in the literature on other very low-mass galaxies. Our conclusions are presented in §8. Finally, in the Appendix, we include an atlas of the HST imaging (Appendix A), an atlas of the WSRT HI data (Appendix B), and details on our new methodology for measuring the rotational motion and spatial extent of the HI in very low-mass galaxies (Appendix C).

## 2. OVERVIEW OF SHIELD AND COMPARISON WITH OTHER SURVEYS

### 2.1. The SHIELD program

The SHIELD sample consist of 82 galaxies selected from the ALFALFA catalog that met the following criteria: (i) low gas masses ( $\log(M_{\text{HI}}/M_{\odot}) < 7.2$ ) based on the HI line fluxes and distance estimates from the flow model of Masters (2005), (ii) narrow HI line widths (HI FWHM  $< 65 \text{ km s}^{-1}$ ), which selected against massive but HI-deficient galaxies, (iii) optically identified counterparts in SDSS imaging, and (iv) distance estimates within  $\sim 11 \text{ Mpc}$ , which ensured the galaxies are sufficiently close for detailed analysis while eliminating the closest and most well-studied gas-rich dwarfs. Note that a few galaxies within  $\sim 4 \text{ Mpc}$  met these criteria but were not included in the SHIELD sample as they were part of existing HI selected surveys.

Results for the first 12 SHIELD galaxies (SHIELD I galaxies; Cannon et al. 2011) include (i) measuring tip of the red giant branch (TRGB) distances (McQuinn et al. 2014), (ii) characterizing their star formation properties from color-magnitude diagrams (CMD; McQuinn et al. 2015b), (iii) deriving their gas kinematics from a combination of B, C, and D configuration data from the Very Large Array (VLA; see McNichols et al. 2016, for details), (iv) comparing their star formation and gas properties (Teich et al. 2016), and (v) measuring their oxygen abundances (Haurberg et al. 2015).

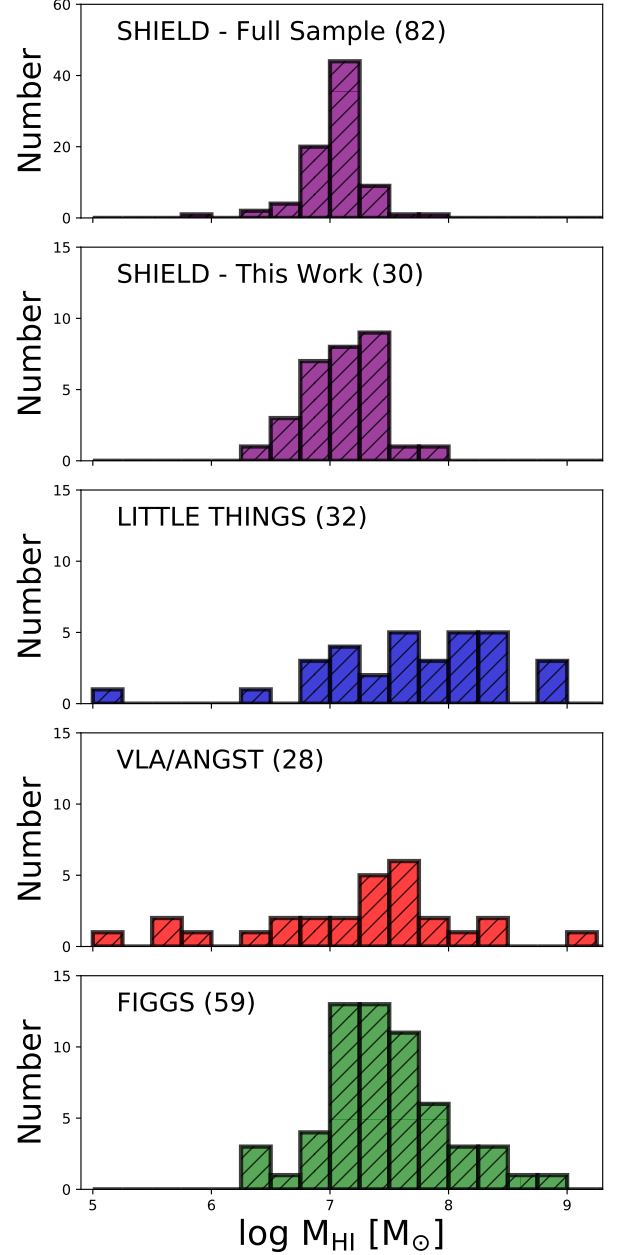


**Figure 1.** From top to bottom: The HI mass distribution of galaxies in the full SHIELD survey, the subset of SHIELD galaxies included in this work (the SHIELD I and II samples), and three other surveys of low-mass galaxies including LITTLE THINGS galaxies, the VLA/ANGST survey, and the FIGGS survey. Both LITTLE THINGS and FIGGS are HI selected surveys, while VLA/ANGST is an HI follow-up on the optically selected galaxies in ANGST (Dalcanton et al. 2009). We include the galaxies for which we have compiled stellar masses; the parenthetical numbers represent the total galaxy counts in each histogram. Collectively, these surveys provide a basis to characterize galaxy properties at the faint end of the HI mass function. See, also, Figure 2.

Here, we expand the analysis from 12 to 30 galaxies, adding new observations of the resolved stellar populations from HST and of the H I from WSRT of 18 galaxies (SHIELD II galaxies). With the combined 30 galaxies from the SHIELD I and II samples, and expanding on the work of previous surveys (e.g., FIGGS, VLA/ANGST, LITTLE THINGS; Begum et al. 2008; Ott et al. 2012; Hunter et al. 2012, respectively), we begin to quantify the properties of galaxies at the faint end of the galaxy H I mass function with statistical confidence. Follow-up analysis will place the SHIELD galaxies in the context of the Baryonic Tully-Fisher Relation (BTFR; K. McQuinn et al. in preparation).

## 2.2. Comparison of SHIELD with Other Surveys of Gas-Rich Low Mass Galaxies

Figure 1 shows the number distribution of the H I masses for the full SHIELD sample (top panel) based on the ALFALFA H I fluxes and adopting the Virgo-centric flow model distances from Masters (2005) (see §4.2). The number shown parenthetically is the number of galaxies in the histogram. The second panel shows the distribution of the SHIELD galaxies presented in this work (i.e., SHIELD I and II samples), after adopting the more robust TRGB distance measured in the present work (see §4). Note that the ordinate range shown for the SHIELD I and II galaxies is a factor of four smaller than for the full SHIELD sample shown in the top panel. The majority of the galaxies span a narrow H I mass range of  $10^{6.5} - 10^{7.5} M_{\odot}$ , which is mainly due to the upper mass limit imposed in our selection criteria and the growing incompleteness of the ALFALFA catalog at lower masses.

As our main goal is to characterize the properties of galaxies in the nearby universe at the faint end of the H I mass function, we also present samples from three existing surveys focused on dwarfs galaxies in the subsequent panels in Figure 1. Specifically, we include the data from the LITTLE THINGS survey (Hunter et al. 2012), the VLA/ANGST survey (Ott et al. 2012), and the FIGGS survey (Begum et al. 2008). We excluded galaxies from VLA/ANGST that are classified as early-type galaxies or were not detected in H I. Note that the numbers for each survey, shown parenthetically, represent the galaxies for which we have compiled stellar masses; the total number of galaxies in each survey is slightly higher. While not a complete census of Local Volume gas-rich dwarfs,<sup>1</sup> these surveys are the largest detailed studies

of H I bearing low-mass galaxies in the Northern Hemisphere and, thus, help characterize galaxy properties over a larger mass range and with improved statistics, complementing the SHIELD results.

## 2.3. H I Masses as a Function of Distance

The distribution of H I masses as a function of distance for SHIELD and the three other surveys described in §2 is presented in Figure 2. We include not only the SHIELD I and II samples, but the remaining 52 galaxies from SHIELD (labelled SHIELD III which includes the all SHIELD galaxies not presented in detail in this work). Collectively, these galaxies provide a statistical population of gas-rich dwarfs down to  $M_{\text{HI}} \sim 10^{6.5} M_{\odot}$ , distributed over  $\sim 12$  Mpc. Galaxies below this mass threshold have almost exclusively been detected within a few Mpc.

All the surveys shown are Northern hemisphere surveys, which allows us to calculate an approximate number density. Selecting systems in the mass range  $6.5 \leq \log(M_{\text{HI}}/M_{\odot}) \leq 7.5$ , the number density within 4, 8 and 12 Mpc is 0.25, 0.06, and  $0.04 \text{ Mpc}^{-3}$  respectively. Focusing on just the SHIELD sample, the volume probed is based on a solid angle of 6630 square degrees (Jones et al. 2018), much smaller than the Northern hemisphere, over a distance range of 4-12 Mpc. The resulting number density is  $0.02 \text{ Mpc}^{-3}$ .

As one moves out in distance, the number counts of galaxies at a given mass should increase as the cube of the distance. While this is not necessarily true over the volume probed by the ALFALFA footprint within  $\sim 12$  Mpc due to cosmic variance, the decreasing number density from 0.25, 0.06, 0.04, to  $0.02 \text{ Mpc}^{-3}$  as a function of distance is, in large part, a result of the growing incompleteness below  $M_{\text{HI}} \sim 10^7 M_{\odot}$  due to the sensitivity limits of the various surveys. The distribution and number density of galaxies in Figure 2 highlights the incomplete nature of our current studies of gas-rich, low-mass galaxies, and the rich opportunity for future H I surveys with even greater sensitivity using new facilities such as the Square Kilometer Array (SKA) and its precursors.

## 3. THE SHIELD OBSERVATIONS AND DATA PROCESSING

Our new observations consist of HST images of the resolved stars, which are used to measure distances, stellar masses, and recent SFRs, and WSRT images of the neutral hydrogen, which are used to characterize the gas distributions and kinematics. The HST data processing and analysis follow the same approach used for the SHIELD I galaxies. For more detailed descriptions, we

<sup>1</sup> Note that in particular the LITTLE THINGS galaxies were selected to sample a broad range of galaxies properties and did not attempt to be volumetrically complete.

Table 1. Stellar Properties

	Galactic	F814W <sub>TRGB</sub>	Distance	Distance	Internal	log	$\langle\text{SFR}\rangle_{\text{life}}$	$\langle\text{SFR}\rangle_{200\text{ Myr}}$	a	1-b/a	PA	Optical
Galaxy	A <sub>F606W</sub>	ML	Modulus		A <sub>V</sub>	(M <sub>*</sub> /M <sub>⊙</sub> )	×10 <sup>−3</sup>	×10 <sup>−3</sup>				Diameter
	(mag)	(mag)	(mag)	(Mpc)	(mag)		(M <sub>⊙</sub> yr <sup>−1</sup> )	(M <sub>⊙</sub> yr <sup>−1</sup> )	(″)		(°)	(kpc)
(1)	(2)	(3)	(4)	(5)	(6)	(7)	(8)	(9)	(10)	(11)	(12)	(13)
SHIELD I Galaxies												
AGC 110482	0.23	25.38 ± 0.05	29.47 ± 0.05	7.82 ± 0.21	0.00	7.40 <sup>+0.25</sup> <sub>−0.21</sub>	5.17 <sup>+2.99</sup> <sub>−2.47</sub>	5.72 <sup>+2.69</sup> <sub>−3.66</sub>	37	0.30	15	2.8
AGC 111164	0.14	24.45 ± 0.02	28.54 ± 0.03	5.11 ± 0.07	0.00	6.54 <sup>+0.12</sup> <sub>−0.14</sub>	0.72 <sup>+0.20</sup> <sub>−0.23</sub>	0.39 <sup>+0.21</sup> <sub>−0.21</sub>	60	0.40	6	3.0
AGC 111946	0.20	25.69 <sup>+0.04</sup> <sub>−0.06</sub>	29.78 <sup>+0.05</sup> <sub>−0.06</sub>	9.02 <sup>+0.20</sup> <sub>−0.29</sub>	0.00	6.81 <sup>+0.20</sup> <sub>−0.24</sub>	1.34 <sup>+0.61</sup> <sub>−0.73</sub>	2.17 <sup>+0.66</sup> <sub>−1.20</sub>	27	0.56	6	2.4
AGC 111977	0.17	24.81 <sup>+0.03</sup> <sub>−0.02</sub>	28.88 <sup>+0.04</sup> <sub>−0.03</sub>	5.96 <sup>+0.11</sup> <sub>−0.09</sub>	0.00	7.12 <sup>+0.16</sup> <sub>−0.17</sub>	2.74 <sup>+0.99</sup> <sub>−1.09</sub>	1.81 <sup>+1.04</sup> <sub>−0.93</sub>	70	0.47	30	4.0
AGC 112521	0.15	25.00 ± 0.05	29.09 ± 0.05	6.58 ± 0.18	0.00	6.47 <sup>+0.18</sup> <sub>−0.19</sub>	0.61 <sup>+0.26</sup> <sub>−0.27</sub>	0.52 <sup>+0.37</sup> <sub>−0.38</sub>	32	0.38	18	2.0
AGC 174585	0.10	25.39 <sup>+0.05</sup> <sub>−0.04</sub>	29.49 ± 0.05	7.89 <sup>+0.21</sup> <sub>−0.17</sub>	0.00	6.56 <sup>+0.09</sup> <sub>−0.16</sub>	0.75 <sup>+0.16</sup> <sub>−0.27</sub>	1.57 <sup>+0.52</sup> <sub>−0.76</sub>	23	0.26	347	1.8
AGC 174605	0.06	26.09 ± 0.05	30.19 ± 0.05	10.89 ± 0.28	0.00	7.10 <sup>+0.63</sup> <sub>−0.20</sub>	2.60 <sup>+3.75</sup> <sub>−1.21</sub>	3.09 <sup>+1.96</sup> <sub>−1.35</sub>	26	0.19	0	2.7
AGC 182595	0.10	25.68 ± 0.06	29.78 ± 0.06	9.02 ± 0.28	0.00	7.41 <sup>+0.15</sup> <sub>−0.25</sub>	5.28 <sup>+1.88</sup> <sub>−3.01</sub>	3.95 <sup>+1.65</sup> <sub>−1.81</sub>	52	0.19	0	4.5
AGC 731457	0.07	26.13 <sup>+0.03</sup> <sub>−0.02</sub>	30.23 <sup>+0.04</sup> <sub>−0.03</sub>	11.13 <sup>+0.20</sup> <sub>−0.16</sub>	0.00	7.82 <sup>+0.03</sup> <sub>−0.33</sub>	13.5 <sup>+0.88</sup> <sub>−10.3</sub>	13.1 <sup>+0.48</sup> <sub>−6.23</sub>	37	0.38	0	4.0
AGC 748778	0.16	24.95 <sup>+0.04</sup> <sub>−0.05</sub>	29.05 ± 0.05	6.46 <sup>+0.14</sup> <sub>−0.17</sub>	0.00	6.13 <sup>+0.11</sup> <sub>−0.21</sub>	0.28 <sup>+0.07</sup> <sub>−0.14</sub>	0.62 <sup>+0.24</sup> <sub>−0.39</sub>	27	0.11	0	1.7
AGC 749237	0.05	26.24 <sup>+0.03</sup> <sub>−0.02</sub>	30.33 <sup>+0.04</sup> <sub>−0.03</sub>	11.62 <sup>+0.20</sup> <sub>−0.16</sub>	0.00	7.40 <sup>+0.39</sup> <sub>−0.31</sub>	5.26 <sup>+4.75</sup> <sub>−3.78</sub>	8.29 <sup>+3.99</sup> <sub>−2.99</sub>	38	0.45	44	4.3
AGC 749241	0.04	24.64 <sup>+0.06</sup> <sub>−0.05</sub>	28.75 <sup>+0.06</sup> <sub>−0.05</sub>	5.62 <sup>+0.17</sup> <sub>−0.14</sub>	0.00	6.26 <sup>+0.15</sup> <sub>−0.13</sub>	0.38 <sup>+0.13</sup> <sub>−0.11</sub>	0.50 <sup>+0.24</sup> <sub>−0.27</sub>	27	0.07	0	1.5
SHIELD II Galaxies												
AGC 102728	0.11	26.45 <sup>+0.11</sup> <sub>−0.09</sub>	30.47 <sup>+0.11</sup> <sub>−0.09</sub>	12.41 <sup>+0.64</sup> <sub>−0.53</sub>	0.00	6.58 <sup>+0.15</sup> <sub>−0.32</sub>	0.79 <sup>+0.28</sup> <sub>−0.58</sub>	1.07 <sup>+0.37</sup> <sub>−0.44</sub>	9.5	0.48	283	1.1
AGC 123352	0.61	26.17 ± 0.05	29.94 ± 0.05	9.72 ± 0.25	0.00	6.71 <sup>+0.11</sup> <sub>−0.23</sub>	1.06 <sup>+0.26</sup> <sub>−0.56</sub>	1.62 <sup>+0.35</sup> <sub>−0.82</sub>	8.2	0.43	137	1.3
AGC 198507	0.08	26.11 <sup>+0.18</sup> <sub>−0.24</sub>	30.20 <sup>+0.18</sup> <sub>−0.24</sub>	10.94 <sup>+0.91</sup> <sub>−1.22</sub>	0.00	6.27 <sup>+0.09</sup> <sub>−0.25</sub>	0.38 <sup>+0.08</sup> <sub>−0.22</sub>	1.95 <sup>+0.54</sup> <sub>−0.71</sub>	6.9	0.11	97	0.7
AGC 198508	0.09	25.91 <sup>+0.08</sup> <sub>−0.07</sub>	29.96 <sup>+0.08</sup> <sub>−0.07</sub>	9.83 <sup>+0.38</sup> <sub>−0.33</sub>	0.00	6.74 <sup>+0.14</sup> <sub>−0.21</sub>	1.14 <sup>+0.37</sup> <sub>−0.56</sub>	2.39 <sup>+0.55</sup> <sub>−1.20</sub>	17	0.39	67	1.6
AGC 198691	0.03	...	30.4 <sup>+0.31</sup> <sub>−0.60</sub>	12.1 <sup>+1.7</sup> <sub>−3.4</sub>	...	5.74 <sup>+0.13</sup> <sub>−0.26</sub>	0.04 <sup>+0.01</sup> <sub>−0.02</sub>	...	6.8	0.61	80	0.8
AGC 200232	0.07	26.06 <sup>+0.01</sup> <sub>−0.02</sub>	30.12 <sup>+0.02</sup> <sub>−0.03</sub>	10.57 <sup>+0.12</sup> <sub>−0.15</sub>	0.00	7.65 <sup>+0.19</sup> <sub>−0.26</sub>	9.30 <sup>+4.01</sup> <sub>−5.58</sub>	4.51 <sup>+1.90</sup> <sub>−1.91</sub>	28	0.18	95	2.9
AGC 205590	0.0 5	26.04 ± 0.11	30.12 ± 0.11	10.55 ± 0.55	0.00	7.08 <sup>+0.37</sup> <sub>−0.36</sub>	2.50 <sup>+0.21</sup> <sub>−2.05</sub>	3.20 <sup>+0.17</sup> <sub>−2.39</sub>	16	0.14	330	1.3
AGC 223231	0.03	25.5 ± 0.05	29.60 ± 0.05	8.32 ± 0.21	0.00	6.81 <sup>+0.05</sup> <sub>−0.24</sub>	1.33 <sup>+0.15</sup> <sub>−0.75</sub>	2.77 <sup>+1.07</sup> <sub>−1.16</sub>	19	0.18	220	1.5
AGC 223254	0.05	24.98 <sup>+0.02</sup> <sub>−0.01</sub>	29.03 <sup>+0.03</sup> <sub>−0.02</sub>	6.41 <sup>+0.09</sup> <sub>−0.07</sub>	0.00	6.84 <sup>+0.09</sup> <sub>−0.15</sub>	1.42 <sup>+0.28</sup> <sub>−0.49</sub>	2.41 <sup>+0.54</sup> <sub>−1.11</sub>	43	0.10	13	2.7
AGC 229053	0.07	26.42 <sup>+0.04</sup> <sub>−0.02</sub>	30.48 <sup>+0.05</sup> <sub>−0.03</sub>	12.50 <sup>+0.26</sup> <sub>−0.17</sub>	0.00	7.39 <sup>+0.21</sup> <sub>−0.29</sub>	5.12 <sup>+2.47</sup> <sub>−3.42</sub>	2.19 <sup>+0.83</sup> <sub>−0.74</sub>	41	0.54	104	5.0
AGC 229379	0.04	25.28 ± 0.08	29.38 ± 0.08	7.51 ± 0.29	0.00	6.42 <sup>+0.14</sup> <sub>−0.20</sub>	0.54 <sup>+0.17</sup> <sub>−0.24</sub>	0.44 <sup>+0.19</sup> <sub>−0.35</sub>	15	0.04	151	1.1
AGC 238890	0.03	24.58 ± 0.02	28.64 ± 0.03	5.34 ± 0.07	0.15	7.12 <sup>+0.07</sup> <sub>−0.19</sub>	2.73 <sup>+0.47</sup> <sub>−1.22</sub>	0.57 <sup>+0.17</sup> <sub>−0.30</sub>	53	0.33	85	2.7
AGC 731448	0.07	25.92 ± 0.08	30.00 ± 0.08	10.01 ± 0.38	0.00	7.44 <sup>+0.15</sup> <sub>−0.26</sub>	4.45 <sup>+1.57</sup> <sub>−2.70</sub>	4.13 <sup>+1.31</sup> <sub>−1.49</sub>	19	0.38	145	1.8
AGC 731921	0.05	26.23 ± 0.05	30.31 ± 0.05	11.51 ± 0.29	0.00	7.66 <sup>+0.06</sup> <sub>−0.32</sub>	9.45 <sup>+1.32</sup> <sub>−7.06</sub>	5.07 <sup>+0.41</sup> <sub>−2.46</sub>	24	0.15	12	2.7
AGC 739005	0.11	25.64 <sup>+0.04</sup> <sub>−0.05</sub>	29.68 ± 0.05	8.63 <sup>+0.18</sup> <sub>−0.22</sub>	0.00	7.11 <sup>+0.06</sup> <sub>−0.26</sub>	2.64 <sup>+0.38</sup> <sub>−1.60</sub>	3.23 <sup>+1.19</sup> <sub>−1.96</sub>	27	0.43	125	2.3
AGC 740112	0.11	26.08 <sup>+0.07</sup> <sub>−0.10</sub>	30.12 <sup>+0.07</sup> <sub>−0.10</sub>	10.56 <sup>+0.36</sup> <sub>−0.50</sub>	0.00	7.60 <sup>+0.10</sup> <sub>−0.34</sub>	8.16 <sup>+1.88</sup> <sub>−6.39</sub>	0.57 <sup>+0.27</sup> <sub>−0.56</sub>	36	0.55	102	3.6
AGC 742601	0.09	25.18 ± 0.05	29.22 ± 0.05	7.00 ± 0.18	0.10	6.46 <sup>+0.05</sup> <sub>−0.22</sub>	0.60 <sup>+0.08</sup> <sub>−0.30</sub>	0.71 <sup>+0.20</sup> <sub>−0.45</sub>	17	0.34	193	1.1
AGC 747826	0.05	26.13 <sup>+0.04</sup> <sub>−0.05</sub>	30.20 ± 0.05	10.94 <sup>+0.28</sup> <sub>−0.23</sub>	0.00	7.44 <sup>+0.11</sup> <sub>−0.35</sub>	5.74 <sup>+1.44</sup> <sub>−4.64</sub>	2.01 <sup>+0.38</sup> <sub>−1.29</sub>	23	0.32	5	2.4

NOTE—Col. 2 lists the Galactic extinction from the dust maps of [Schlegel et al. \(1998\)](#) with recalibration from [Schlafly & Finkbeiner \(2011\)](#); values for SHIELD I galaxies are updated from [McQuinn et al. \(2014\)](#). Cols. 3, 4, and 5 list the TRGB identified in the F814W luminosity function of the resolved stars, the distance modulus calculating from the TRGB mag using the calibration of [Rizzi et al. \(2007\)](#), and the corresponding distance respectively. Col. 6 is the internal extinction estimating by fitting the CMD with stellar evolution libraries. Col. 7, 8, and 9 are the present-day stellar mass, average lifetime SFR, and average recent SFR over the past 200 Myr derived from the CMDs using the PARSEC stellar library. Cols. 10, 11, and 12 are the semi-major axis, ellipticity, and position angle determined from the resolved stars. Col. 13 is the optical diameter of the stellar disk estimated from the semi-major axis and adopting our distances. See text for details. The distance to AGC 198691 is from [McQuinn et al. \(2020\)](#); due to the sparseness of the CMD, no recent SFR for this galaxy was measured from the CMD-fitting technique.

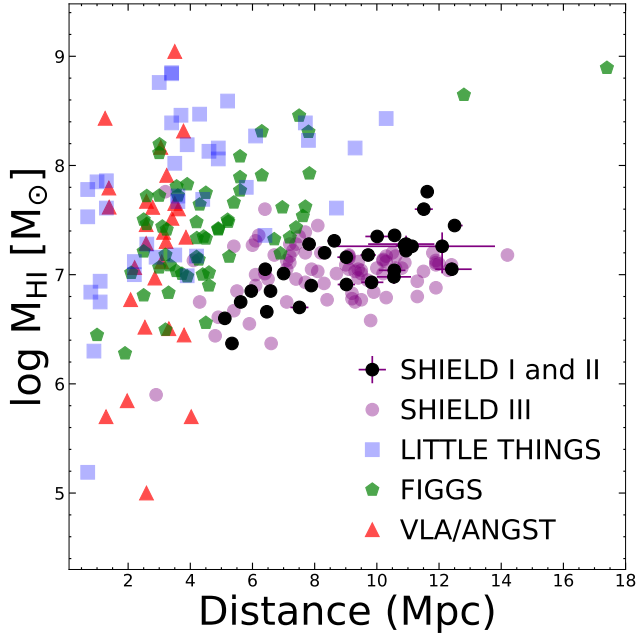


**Figure 2.**  $\log(M_{\text{HI}}/M_{\odot})$  vs. Distance for SHIELD and three other surveys of low-mass galaxies. The SHIELD I and II samples studied in detail in the present work are shown with black circles and purple uncertainties; the remainder of the SHIELD sample (labelled as SHIELD III) are shown with transparent purple circles. VLA/ANGST includes optically selected galaxies within  $\sim 4$  Mpc by design. LITTLE THINGS extends to larger HI masses than VLA/ANGST and spans a larger range in distance. The FIGGS galaxies are on average slightly more massive than the SHIELD galaxies (see also Figure 1) and less distant.

refer the reader to [McQuinn et al. \(2014\)](#) for HST data processing and TRGB distance methodology, and to [McQuinn et al. \(2015b\)](#) for measurements of the star formation rates from CMD-fitting. The WSRT data processing and estimates of the HI kinematics are described in full below.

### 3.1. Hubble Space Telescope Observations of the Stars

Table 1 lists the 18 SHIELD II galaxies for which we have obtained new observations from HST (PID HST-GO-13750). All galaxies were observed for a single orbit using the Advanced Camera for Surveys (ACS) Wide Field Channel ([Ford et al. 1998](#)). Integration times were divided between the F606W (1000 s) and F814W filters ( $\sim 1200$  s) with CRSPILT = 2 to allow for the removal of cosmic-rays. The images were processed by the standard HST pipeline. The data from each filter were cosmic-ray cleaned, aligned, and median combined at the native resolution of the ACS instrument using the HST Drizzlepac v2.0 software ([Gonzaga 2012](#)).

Color images of four galaxies are shown in the left panels of Figure 3, created with the F606W (blue), F814W (red), and an average of the two images (green). An atlas of the HST data for the remainder of the SHIELD II sample is presented in Appendix A. In order to highlight the low surface brightness features in the galaxies, we apply an arcsinh stretch to the images. The fields of view encompass thrice the optical major diameter or  $6 \times a$ , where  $a$  is the semi-major axis listed in Table 1; the exception is AGC 238890 which has a smaller field of view of twice the optical diameter. Using the same approach adopted for SHIELD I galaxies studied in [McQuinn et al. \(2014\)](#), we determined the optical semi-major axes of the galaxies by iteratively examining color-magnitude diagrams (CMDs) of the stars with different elliptical parameters and in concentric annuli. We describe this in more detail in §3.2.

Similarly to the SHIELD I sample, the galaxies have irregular morphologies and their stellar concentrations range from compact (AGC 189691) to more distributed (AGC 731921). The physical scales, gauged by the markers in the lower right of each panel, are small, with nearly all of the stellar disks less than 2 kpc in diameter. Knots of recent star formation are apparent in much of the sample, although only 12 of the 18 galaxies are detected in H $\alpha$  (M. Shepley et al. in preparation).

### 3.2. Photometry of the Resolved Stars

We analyzed the resolved stars in the HST images using the same methodology applied in [McQuinn et al. \(2014\)](#). Briefly, point-spread function (PSF) photometry was performed with the software package HSTphot using the ACS-specific module ([Dolphin 2000](#)). As input to the photometry, we used the pipeline processed, cosmic-ray rejected CRJ.FITS images. These files were also pipeline corrected for charge transfer efficiency (CTE) non-linearities caused by space radiation damage to the ACS instrument (e.g., [Anderson & Bedin 2010](#); [Massey et al. 2010](#)).

The photometry results were filtered to exclude: objects with large errors (error flag  $\geq 4$ ); cosmic rays and background galaxies ( $V_{\text{sharp}} + I_{\text{sharp}})^2 > 0.75$  and objects in crowded regions ( $V_{\text{crowd}} + I_{\text{crowd}} > 0.8$ , which have higher photometric uncertainties. The F814W photometry was filtered for sources with a signal-to-noise ratio (S/N)  $> 4$ , ensuring only sources with high fidelity measurements are used as input to the TRGB and star formation measurements. The F606W photometry was filtered twice. First, for the purposes of creating clean CMDs and measuring the star formation rates in the galaxies, we made a cut on sources with the more stringent F606W S/N  $> 4$ . Second, for the purpose of



measuring the TRGB from the F814W luminosity function, we made a more liberal cut with F606W  $S/N > 2$ . This more generous  $S/N$  cut in F606W avoids excluding sources with a low  $S/N$  in the F606W filter but higher  $S/N$  in the F814W photometry. This is particularly important given the photometric depth of the data and prevents completeness effects in the F606W data from removing high quality point sources in the F814W data needed for the TRGB measurements.

Finally, we applied spatial cuts to the photometry. The SHIELD galaxies typically subtend only a small fraction of the ACS field of view. Therefore, spatial cuts are used to reduce contamination of background galaxies and foreground stars that were not already rejected by our quality cuts. We used the same approach employed for the SHIELD I galaxies, given in detail in [McQuinn et al. \(2014\)](#). Briefly, the spatial extent of the galaxies was determined by plotting the CMD of well-recovered point sources within concentric ellipses centered on the galaxy with position angles and ellipticities that approximately matched the distribution of point sources. Starting with the inner ellipse, the CMD is dominated by stars in the galaxies. As the axes of the ellipses are increased, the stellar density in the galaxy begins to drop until more contaminating point sources are added to the CMD than bona fide stars in the galaxy. We determine that we have reached the edge of the main stellar population detected when the CMD of sources from the outer annulus matches the approximate number and distribution of sources from a field region in the image. Table 1 lists these empirically determined ellipticities, position angles, and semi-major axes.

Artificial star tests were performed on the images to measure the completeness limits of the data using the same photometry package. The stars were injected in an area encompassing each galaxy using the geometric parameters in Table 1, but over a slightly larger area. We filtered the artificial star tests using the same quality cuts applied to the photometry.

The CMDs for 4 of the SHIELD II galaxies are shown in the middle panels of Figure 3, based on the photometry with  $S/N$  cuts of  $4\sigma$  in both filters. We plot in grey the point sources with lower  $S/N$  in the F606W image that were used in distance determinations. Representative uncertainties per magnitude are shown which include uncertainties from the photometry and the completeness tests. The depths of the CMDs approximately correspond to the 50% completeness limits measured by the artificial star tests. An atlas of the CMDs for the remainder of the SHIELD II sample is presented in Appendix A.

The CMDs have well-populated red giant branch (RGB) sequences, which allows for a robust distance determination. The exception is AGC 198691 (a.k.a. the Leoncino dwarf; [Hirschauer et al. 2016](#)); for this galaxy, deeper HST observations were obtained separately in HST-GO-15423. We adopt the distance and galaxy properties reported from this program in [McQuinn et al. \(2020\)](#) and discuss these results in more detail below. The CMDs of the galaxies also ubiquitously host upper main sequence and helium burning stars, indicative of recent star formation. There are, however, notable differences in the number of these young stars between systems. For example, AGC 223231 has well-defined upper main and helium burning sequences, whereas in AGC 747826 these sequences are comparatively underpopulated. We investigate the differences in recent star formation properties in more detail in §5.

### 3.3. WSRT Observations of the HI

The HI data for SHIELD II were obtained using the WSRT (Program Code 14A–018). Table 2 lists the number of antennas available for the observations, rms noise per channel, beam sizes, position angles of the restoring beams, and physical resolutions of the HI observations. WSRT acquisition began in December 2013, and was completed in September 2014. The observing campaign coincided with the WSRT APERTIF project upgrade which removed three of the fourteen antennas from use. Additional antennas were unavailable for various maintenance reasons for many of the observations. As a result, the observations were obtained with a smaller collecting area than WSRT has when it is fully operational, and consequently have lower sensitivity. All WSRT observations are 12-hour tracks. For two sources, we were unable to detect the system in the WSRT interferometric data. For AGC 731448, the observations were truncated due to a high priority transient, and, thus, the beam is heavily skewed and the data uninterpretable. For AGC 740112 the source was not detected at a level above the background noise<sup>2</sup>.

The WSRT HI data reduction was performed using MIRIAD. Radio Frequency Interference (RFI) was excised by hand. Bad baselines and broken antennas were likewise flagged and the data were corrected for system temperature. A combination of 3C48, 3C147, and 3C286 calibrators were observed at the beginning and end of the WSRT observations. As the telescope has excellent

<sup>2</sup> The observations were obtained with only eight of fourteen total antennas, which may account for the non-detection. AGC 740112 is detected in the new VLA observations; J. M. Cannon et al. in preparation.

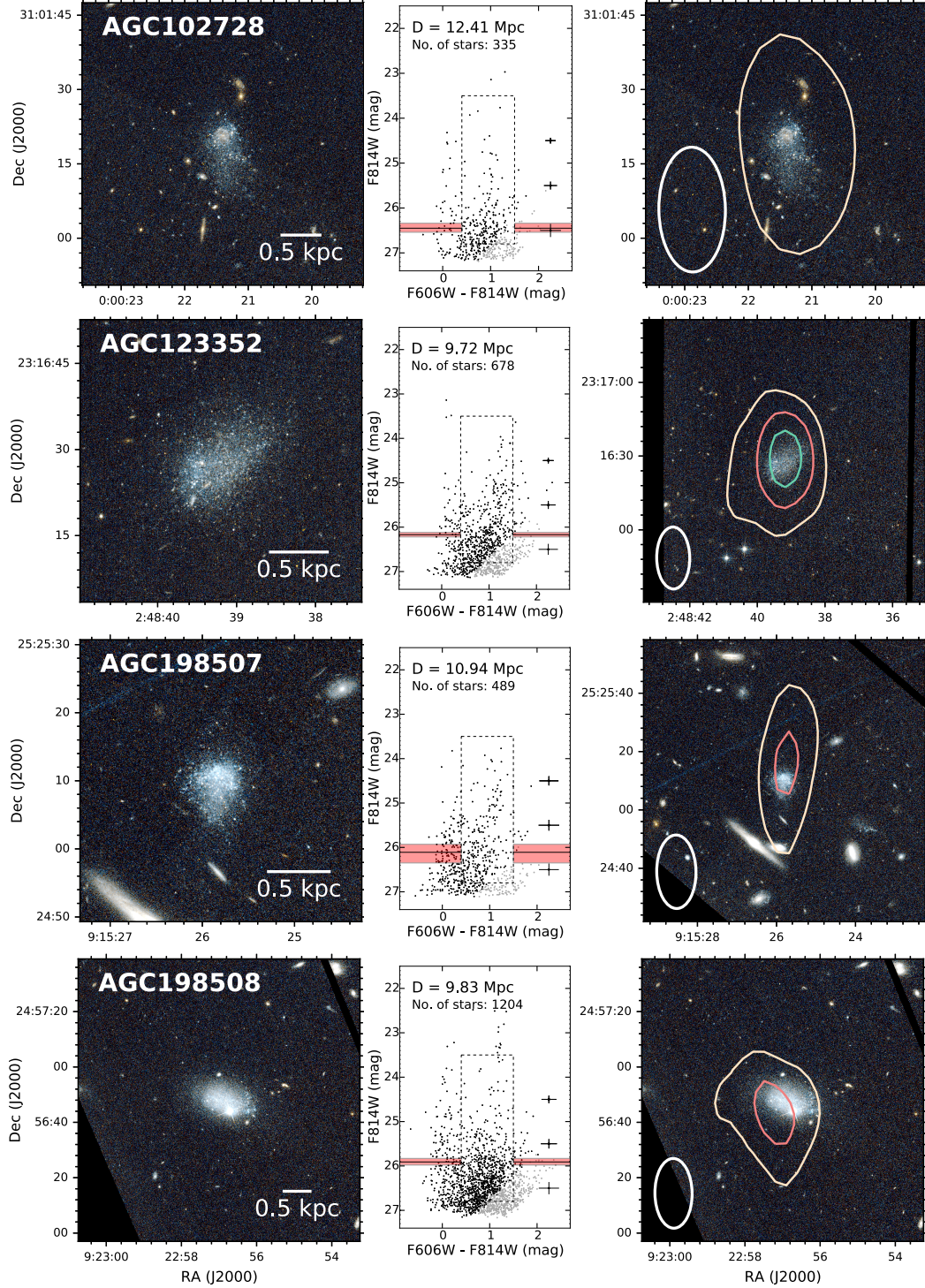


**Figure 3.** HST optical images, CMDs, and HST optical images with WSRT HI contours overlaid for AGC 102728, AGC 123352, AGC 198507, AGC 198508. Left: HST optical images of the galaxies with North up and East left. The physical scales of the galaxies are marked in the lower right. The galaxies range from highly compact (e.g., AGC 198691; see Figure 9) to more extended (e.g., AGC 123352). Middle: CMDs of the resolved stars from the HST imaging. Grey points at the bottom of CMDs are point sources with low S/N in the F606W filter that were used in the distance determinations. The dashed boxes highlight the region of the CMD used for the TRGB measurement. The black horizontal lines mark the measured TRGBs and the shaded red regions represent the measurement uncertainties. Distances to the galaxies and total number of stars in each CMD are listed at the top for each galaxy. Right: HST optical images with WSRT HI contours overlaid at HI column densities corresponding to  $4$ ,  $8$ , and  $12\sigma$  in tan, red, and green, respectively. The fields of view in the right panels are the same as in the left panel except for AGC 123352, AGC 198507, and AGC 198691 (Figure 9) which encompass fields  $7\times$  the optical diameter to show the more extended HI distributions. The WSRT beam size is shown in the lower left for each galaxy. Note the elongated beam results in somewhat elongated HI contours and, thus, care must be taken when interpreting the apparent HI morphologies of the galaxies. An atlas of the HST data for the remainder of the SHIELD II sample is presented in Appendix A.

**Table 2.** Summary of WSRT Observations

Galaxy	RA	Dec	No. of	rms noise	Beam size	$B_{PA}$	$S_{HI}$	Resolution
	(J2000)	(J2000)	Antennas	(mJy Bm <sup>-1</sup> )	(" × ")	(°)	Jy km s <sup>-1</sup>	(kpc)
(1)	(2)	(3)	(4)	(5)	(6)	(7)	(8)	(9)
SHIELD II Galaxies								
AGC 102728	00:00:21.4	+31:01:19	8	1.64	43.17×19.41	0.5	0.20 ± 0.02	1.74
AGC 123352	02:48:39.2	+23:16:28	9	1.23	35.30×12.85	0.1	0.66 ± 0.07	1.00
AGC 198507	09:15:25.8	+25:25:10	10	1.48	33.90×13.32	0.3	0.58 ± 0.06	1.13
AGC 198508	09:22:57.0	+24:56:48	9	1.18	35.64×13.40	0.3	0.46 ± 0.05	1.04
AGC 198691	09:43:32.4	+33:26:58	8	1.43	22.86×11.97	-1.2	0.32 ± 0.03	1.13
AGC 200232	10:17:26.4	+29:22:11	11	1.17	27.32×13.81	0.3	0.82 ± 0.08	1.00
AGC 205590	10:00:36.5	+30:32:10	11	1.16	26.37×13.76	0.4	0.36 ± 0.04	0.97
AGC 223231	12:22:52.7	+33:49:43	9	1.33	23.51×13.49	0.6	0.83 ± 0.08	0.72
AGC 223254	12:28:05.0	+22:17:27	9	1.18	39.60×13.78	0.3	0.89 ± 0.08	0.73
AGC 229053	12:18:15.5	+25:34:05	10	1.20	31.36×13.56	-1.0	0.81 ± 0.08	1.25
AGC 229379	12:30:34.3	+23:12:19	10	2.42	37.08×13.91	-0.1	0.25 ± 0.03	0.83
AGC 238890	13:32:30.3	+25:07:24	10	1.36	29.77×12.35	-0.2	0.25 ± 0.03	0.50
AGC 731448	10:23:45.0	+27:06:39	...	...	...	...	...	...
AGC 731921	12:05:34.3	+28:13:56	10	1.34	26.64×12.65	0.4	1.14 ± 0.12	0.89
AGC 739005	09:13:39.0	+19:37:07	10	1.32	39.29×12.16	-0.1	1.02 ± 0.10	1.22
AGC 740112	10:49:55.4	+23:04:06	8	1.37	30.03×11.85	1.2	...	...
AGC 742601	12:49:36.9	+21:55:05	10	1.40	34.02×12.35	0.0	0.73 ± 0.07	0.86
AGC 747826	12:07:50.0	+31:33:07	9	1.24	25.19×13.46	0.7	0.61 ± 0.06	0.94

NOTE—Coordinates are based on the optical emission. From the WSRT data, we list the number of dishes available for each observation, rms noise per channel, angular beam size, position angle of the restoring beam ( $B_{PA}$ ) used in calculating the effective beam, total integrated flux density, and the resolution based on the effective radius of a circle with the same area as an ellipse with semi-major and semi-minor axes defined by the beam size and adopting the distances in Table 1. Each HI data cube has a velocity resolution of 4.1 km s<sup>-1</sup> per channel. Observations for AGC 731448 were interrupted; AGC 740112 is a non-detection.

phase stability, targets are followed from the moment they peek above the horizon until the moment they set. A phase-only self-calibration was performed, using the `self-cal` task, to correct for changes in the phases during the observation.

A first-order continuum subtraction was performed for all datasets using the task `uvlin`. The ALFALFA spectra were used to determine the velocity range that should be excluded from fitting for the continuum. Dirty image cubes were created with a 4 channel binning, corresponding to a velocity resolution of  $4.1 \text{ km s}^{-1}$ . These cubes, along with the ALFALFA spectra, were used to determine the velocity extent of each source. A single channel image over this entire velocity extent was created. The emission from the galaxy was selected and cleaned in an iterative fashion, with the mask growing as more emission was cleaned. A final mask was created by smoothing to a resolution of  $60'' \times 30''$ , clipping at the  $2\text{-}\sigma$  level, and masking to only consider central emission associated with the source. This global clean mask was then applied to all channels in the original cube determined to have emission and a deep cleaning to  $0.5\text{-}\sigma$  was performed. A spectrum was then extracted using this global clean mask and the channel range considered for cleaning was compared to the extent of emission seen in this spectrum. If needed, the channel range considered for cleaning was changed to match the extent of emission seen in the spectrum. This approach optimizes the detection and cleaning of low S/N emission, following the approach of [Adams & Oosterloo \(2018\)](#).

### 3.4. HI Moment Zero and Moment One Maps

Once the clean cubes were finalized, moment zero and moment one maps were created over the channel range used for cleaning. Each moment zero map, or total HI intensity map, was clipped at the  $2\text{-}\sigma$  level to derive a spectrum over the region where emission was directly detected. These moment zero maps were then used to derive HI column density maps assuming optically thin emission. The moment zero maps were also clipped at the  $3\text{-}\sigma$  level and used as a mask on the moment one maps, or velocity fields, so that only areas of significant emission were included.

An example HI intensity map and HI velocity field for AGC 731921 are shown in the right panels of the Figure 4; an atlas of the HI data for the remainder of the SHIELD II sample is presented in Appendix B. In the top right panel of Figure 4, we show the HI column density maps with contours corresponding to the 4, 8, and  $12\text{-}\sigma$  levels of emission in tan, red, and green colors respectively, matching the HI column density contours overplotted in the HST images in Figure 3 and in Ap-

pendix A. In the bottom right panel, we show the velocity field. Also shown are the beam size, physical scale of the image, and the location of the position-velocity (PV) slice used in the kinematics analysis below. The position angle of the PV slice is provided in Table 3. Note that, while the elongated elliptical beam of WSRT observations prevents a detailed analysis of the HI morphology, the overall extent of the HI is accurately represented. The neutral gas is more extended than the detected stellar disks in all cases. A few galaxies do have East-West velocity gradients that are resolved by the beam sizes; we make note of this for the individual systems in the HI image atlas in Appendix B.

Figure 4 also shows example spectra in the top left panel, along with the channel range used for cleaning, for AGC 731921. Three spectra are shown for comparison: a WSRT spectrum based on the global masks used for cleaning, a WSRT spectrum based on clipping the moment zero map at the  $2\text{-}\sigma$  level, and the ALFALFA spectrum; similar comparisons for the remaining galaxies with WSRT detections are presented in Appendix B. Both the spectrum from the global clean mask and the  $2\text{-}\sigma$  moment zero mask were used to derive the flux of the galaxies. The fluxes derived from spectra using the clean masks are significantly larger than those derived using the moment zero  $2\text{-}\sigma$  mask as the global clean mask was spatially smoothed and includes real emission that is at the level of the noise. We report the fluxes from the global clean mask in Table 2, assuming a 10% uncertainty from the flux scale accuracy. The fluxes are generally smaller than but consistent with the fluxes reported from the ALFALFA survey using the single-dish measurements; we list these values in Table 3. The exception is AGC 198508 where noise peaks in the global WSRT spectrum artificially inflate the flux.

### 3.5. Measurements of the HI Kinematics

While the moment one maps provide information on the gas kinematics, the small spatial extent of the HI and the less clearly defined rotation in the gas make it difficult to extract the kinematic information using methods traditionally applied to more massive galaxies (i.e., fitting tilted ring models using codes such as <sup>3D</sup>BAROLO to derive rotation curves; [Di Teodoro & Fraternali 2015](#)). Instead, we measure the rotational velocities and spatial extent of the HI by analyzing spatially-resolved PV slices through the cubes, at the angle of greatest velocity spread.

An example PV diagram is shown in the bottom left of Figure 4 for AGC 731921; Appendix B includes PV diagrams for the rest of the sample. Contours are overlaid at the 2, 3, 5,  $7\text{-}\sigma$  level of the rms values measured



**Table 3.** HI Properties

Galaxy	V <sub>21</sub>	W <sub>50</sub>	S <sub>HI</sub>	PA	<i>i</i>	D <sub>PV</sub>	R <sub>PV</sub>	V <sub>PV</sub>	V <sub>rot</sub>	log (M <sub>HI</sub> /M <sub>⊙</sub> )
	(km s <sup>-1</sup> )	(km s <sup>-1</sup> )	(Jy km s <sup>-1</sup> )	(°)	(°)	(″)	(kpc)	(km s <sup>-1</sup> )	(km s <sup>-1</sup> )	
(1)	(2)	(3)	(4)	(5)	(6)	(7)	(8)	(9)	(10)	(11)
SHIELD I Galaxies										
AGC 110482	357 ± 1	30 ± 2	1.33 ± 0.04	84	55 ± 5	21 ± 4	0.4 ± 0.1	15 ± 4	9 ± 3	7.28 ± 0.03
AGC 111164	163 ± 3	27 ± 6	0.65 ± 0.04	326	50 ± 5	20 ± 1	0.3 ± 0.1	20 ± 2	13 ± 2	6.60 ± 0.03
AGC 111946	367 ± 2	21 ± 3	0.76 ± 0.03	285	62 ± 5	...	...	...	...	7.16 ± 0.03
AGC 111977	207 ± 2	26 ± 4	0.85 ± 0.05	29	59 ± 5	...	...	...	...	6.85 ± 0.03
AGC 112521	274 ± 1	26 ± 1	0.69 ± 0.04	180	55 ± 5	23 ± 2	0.4 ± 0.1	14 ± 1	9 ± 1	6.85 ± 0.03
AGC 174585	356 ± 3	21 ± 6	0.54 ± 0.04	290	42 ± 5	...	...	...	...	6.90 ± 0.04
AGC 174605	351 ± 1	24 ± 2	0.66 ± 0.04	90	19 ± 10	10 ± 7	0.3 ± 0.2	10 ± 7	15 ± 13	7.27 ± 0.03
AGC 182595	398 ± 2	20 ± 4	0.42 ± 0.03	74	39 ± 10	...	...	...	...	6.91 ± 0.04
AGC 731457	454 ± 3	36 ± 6	0.62 ± 0.04	18	34 ± 10	...	...	...	...	7.26 ± 0.03
AGC 748778	258 ± 2	16 ± 3	0.46 ± 0.04	21	40 ± 15	...	...	...	...	6.66 ± 0.04
AGC 749237	372 ± 1	65 ± 2	1.80 ± 0.05	254	54 ± 5	38 ± 4	1.1 ± 0.1	47 ± 6	29 ± 4	7.76 ± 0.02
AGC 749241	451 ± 1	18 ± 2	0.76 ± 0.03	301	45 ± 20	...	...	...	...	6.75 ± 0.03
SHIELD II Galaxies										
AGC 102728	566 ± 3	21 ± 6	0.31 ± 0.03	36	30 ± 15	...	...	...	...	7.05 ± 0.06
AGC 123352	467 ± 3	25 ± 5	0.68 ± 0.03	64	50 ± 5	...	...	...	...	7.18 ± 0.03
AGC 198507	502 ± 2	37 ± 3	0.68 ± 0.04	246	35 ± 10	...	...	...	...	7.28 <sup>+0.08</sup> <sub>-0.10</sub>
AGC 198508	519 ± 4	29 ± 7	0.37 ± 0.04	223	50 ± 5	...	...	...	...	6.93 ± 0.06
AGC 198691	514 ± 3	33 ± 5	0.53 ± 0.04	10	45 ± 5	...	...	...	...	7.26 <sup>+0.13</sup> <sub>-0.25</sub>
AGC 200232	450 ± 6	49 ± 11	0.86 ± 0.05	0	40 ± 5	...	...	...	...	7.36 ± 0.03
AGC 205590	494 ± 4	29 ± 7	0.36 ± 0.04	345	40 ± 5	...	...	...	...	6.98 ± 0.07
AGC 223231	571 ± 2	19 ± 3	0.97 ± 0.04	104	50 ± 5	...	...	...	...	7.20 ± 0.03
AGC 223254	603 ± 2	19 ± 3	1.16 ± 0.04	80	45 ± 10	...	...	...	...	7.05 ± 0.02
AGC 229053	425 ± 2	40 ± 4	0.77 ± 0.04	190	50 ± 5	34 ± 3	1.0 ± 0.1	29 ± 3	19 ± 2	7.45 ± 0.03
AGC 229379	624 ± 3	22 ± 6	0.38 ± 0.04	40	20 ± 10	...	...	...	...	6.70 ± 0.06
AGC 238890	360 ± 3	20 ± 6	0.35 ± 0.04	180	45 ± 5	...	...	...	...	6.37 ± 0.06
AGC 731448	540 ± 2	39 ± 4	0.94 ± 0.04	...	55 ± 5	...	...	...	...	7.35 ± 0.04
AGC 731921	504 ± 2	62 ± 3	1.26 ± 0.04	110	40 ± 5	53 ± 4	1.5 ± 0.1	46 ± 3	36 ± 4	7.60 ± 0.03
AGC 739005	433 ± 2	46 ± 3	1.16 ± 0.05	308	55 ± 5	38 ± 2	0.8 ± 0.1	37 ± 2	23 ± 2	7.31 ± 0.03
AGC 740112	609 ± 5	37 ± 9	0.42 ± 0.04	...	55 ± 10	...	...	...	...	7.04 <sup>+0.05</sup> <sub>-0.06</sub>
AGC 742601	539 ± 2	27 ± 3	0.88 ± 0.06	266	45 ± 5	24 ± 2	0.4 ± 0.1	13 ± 1	9 ± 1	7.01 ± 0.04
AGC 747826	558 ± 2	31 ± 4	0.59 ± 0.03	204	50 ± 5	25 ± 2	0.7 ± 0.1	10 ± 3	7 ± 2	7.22 ± 0.03

NOTE—Heliocentric velocity of the H I (V<sub>21</sub>), the velocity width of the H I line profile measured at 50% of its peak value (W<sub>50</sub>), and integrated H I flux density (S<sub>HI</sub>) values are from the ALFALFA catalog (Haynes et al. 2018). The statistical uncertainty on V<sub>21</sub> is adopted as half the error on the width W<sub>50</sub> tabulated in Col. 3 (Haynes et al. 2018). *i* is the inclination angle of the source determined from the *HST* optical imaging. D<sub>PV</sub> is the maximum spatial extent in arcsec determined from the PV diagrams using with our new methodology, and R<sub>PV</sub> is the radius in kpc based on  $\frac{1}{2}$ D<sub>PV</sub> and adopting the TRGB distances. V<sub>PV</sub> is full maximum velocity extent measured from the PV diagrams, also determined using our new methodology, and V<sub>rot</sub> is  $\frac{1}{2}$ V<sub>PV</sub>/sin *i* (i.e., half the full velocity extent corrected for inclination). H I masses are based on adopting the TRGB distance in Table 1. See text for more details on all parameters.

from the PV slice in an off-source region, after spatially smoothing with a 1-pixel boxcar. All PV slices have a width of 50″, which is larger than the major axis beam size in all cases. This ensures that the slices are representative of the bulk projected motion and are less sensitive to the absolute slice position or PA than a narrower (e.g., a few pixels wide) slice would be.

Here, we introduce a new methodology that enables the robust determination of the maximum velocity de-

tected in the H I data for each system and its spatial extent, including associated uncertainty estimates, from PV diagrams. This new method is an improvement over the technique originally used for the SHIELD I galaxies in McNichols et al. (2016) where the maximum velocity of the H I gas was empirically estimated based on the maximum identified extent of the emission in the PV diagram.

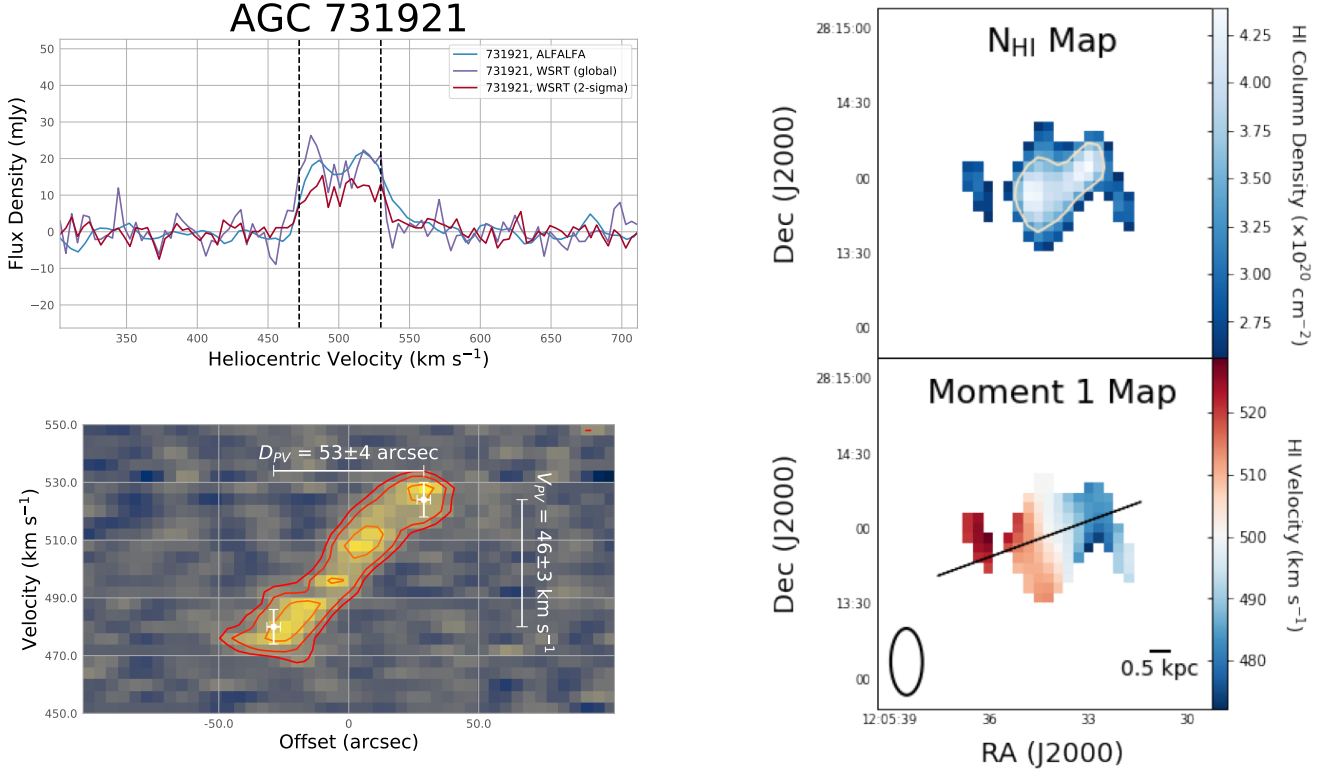


**Figure 4.** Clockwise from the top left: Comparison of the WSRT global spectrum and the WSRT spectrum clipped at the 2- $\sigma$  level with the ALFALFA spectrum for AGC 731921. The velocity range used in cleaning the spectrum is marked with vertical dashed lines. Top right: Example of the HI column density map for AGC 731921 with HI column density contours overlaid at the 4, 8, 12- $\sigma$  detection levels based on the rms listed in Table 2. Bottom right: the HI velocity field map. The identified major axis of rotation passing through the kinematic center used for making a position–velocity (PV) diagram is marked as a black line. Physical scale marker and HI beam size are also shown. The field of view in each panel is  $3\times$  the optical diameter. Bottom left: Example of spatially resolved PV diagram across the major axes of AGC 731921 taken along the black line shown in the velocity field with contours overlaid at 2, 3, 5, 7- $\sigma$  detection levels based on the rms measured off-source in the PV slice. The spatial extent of the HI ( $D_{PV}$ ) and the range in velocity measured from the PV slice ( $V_{PV}$ ), marked in the figure, as well as the position angle (PA) measured east of north of the PV slice, are listed in Table 3. An atlas of the HI data for the full SHIELD II sample is presented in Appendix B.

Briefly, the PV diagram is sliced in orthogonal bins and the maximum range in velocity is determined by taking bins along the spatial position offset and fitting the velocity profile with a Gaussian. The difference between the center velocity of the Gaussians in the two furthest spatial bins is the maximum range in velocity, which we label  $V_{PV}$ . The maximum spatial extent is obtained in an analogous way by taking bins along the velocity axis and fitting a Gaussian to the spatial dimension. The difference between the minimum and maximum values fit with a Gaussian is taken as the total extent, or diameter, which we label  $D_{PV}$ . The returned velocity and spatial extent values are only considered meaningful if the spatial extent is larger than the effective beam of the PV diagram.

Figure 4 shows an example PV slice with the maximum velocity value and spatial extent found by this

methodology for a galaxy that is well-resolved with high S/N data. There is a projected velocity gradient from north to south with a magnitude of  $46\pm3$  km s $^{-1}$  over an extent of  $53\pm4''$ . The source is resolved by the HI beam so this gradient can be interpreted as projected rotation. The velocities appears to reach a plateau in the outer edges of the detected HI, suggesting the data are reaching the flat part of the rotation curve.

This new methodology and its application to both the SHIELD I and SHIELD II galaxies is described in detail in Appendix C. We also present PV slices and their derived maximum velocities and extents in Appendices B and C for SHIELD II and SHIELD I, respectively. Note that the velocity and spatial extent could not be measured for all galaxies; Appendix C also describes the criteria we used to apply our new methodology and which galaxies did not meet our criteria.

It is important to note that these velocity measurements represent estimates of the bulk motion of the gas, and while they are good indicators of the rotational velocities, they are not as robust as values determined from kinematic modeling. J. Fuson et al. (in preparation) will present a detailed comparison of this approach to rotation curve modeling based on higher angular resolution observations.

Final rotational velocity values were calculated using half the difference between the maximum and minimum velocity of gas we could attribute to the source, corrected for inclination (i.e.,  $V_{\text{rot}} = \frac{1}{2} V_{\text{PV}} / \sin i$ ). The inclinations were derived from the HST optical images. Specifically, the F814W image was edited by hand to remove obvious foreground and background contaminants, smoothed, and then fit with an ellipse to determine the axial ratio and position angle. This follows the approach used for the SHIELD I sample in Teich et al. (2016). The values of  $i$ ,  $D_{\text{PV}}$ ,  $V_{\text{PV}}$ , and  $V_{\text{rot}}$ , as well as the radius  $R_{\text{PV}} = \frac{1}{2} D_{\text{PV}}$  converted to a physical scale in kpc, are listed in Table 3. We also include our updated values for the SHIELD I galaxies in Table 3, and, for completeness, we list the HI heliocentric velocities, line widths, and fluxes as reported in the ALFALFA catalog (Haynes et al. 2018). The HI masses for the galaxies were calculated based on the measured fluxes from the ALFALFA survey and adopting our TRGB distances (see §4).

For nearly all the galaxies, the rotational velocities measured are still on the rising part of the rotation curve in the inner radii of the galaxies. Thus, our values of  $V_{\text{rot}}$  are lower limits for the full rotational velocity of the galaxies which can only be determined at larger radii on the flat part of a rotation curve. In addition, we have not accounted for the velocity dispersion in the gas nor have we made any asymmetric drift corrections; given the low rotational velocities measured in the galaxies, the inclusion of dispersion and asymmetric drift may impact the rotational velocities significantly. These corrections, as well as analysis of the rotational velocities, dynamical masses, and the stellar and gas content of the sample will be the focus of a future publication on the BTFR (K. McQuinn et al. in preparation).

#### 4. TIP OF THE RED GIANT BRANCH DISTANCES

##### 4.1. TRGB Measurements

The RGB sequence of stars is well-defined in the CMDs of SHIELD II galaxies, enabling robust distances to be measured using the TRGB method<sup>3</sup>. The TRGB is

a primary, Population II distance indicator that uses the predictable luminosity peak of low-mass stars just before the helium flash as a standard candle (e.g., Lee et al. 1993; Sakai et al. 1996). The luminosity of stars as they approach the TRGB has some dependency on the metal content of the stars, and, to a lesser extent, the stellar age (or mass), due to bolometric corrections. This dependency is modest in the I-band (or I-band equivalent filters such as the F814W), compared with other wavelengths (e.g., Salaris & Girardi 2005; McQuinn et al. 2019a), and can be accounted for in calibrations as discussed below. High-resolution imaging from HST has revolutionized our ability to efficiently measure high-quality distances using the TRGB method out to  $\sim 15$  Mpc (e.g., Tully et al. 2013); since the TRGB is brighter in the infrared, JWST has the potential to reach larger distances than HST, more efficiently (Beaton et al. 2018; McQuinn et al. 2019a).

TRGB distances are determined by identifying the discontinuity in the extinction-corrected F814W luminosity function from stars pre-selected from a CMD to be in the RGB region and then translating that luminosity to a distance. The dashed boxes in the CMDs of Figure 3 and of Appendix A highlight the stars used in our distance determinations; all boxes encompass the same color range ( $0.4 < F606W - F814W < 1.5$ ) with luminosity limits individually chosen for each galaxy to include stars that are just above the limit of detection to  $\sim 2$  mag brighter than the TRGB.

We measure the F814W luminosity function discontinuity corresponding to the TRGB using a maximum likelihood (ML) technique, following the same approach employed for the SHIELD I galaxies in McQuinn et al. (2014). Briefly, the ML approach fits a parametric RGB luminosity function to the observed F814W luminosity function. The probability estimation takes into account the photometric error distribution and completeness from the artificial star tests (Makarov et al. 2006), which is particularly important in data with limited photometric depth. The assumed theoretical form of the luminosity function is:

$$P = \begin{cases} 10^{(A*(m-m_{\text{TRGB}})+B)}, & \text{if } m - m_{\text{TRGB}} \geq 0 \quad (1a) \\ 10^{(C*(m-m_{\text{TRGB}}))}, & \text{if } m - m_{\text{TRGB}} < 0 \quad (1b) \end{cases}$$

where A, B, and C are treated as free parameters in the majority of fits, and A and C have normal priors of 0.30 ( $\sigma = 0.07$ ) and 0.30 ( $\sigma = 0.2$ ), respectively. In six cases (AGC 205590, AGC 229053, AGC 229379, AGC 238890, AGC 731448, AGC 747826), the data did not suitably constrain the three parameters and A and

<sup>3</sup> The exception, as noted above, is AGC 198691, which has a TRGB distance measurement from deeper HST data presented in McQuinn et al. (2020).

C were held fixed to their priors. The range in solutions returning  $\log(P)$  within 0.5 of the maximum gives the uncertainty. We also independently checked that the ML results agreed within the uncertainties with the simpler approach of using a Sobel filter. The benefit of the ML technique is the more robustly quantified uncertainties (see [McQuinn et al. 2014](#), for details). The best-fits to the data are shown as a solid black line in the CMDs of Figure 3 and of Appendix A with the measurement uncertainties shaded in red.

The measured TRGB luminosities in the F814W filter were calibrated to an absolute distance scale by applying the modest, color-based correction for metallicity and zero-point for ACS-specific filters from [Rizzi et al. \(2007\)](#):

$$M_{F814W}^{ACS} = -4.06(\pm 0.02) + 0.20(\pm 0.01) \cdot [(F606W - F814W) - 1.23] \quad (2)$$

where  $F606W - F814W$  is the average color of the TRGB stars. The distances using the [Rizzi et al. \(2007\)](#) calibration are also consistent with the newer calibration from [Jang & Lee \(2017\)](#).<sup>4</sup>

The measured distances for the SHIELD II galaxies range from  $\sim 5$  to  $\sim 12$  Mpc. Table 1 lists the apparent magnitude of the identified discontinuity in the F814W luminosity function before correcting for extinction, the calculated distance moduli, and the corresponding distance for each galaxy. The uncertainties are based on adding in quadrature the uncertainties from the ML technique, photometry, artificial star tests, and the TRGB calibration. For AGC 198691, we list the distance determined from [McQuinn et al. \(2020\)](#). For completeness, Table 1 also lists the values for the SHIELD I sample from [McQuinn et al. \(2014\)](#).

#### 4.2. Comparison with flow model Distances

Figure 5 compares our measured TRGB distances with the Virgo-centric flow model distances adopting the reported minimum uncertainties of  $\pm 3$  Mpc ([Masters 2005](#)). With two exceptions, the TRGB distances to the SHIELD galaxies are farther than the original ALFALFA estimates based on the flow model. The larger number of under-estimated distances is due to our sample selection criteria and the Malmquist bias. Because we imposed an HI upper mass cutoff, galaxies with flow model distances larger than their true distance would

<sup>4</sup> The [Jang & Lee \(2017\)](#) calibration includes a higher-order correction that has a greater impact on more metal-rich stellar populations typical of spiral galaxies.

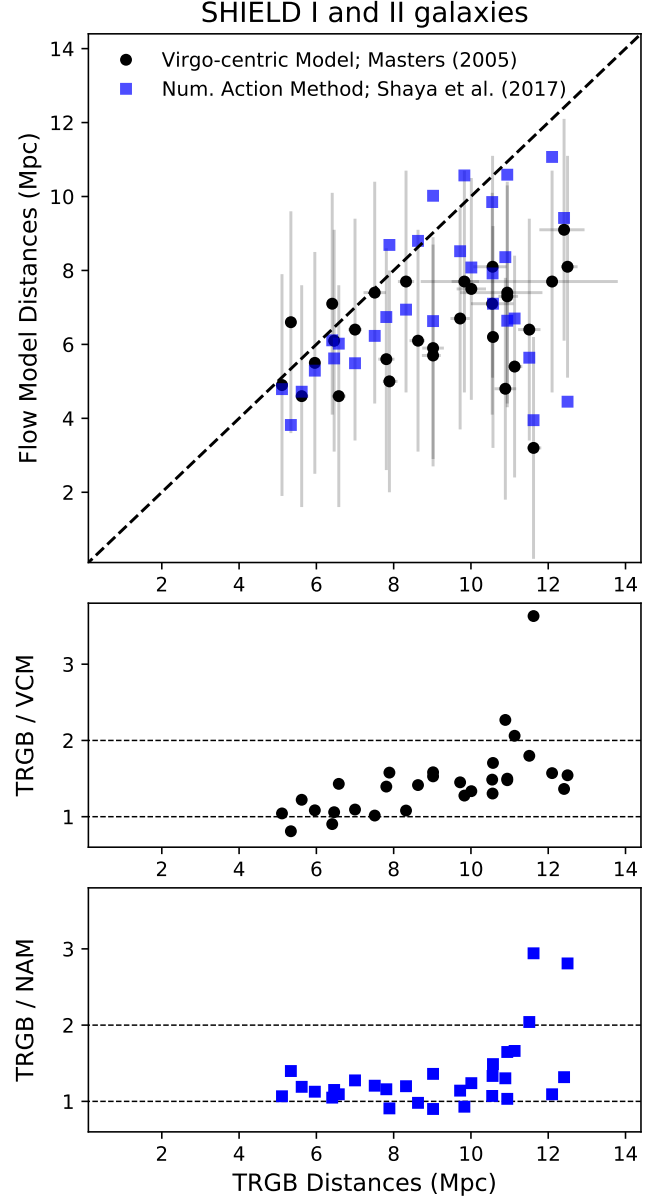


**Figure 5.** Top panel: Distances determined from a Virgo-centric flow model using the HI velocities of the galaxies ([Masters 2005](#)) versus the distances determined using the TRGB method (black circles). The dashed line represents one-to-one agreement between the two methods. While, overall, the flow model distances are within  $1\text{-}\sigma$  of our measured TRGB distances, the discrepancy for any individual galaxy be as much as a factor of four. Also shown are distance estimates based on the numerical action method from [Shaya et al. \(2017\)](#), blue squares). Lower two panels: The ratio of the TRGB distances to the Virgo-centric flow model ( $\text{TRGB} / \text{VCM}$ ) and the numerical action method ( $\text{TRGB} / \text{NAM}$ ) as a function of TRGB distance. These comparisons highlight the challenges of using velocity-based distances in the nearby universe for even inter-sample comparisons of galaxy properties.



**Table 4.** Comparison of TRGB and Flow-Model Distances

Galaxy	D <sub>TRGB</sub>	D <sub>M05</sub>	D <sub>S17</sub>
(1)	(2)	(3)	(4)
SHIELD I Galaxies			
AGC 110482	7.82 ± 0.21	5.6	6.7
AGC 111164	5.11 ± 0.07	4.9	4.8
AGC 111946	9.02 <sup>+0.2</sup> <sub>-0.29</sub>	5.7	6.6
AGC 111977	5.96 <sup>+0.11</sup> <sub>-0.09</sub>	5.5	5.3
AGC 112521	6.58 ± 0.18	4.6	6.0
AGC 174585	7.89 <sup>+0.21</sup> <sub>-0.17</sub>	5.0	8.7
AGC 174605	10.89 ± 0.28	4.8	8.4
AGC 182595	9.02 ± 0.28	5.9	10.0
AGC 731457	11.13 <sup>+0.2</sup> <sub>-0.16</sub>	5.4	6.7
AGC 748778	6.46 <sup>+0.14</sup> <sub>-0.17</sub>	6.1	5.6
AGC 749237	11.62 <sup>+0.2</sup> <sub>-0.16</sub>	3.2	4.0
AGC 749241	5.62 <sup>+0.17</sup> <sub>-0.14</sub>	4.6	4.7
SHIELD II Galaxies			
AGC 102728	12.41 <sup>+0.64</sup> <sub>-0.53</sub>	9.1	9.4
AGC 123352	9.72 ± 0.25	6.7	8.5
AGC 198507	10.94 <sup>+0.91</sup> <sub>-1.22</sub>	7.4	10.6
AGC 198508	9.83 <sup>+0.38</sup> <sub>-0.33</sub>	7.7	10.6
AGC 198691	12.1 <sup>+1.7</sup> <sub>-3.4</sub>	7.7	11.1
AGC 200232	10.57 <sup>+0.12</sup> <sub>-0.15</sub>	6.2	7.1
AGC 205590	10.55 ± 0.55	7.1	9.9
AGC 223231	8.32 ± 0.21	7.7	6.9
AGC 223254	6.41 <sup>+0.09</sup> <sub>-0.07</sub>	7.1	6.1
AGC 229053	12.50 <sup>+0.26</sup> <sub>-0.17</sub>	8.1	4.5
AGC 229379	7.51 ± 0.29	7.4	6.2
AGC 238890	5.34 ± 0.07	6.6	3.8
AGC 731448	10.01 ± 0.38	7.5	8.1
AGC 731921	11.51 ± 0.29	6.4	5.6
AGC 739005	8.63 <sup>+0.18</sup> <sub>-0.22</sub>	6.1	8.8
AGC 740112	10.56 <sup>+0.36</sup> <sub>-0.5</sub>	8.1	7.9
AGC 742601	7.00 ± 0.18	6.4	5.5
AGC 747826	10.94 <sup>+0.28</sup> <sub>-0.23</sub>	7.3	6.6

NOTE—Distances in Mpc measured using the TRGB method in this work compared with distance estimates from the Virgo-centric flow model of [Masters \(2005, D<sub>M05</sub>\)](#) and the Numerical Action Method of [Shaya et al. \(2017, D<sub>S17</sub>\)](#) for the SHIELD I and II samples. Uncertainties on the flow-model distances of [Masters \(2005\)](#) are estimated to be ±3 Mpc. A graphical comparison of the values is shown in Figure 5 and discussed in the text in §4.

have higher HI mass estimates and, thus, are excluded from our study. Also shown in Figure 5 is a comparison of our measured TRGB distances to estimates from the numerical action method (NAM) model that is based on galaxy orbit reconstruction ([Shaya et al. 2017](#)) with the NAM tool ([Kourkchi et al. 2020](#)) and is used in the CosmicFlows-3 program ([Tully et al. 2013](#)). The NAM distance estimates are a better match, although there

are still a number of points that disagree by a factor of 2.

The lower two panels in Figure 5 show the ratio of the TRGB distances to the Virgo-centric flow models (TRGB / VCM) and NAM method (TRGB / NAM) as a function of TRGB distance. These comparisons highlight the importance of primary distance measures in the local universe since the NAM distances are still discrepant. While parametric multi-attractor flow models work to minimize the impact, the complicated peculiar motions in the local universe make individual distances inferred from velocity based models highly uncertain. For even inter-sample comparisons, measuring distances via reliable methods such as the TRGB method are critical for accurate interpretation of galaxy properties as discrepancies at the factor of 2 level translate to differences of a factor of 4 for many galaxy properties that rely on the square of the distance (e.g., luminosity, galaxy masses, etc.).

## 5. CMD-BASED STAR FORMATION RATES

In addition to providing TRGB distances, the CMDs in Figure 3 and in Appendix A also contain information on the star formation histories of the galaxies. Qualitatively, differences in the overall stellar mass assembly of the galaxies can be discerned in the CMDs. The total number of stars detected in the CMDs gives an indication of the total stellar mass and constrains the lifetime SFRs. The structure of the brightest stellar evolution sequences gives an indication of recent star formation activity and points to obvious differences between galaxies in the sample. For example, as mentioned in §3.2, there is evidence of recent star formation activity in AGC 223231, based on the strong upper main sequence and helium burning sequences. In contrast, there has been comparatively less recent star formation in AGC 747826.

Quantitatively, the recent and lifetime star formation properties of the galaxies can be measured by fitting the CMD with a series of synthetic simple stellar populations of different ages and metallicities. The best-fitting modeled CMD represents the most likely star formation history (i.e., SFR(t)) of the system. Measuring detailed star formation histories with high time resolution requires both sufficient photometric depth and sufficiently populated CMDs. As the photometric depth of the SHIELD observations is limited to  $\sim 1$  mag below the expected TRGB by design, we limit the temporal resolution of the star formation histories to two time bins. Specifically, we measure the average SFR over the last 200 Myr (i.e.,  $\langle \text{SFR} \rangle_{200 \text{ Myr}}$ ) and the average SFR over the lifetime of the galaxy (i.e.,  $\langle \text{SFR} \rangle_{\text{life}}$ ).

The SFRs were measured using the CMD-fitting software MATCH (Dolphin 2002). We followed the same methodology employed in the analysis on the SHIELD I galaxies, as described in detail in (McQuinn et al. 2015b), with some modifications of the inputs. We assumed a Kroupa initial mass function (IMF) from Kroupa (2001) and a binary fraction of 35% with a flat secondary mass function distribution. The distances were fixed to the TRGB distances listed in Table 1 and the mean metallicities were constrained to be a continuous, non-decreasing function with time. We assumed the Galactic foreground extinction from Schlafly & Finkbeiner (2011), listed in Table 1, and assumed internal extinction values determined by iteratively fitting the CMDs with an extinction parameter in increments of 0.05 mag. The majority of galaxies were best fit without internal extinction; final values are listed in Table 1. Random uncertainties were estimated by applying a hybrid Markov Chain Monte Carlo simulation (Dolphin 2013). Systematic uncertainties from the stellar evolution models were estimated by applying shifts in luminosity and temperature to the observed stellar populations through 50 Monte Carlo simulations per solution (Dolphin 2012).

We experimented with deriving the CMD fits with different stellar libraries including PARSEC (Bressan et al. 2012) and MIST (Choi et al. 2016). Both the lifetime and recent SFRs from the two libraries agreed within the uncertainties. For the remainder of the analysis, we adopt the SFRs derived using the PARSEC library.

Table 1 lists the recent and lifetime SFRs as well as the present-day stellar masses for the sample. The present-day stellar masses were calculated based on the total stellar mass formed in each galaxy derived from the CMD fits with a Kroupa IMF (adjusted to the mass limits of  $0.1 - 100 M_{\odot}$ ; Telford et al. 2020) and assuming a correction for the amount of mass returned from stars via stellar winds and supernovae. We adopt a return mass fraction of 55% based on a Kroupa IMF at low metallicity.

As noted above, the star formation properties for the SHIELD I sample were previously derived using the same technique, but the CMD-fits were based on the Padua stellar evolutionary models from Marigo et al. (2008) with AGB tracks from Girardi et al. (2010), assumed a Salpeter IMF (Salpeter 1955), and adopting a lower return mass fraction of 30% (Kennicutt et al. 1994). To ensure the SHIELD galaxies can be inter-compared without a systematic bias due to these different assumptions, we have re-derived the star formation properties of SHIELD I using the PARSEC library, assuming a Kroupa IMF, and the higher return fraction

of 55%. The change from a Salpeter to a Kroupa IMF decreases the total stellar mass by a factor of  $\sim 0.66$ , while the difference in return fraction has a smaller impact. After adjusting for these changes, we found the originally derived stellar mass using the Padua library agreed within the uncertainties with those found using PARSEC in 10 of the 12 SHIELD I galaxies. For the remainder of our analysis for the SHIELD I galaxies, we adopt the star formation properties derived with the PARSEC library and the updated assumptions; those values can be found in Table 1.

As a consistency check, we compared our  $\langle \text{SFR}_{200 \text{ Myr}} \rangle$  to values determined using GALEX far ultraviolet imaging available for the SHIELD I galaxies (Teich et al. 2016) and adopting an empirically determined UV-SFR scaling relation (McQuinn et al. 2015a). All values agreed within the uncertainties. We also compared our measured stellar masses to values previously determined using Spitzer 3.6 and  $4.5 \mu\text{m}$  imaging (Hauberg et al. 2015). Here, we found that nearly all values also agreed within the uncertainties of the CMD-based stellar mass values. There were two exceptions that differed by 0.10 and 0.30 dex, which are still in reasonable agreement as the stellar masses reported from the Spitzer imaging do not have reported uncertainties.

Note that, while all galaxies have measurable star formation activity over the past 200 Myr, 6 of the 18 SHIELD II galaxies are not detected in H $\alpha$  (M. Shepley et al. in preparation). The lack of a massive star population needed to ionize hydrogen implies either that the SFR is fluctuating on short timescales, the upper IMF is not fully populated at these low SFRs, or both.

## 6. THE SHIELD NEIGHBORHOODS

In this section, we describe our investigation of the environments around the SHIELD galaxies. We searched for the nearest neighbors of our sample using the CosmicFlows-3 database (Tully et al. 2013) and the Updated Nearby Galaxy Catalog (Karachentsev et al. 2013). Wherever possible, we used robust distances determined, for example, from the TRGB or Cepheids. Some of the catalogued distances, however, are from less precise indicators. Regardless, the search for the nearest neighbors provides an overall picture of whether the SHIELD galaxies reside in highly dense versus sparse environments.

No galaxies were identified within 1 Mpc of 5 SHIELD galaxies (AGC 102728, AGC 123352, AGC 174605, AGC 198507, and AGC 198691). Of these, AGC 102728, AGC 176405, and AGC 198691 are located in Void Numbers 25, 8, and 12 respectively, identified by Pustilnik et al. (2019). Note, however, the in-depth study of

**Table 5.** Galaxies within 500 kpc of the SHIELD I and II samples

SHIELD	Neighbor	Neighbor	Neighbor	Dist.	3-D Separation
Galaxy	Galaxy	RA (J2000)	Dec (J2000)	(Mpc)	(kpc)
AGC 110482	IC 1727	1.791638	27.333021	7.45	420
AGC 111164	NGC0784	2.021333	28.843611	4.97	140
AGC 111164	UGC01281	1.825639	32.592500	4.94	420
AGC 112521	KK14	1.745206	27.288457	7.01	440
AGC 223254	UGC07603	12.47891	22.820347	6.79	390
AGC 739005	D564-08	9.048332	20.074716	8.83	440

NOTE—Galaxies within 500 kpc of the SHIELD I and II samples identified in the Cosmicflows-3 (Tully et al. 2013) and Updated Nearby Galaxy Catalog (Karachentsev et al. 2013). AGC 111164 appears to be paired with a slightly more massive neighbor and resides in a void (Pustilnik et al. 2016).

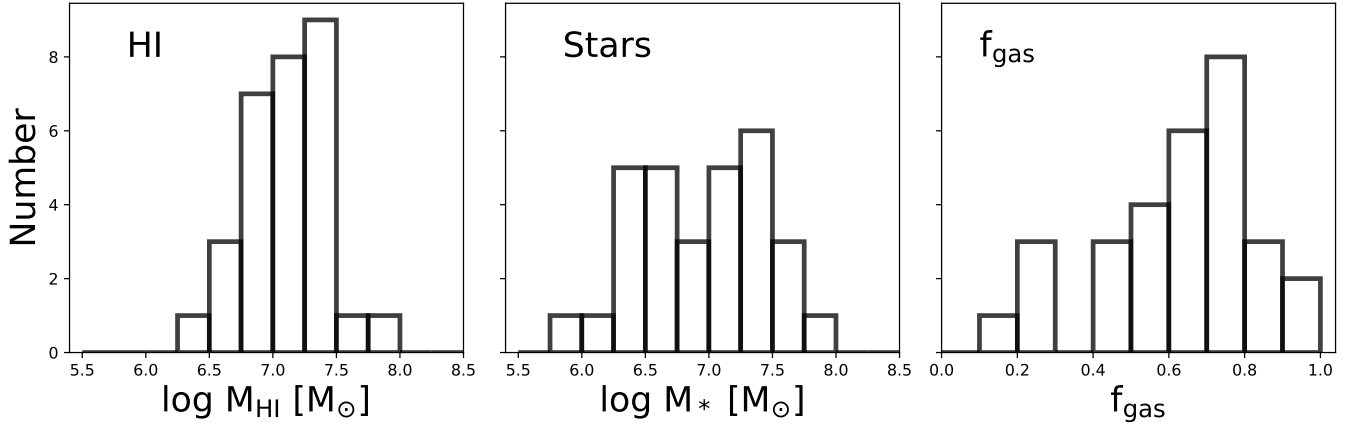


**Figure 6.** The number of galaxies as a function of HI mass, stellar mass, and gas fractions ( $f_{\text{gas}} = M_{\text{gas}}/M_{\text{bary}}$ ) which includes scaling the HI by 1.33 to account for the mass of helium. The mean HI mass of the SHIELD sample is  $1.6 \times 10^7 M_{\odot}$  with a standard deviation of  $1.1 \times 10^7$ . The stellar mass has a flatter distribution with a mean value of  $1.6 \times 10^7 M_{\odot}$ , and a standard deviation of  $1.6 \times 10^7$ . The gas fractions similarly span a wide range.

AGC 198691 suggests that a galaxy nearby-on-the-sky and also located in Void Number 12, UGC 5186, may be much closer than 1 Mpc and interacting (McQuinn et al. 2020). We also note that AGC 748778, which is identified as having two neighbors within 1 Mpc (i.e., UGC 0075 separated by 0.7 Mpc, and the newly discovered Pisces A separated by 0.9 Mpc; Tollerud et al. 2016) is also located within Void Number 25 (Pustilnik et al. 2019). Of the remaining 24 SHIELD galaxies, 6 galaxies have neighbors within 500 kpc as identified in the Cosmicflows-3 catalog, listed in Table 5.

From the study of the SHIELD I galaxies, McQuinn et al. (2014, see their Figure 6) reported 6 systems that appear to be part of 2 galaxy groups that are aligned in a single structure extending  $\sim 4$  Mpc. The main galaxies in these two loose groups are also dwarf galaxies, namely NGC 784 and NGC 672. The NGC 784 group is located in Void Number 8 by Pustilnik et al. (2019).

Despite being in low-density environments, loose associations of dwarf galaxies are not uncommon (e.g., Tully et al. 2006).

One SHIELD galaxy is within 200 kpc of its nearest neighbors and warrants additional discussion. AGC 111164 is located 140 kpc from NGC 784, the main galaxy in one of the aforementioned groups. NGC 784 is a starburst dwarf galaxy with a stellar mass of  $6 \times 10^8 M_{\odot}$  (McQuinn et al. 2010b). At this 3D physical separation, the evolution of each of the systems in this dwarf galaxy pair may be impacted by the gravitational presence of the other.

In summary, the SHIELD galaxies are located in sparsely populated environments. Seven (23%) SHIELD galaxies reside in voids catalogued by Pustilnik et al. (2019), five (17%) galaxies have no clearly identified neighbors within 1 Mpc, six (20%) reside in two loosely associated dwarf galaxy groups (McQuinn et al. 2014),

**Table 6.** Comparison of HI and Stellar Content

Galaxy	$M_{\text{HI}}/M_*$	$f_{\text{gas}}$	b	$\log(M_{\text{bary}}/M_{\odot})$
(1)	(2)	(3)	(4)	(5)
SHIELD I Galaxies				
AGC 110482	$0.76^{+0.44}_{-0.37}$	$0.50^{+0.15}_{-0.12}$	$1.1^{+0.8}_{-0.9}$	$7.70^{+0.13}_{-0.10}$
AGC 111164	$1.14^{+0.33}_{-0.38}$	$0.60^{+0.08}_{-0.09}$	$0.5^{+0.3}_{-0.3}$	$6.94^{+0.05}_{-0.06}$
AGC 111946	$2.23^{+1.03}_{-1.23}$	$0.75^{+0.10}_{-0.12}$	$1.6^{+0.9}_{-1.3}$	$7.41^{+0.05}_{-0.06}$
AGC 111977	$0.53^{+0.20}_{-0.22}$	$0.42^{+0.09}_{-0.10}$	$0.7^{+0.4}_{-0.4}$	$7.36^{+0.09}_{-0.10}$
AGC 112521	$2.40^{+1.02}_{-1.08}$	$0.76^{+0.11}_{-0.11}$	$0.9^{+0.7}_{-0.7}$	$7.09^{+0.05}_{-0.05}$
AGC 174585	$2.19^{+0.49}_{-0.82}$	$0.74^{+0.09}_{-0.11}$	$2.1^{+0.8}_{-1.3}$	$7.15^{+0.04}_{-0.05}$
AGC 174605	$1.49^{+2.15}_{-0.70}$	$0.66^{+0.33}_{-0.12}$	$1.2^{+1.9}_{-0.8}$	$7.57^{+0.21}_{-0.07}$
AGC 182595	$0.32^{+0.12}_{-0.18}$	$0.30^{+0.08}_{-0.12}$	$0.7^{+0.4}_{-0.5}$	$7.56^{+0.11}_{-0.17}$
AGC 731457	$0.28^{+0.03}_{-0.21}$	$0.27^{+0.02}_{-0.15}$	$1.0^{+0.1}_{-0.9}$	$7.95^{+0.02}_{-0.24}$
AGC 748778	$3.36^{+0.94}_{-1.68}$	$0.82^{+0.11}_{-0.13}$	$2.2^{+1.0}_{-1.8}$	$6.87^{+0.04}_{-0.05}$
AGC 749237	$2.27^{+2.05}_{-1.63}$	$0.75^{+0.17}_{-0.14}$	$1.6^{+1.6}_{-1.3}$	$8.01^{+0.10}_{-0.08}$
AGC 749241	$3.11^{+1.11}_{-0.95}$	$0.81^{+0.09}_{-0.08}$	$1.3^{+0.8}_{-0.8}$	$6.97^{+0.04}_{-0.03}$
SHIELD II Galaxies				
AGC 102728	$2.95^{+1.12}_{-2.22}$	$0.80^{+0.16}_{-0.18}$	$1.4^{+0.7}_{-1.2}$	$7.27^{+0.06}_{-0.08}$
AGC 123352	$2.95^{+0.75}_{-1.57}$	$0.80^{+0.08}_{-0.11}$	$1.5^{+0.5}_{-1.1}$	$7.40^{+0.03}_{-0.05}$
AGC 198507	$10.35^{+2.89}_{-6.42}$	$0.93^{+0.23}_{-0.30}$	$5.1^{+1.8}_{-3.5}$	$7.43^{+0.07}_{-0.10}$
AGC 198508	$1.54^{+0.54}_{-0.79}$	$0.67^{+0.13}_{-0.15}$	$2.1^{+0.8}_{-1.5}$	$7.23^{+0.06}_{-0.08}$
AGC 198691	$24.93^{+10.47}_{-20.44}$	$0.97^{+0.40}_{-0.77}$	$\dots$	$7.40^{+0.12}_{-0.24}$
AGC 200232	$0.51^{+0.22}_{-0.31}$	$0.40^{+0.11}_{-0.15}$	$0.5^{+0.3}_{-0.4}$	$7.88^{+0.11}_{-0.16}$
AGC 205590	$0.79^{+0.14}_{-0.66}$	$0.51^{+0.09}_{-0.22}$	$1.3^{+0.1}_{-1.4}$	$7.39^{+0.04}_{-0.18}$
AGC 223231	$2.47^{+0.32}_{-1.40}$	$0.77^{+0.07}_{-0.12}$	$2.1^{+0.8}_{-1.5}$	$7.44^{+0.02}_{-0.06}$
AGC 223254	$1.63^{+0.33}_{-0.57}$	$0.68^{+0.06}_{-0.08}$	$1.7^{+0.5}_{-1.0}$	$7.34^{+0.03}_{-0.05}$
AGC 229053	$1.14^{+0.55}_{-0.76}$	$0.60^{+0.12}_{-0.16}$	$0.4^{+0.3}_{-0.3}$	$7.79^{+0.09}_{-0.12}$
AGC 229379	$1.91^{+0.65}_{-0.90}$	$0.72^{+0.13}_{-0.15}$	$0.8^{+0.4}_{-0.7}$	$6.97^{+0.06}_{-0.07}$
AGC 238890	$0.18^{+0.04}_{-0.08}$	$0.19^{+0.04}_{-0.07}$	$0.2^{+0.1}_{-0.1}$	$7.21^{+0.06}_{-0.16}$
AGC 731448	$1.04^{+0.38}_{-0.64}$	$0.58^{+0.10}_{-0.16}$	$0.9^{+0.4}_{-0.7}$	$7.71^{+0.07}_{-0.11}$
AGC 731921	$0.87^{+0.13}_{-0.65}$	$0.54^{+0.05}_{-0.19}$	$0.5^{+0.1}_{-0.5}$	$7.99^{+0.03}_{-0.15}$
AGC 739005	$1.60^{+0.25}_{-0.98}$	$0.68^{+0.06}_{-0.14}$	$1.2^{+0.5}_{-1.0}$	$7.60^{+0.03}_{-0.09}$
AGC 740112	$0.28^{+0.07}_{-0.22}$	$0.27^{+0.06}_{-0.16}$	$0.1^{+0.0}_{-0.1}$	$7.73^{+0.07}_{-0.25}$
AGC 742601	$3.53^{+0.54}_{-1.79}$	$0.82^{+0.09}_{-0.12}$	$1.2^{+0.4}_{-1.0}$	$7.22^{+0.03}_{-0.05}$
AGC 747826	$0.60^{+0.16}_{-0.49}$	$0.44^{+0.07}_{-0.20}$	$0.4^{+0.1}_{-0.4}$	$7.70^{+0.06}_{-0.20}$

NOTE—HI to stellar mass ratios, gas fractions, birthrate parameter (i.e.,  $b = \langle \text{SFR} \rangle_{200 \text{ Myr}} / \langle \text{SFR} \rangle_{\text{life}}$ ) and baryonic masses for the SHIELD I and II samples. Note that  $f_{\text{gas}} = M_{\text{gas}}/M_{\text{bary}}$ ,  $M_{\text{bary}} = M_{\text{gas}} + M_*$ , and  $M_{\text{gas}} = 1.33 \times M_{\text{HI}}$ .

and one system appears to be loosely paired with another dwarf galaxy.

## 7. STELLAR AND GAS CONTENT

### 7.1. Characterizing the SHIELD Sample

The distributions of HI masses, stellar masses, and gas fractions are presented in Figure 6. The SHIELD I and II samples span  $\sim 1.5$  decades in HI mass ( $6.25 \lesssim \log(M_{\text{HI}}/M_{\odot}) \lesssim 7.75$ ) and more than  $\sim 2$  decades in stellar mass ( $5.5 < \log(M_*/M_{\odot}) < 8$ ). While the

galaxies are extremely low-mass ( $\log \langle M_{\text{HI}}/M_{\odot} \rangle = 7.2$ ), the upper mass range extends to higher values than the original limit of  $10^{7.2} M_{\odot}$  used to define the SHIELD galaxies. The sample was selected from the ALFALFA catalog based on the HI line flux and distance estimates. Since the measured TRGB distances are nearly all farther than the original estimates (see §4 and Figure 5), the HI masses of the galaxies are also larger. Despite this problem, all but two of current sample of 30 SHIELD galaxies have revised HI masses less than  $10^{7.5} M_{\odot}$ .

The resulting gas fractions, defined as  $f_{\text{gas}} = M_{\text{gas}}/M_{\text{bary}}$ , where  $M_{\text{bary}} = M_{\text{gas}} + M_*$  and  $M_{\text{gas}} = 1.33 \times M_{\text{HI}}$  to account for the helium content in the interstellar medium, range from  $f_{\text{gas}} = 19$  to 97%. Note that, despite some of the galaxies having lower gas-fractions, all of the galaxies are considered gas-rich. The gas fractions, as well as the HI-to-stellar mass ratios ( $M_{\text{HI}}/M_*$ ), are listed in Table 6.

The stellar masses span a larger range than the HI masses and have a flatter distribution, seen in the middle panel of Figure 6, which may also be a result of our imposed HI mass cutoff in our selection criteria. Unsurprisingly, given that SHIELD is an HI selected survey and includes galaxies previously overlooked in optical surveys, the gas fractions are predominantly high.

The declining number of sources below  $\log(M_{\text{HI}}/M_{\odot}) \sim 7$  reflects, in part, the growing incompleteness of the ALFALFA catalog at these very low masses (Haynes et al. 2011; Jones et al. 2018). While the HI mass function at lower masses and, in particular, the turnover, are not well quantified, larger numbers of low-mass galaxies than detected are expected. See §2.3 for a calculation of the number density of SHIELD galaxies and implications for finding lower mass galaxies in future surveys.

### 7.2. Star Formation and Gas Properties

Here, we explore the correlations between the recent star formation properties, stellar content, and gas content for galaxies at the faint end of the HI mass function. We use our measurements of the SHIELD galaxies as well as measurements of other low-mass galaxy samples from surveys introduced in §2, including the LITTLE THINGS survey (Hunter et al. 2012), the VLA/ANGST survey (Ott et al. 2012), and the FIGGS survey (Begum et al. 2008). Note that, as many of the measurements from the other surveys lack uncertainties, our focus is on the overall qualitative trends between the samples. For ease of comparison, the properties are shown in a series of plots in Figures 7–8.

The first panel in Figure 7 provides a comparison of the HI and stellar masses probed by the four surveys. The majority (63%) of the galaxies have  $M_{\text{HI}}/M_*$  ra-



tios approximately equal to or greater than unity, which is expected from HI selected surveys. VLA/ANGST, the only optically selected survey, is the exception and includes galaxies that have notably low HI masses for a given stellar mass. As noted in §2, the LITTLE THINGS study includes 40 galaxies within the Local Volume ( $D \lesssim 10$  Mpc), but we limit the comparison to the 32 galaxies for which stellar masses, determined from SED fits, and SFRs, based on the  $H\alpha$  emission, are reported (Zhang et al. 2012). The VLA/ANGST sample includes systems within  $\sim 4$  Mpc. Stellar masses were estimated from CMDs (Weisz et al. 2011), SFRs were estimated using the far-ultraviolet scaling relation (Kennicutt 1998) and adopting robust TRGB distances (Dalcanton et al. 2009). The FIGGS sample shown includes 59 low-mass galaxies. Stellar masses were calculated using the B-band luminosity and assuming a mass-to-light ratio of unity; no SFRs were reported.

The gas fractions as a function of  $M_*$  are presented in the middle panel in Figure 7. There is a general trend that gas fractions increase at lower stellar masses, but the spread in values is significant with a large range of gas fractions ( $\sim 0.4 - 0.9$ ) at nearly all stellar masses probed. The range in gas fractions at lower stellar mass could be even larger except for our observational bias.

Gas fractions are more directly correlated with higher recent SFRs relative to the lifetime averages. Shown in the final panel in Figure 7, the birthrate parameter ( $b \equiv$  recent SFR / lifetime SFR; Scalo 1986; Kennicutt et al. 2005) for the SHIELD systems increases with increasing gas content. Specifically, galaxies with  $b$  parameters  $\geq 1$  indicating constant or, in cases with  $b \gtrsim 2$ , a burst of star formation, have  $f_{\text{gas}} > 50\%$  (upper right shaded region; see e.g., McQuinn et al. 2009, 2010a, for defining bursting star formation in dwarf galaxies with the birthrate parameter), whereas systems with lower gas fractions are better characterized by a declining recent SFR relative to their lifetime average (lower left shaded region). As the gas fraction generally increases as stellar mass decreases, the birthrate parameter also increases for lower stellar masses, consistent with galaxy downsizing down to  $M_* \sim 10^6 M_\odot$ . The birthrate parameters for the SHIELD galaxies are listed in Table 6.

The recent SFRs, as a function of stellar mass, are shown in the left panel of Figure 8. The SFRs for the low-mass SHIELD galaxies increase with increasing galaxy stellar masses. The SFR- $M_*$  correlation is similar to the well-established and relatively tight trend found for star-forming galaxies with masses between  $\sim 10^8 \sim 10^{11} M_\odot$  (Brinchmann et al. 2004; Schiminovich et al. 2007) also shown in Figure 8. The main difference is a lower implied star formation efficiency than

extrapolations from the more massive galaxies to the mass regime of the SHIELD galaxies would suggest. The best-fitting line to the SFR- $M_*$  relation for the SHIELD galaxies is  $\log \text{SFR} = (-7.99 \pm 1.26) + (0.76 \pm 0.18) \cdot \log M_*$ , with an intrinsic dispersion in SFR of  $\sigma = 0.14$ . The VLA/ANGST sample lies in the same parameter space as the SHIELD galaxies; the LITTLE THINGS sample, which includes starbursting dwarfs (McQuinn et al. 2010b), show a larger range in SFRs for a given  $M_*$ . Note that, while the lower mass SHIELD galaxies have increasingly lower SFRs, these systems are gas-rich and have generally increasing gas fractions with sufficient material to fuel star formation. None of the galaxies have quenched star formation.

The specific SFRs ( $\text{sSFR} = \text{SFR} / M_*$ ) as a function of  $M_*$  are shown in the middle panel of Figure 8. Normalizing the SFR by stellar mass quantifies the intensity of star formation and helps to isolate other factors that may help regulate star formation (Brinchmann et al. 2004), including the energy input from supernovae. The best-fitting line to the SHIELD galaxies is  $\log \text{sSFR} = (-6.63 \pm 1.36) + (-0.44 \pm 0.20) \cdot \log M_*$ , with an intrinsic dispersion in sSFR of  $\sigma = 0.13$ . As with the  $\log \text{SFR} - \log M_*$  relation, the  $\log \text{sSFR} - \log M_*$  trend found for the SHIELD galaxies has a slope similar to the value of  $-0.36$  found for SDSS galaxies in the mass range  $10^8 - 10^{11} M_\odot$ , but with a lower sSFR intercept (Brinchmann et al. 2004; Schiminovich et al. 2007). The trend that sSFR increases with decreasing  $M_*$  is broader when considering the LITTLE THINGS sample. The larger spread in sSFR, as mentioned above, can be at least partially attributed to differences in sample as LITTLE THINGS includes starbursting dwarfs with intrinsically higher star formation activity for a given stellar mass. In addition, SFRs for LITTLE THINGS were derived using  $H\alpha$  emission which has been previously attributed to increasing the scatter in the SFR- $M_*$  relation at low galaxy masses (Bothwell et al. 2009).  $H\alpha$  emission can under-represent the SFR in systems with star formation activity below  $\sim 10^{-3} M_\odot \text{ yr}^{-1}$  where the upper-end of the IMF may not be fully populated (Lee et al. 2009).

Note that the SFR- $M_*$  relation for the SHIELD galaxies has a shallower slope than what has been reported for a sample of 56 low surface brightness (LSB) galaxies, which has a slope consistent with unity (McGaugh et al. 2017). For the LSB sample, the SFRs were based on  $H\alpha$  fluxes and the stellar masses were based on optical mass-to-light ratios yielding the relation  $\log \text{SFR} = (-10.75 \pm 0.53) + (1.04 \pm 0.06) \cdot \log M_*$ , with an intrinsic scatter of  $\sigma = 0.34$ . These authors suggest that the steeper slope for the LSB galaxies relative to more massive galaxies is another manifestation of galaxy down-

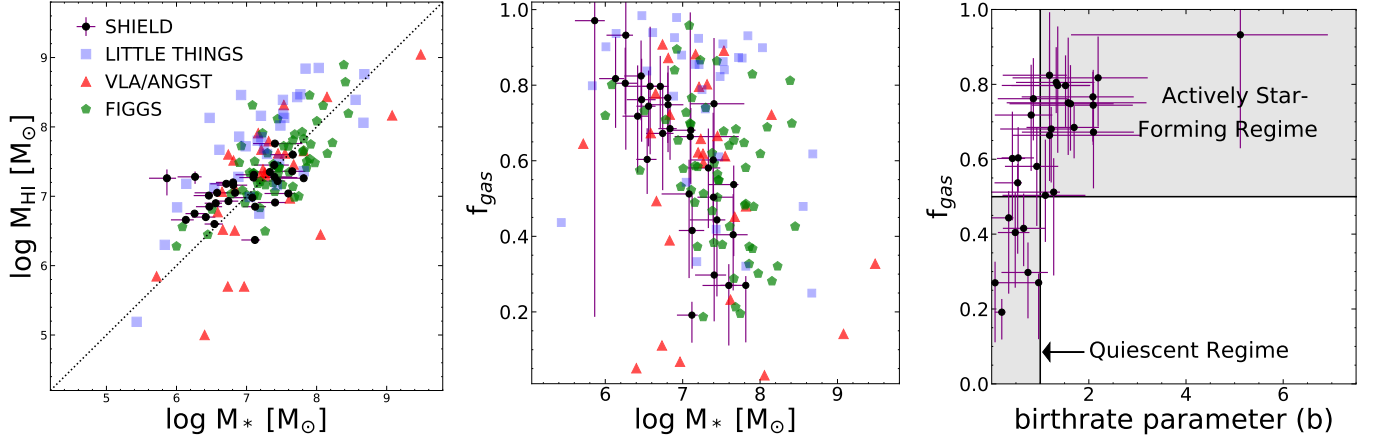


**Figure 7.** Left: The HI masses as a function of stellar mass for the SHIELD I and II galaxies (black points). Samples from the literature are shown including from LITTLE THINGS (blue squares; Hunter et al. 2012; Zhang et al. 2012), VLA/ANGST (red triangles; Ott et al. 2012), and FIGGS (green pentagons; Begum et al. 2008). Middle: Gas fractions as a function of stellar mass. Right: Gas fractions compared with the birthrate parameter for the SHIELD I and II samples. Galaxies with birthrate parameters  $b \geq 1$  are labeled actively star-forming in the upper right shaded region whereas systems with  $b < 1$  are labeled quiescent in the lower left shaded region.

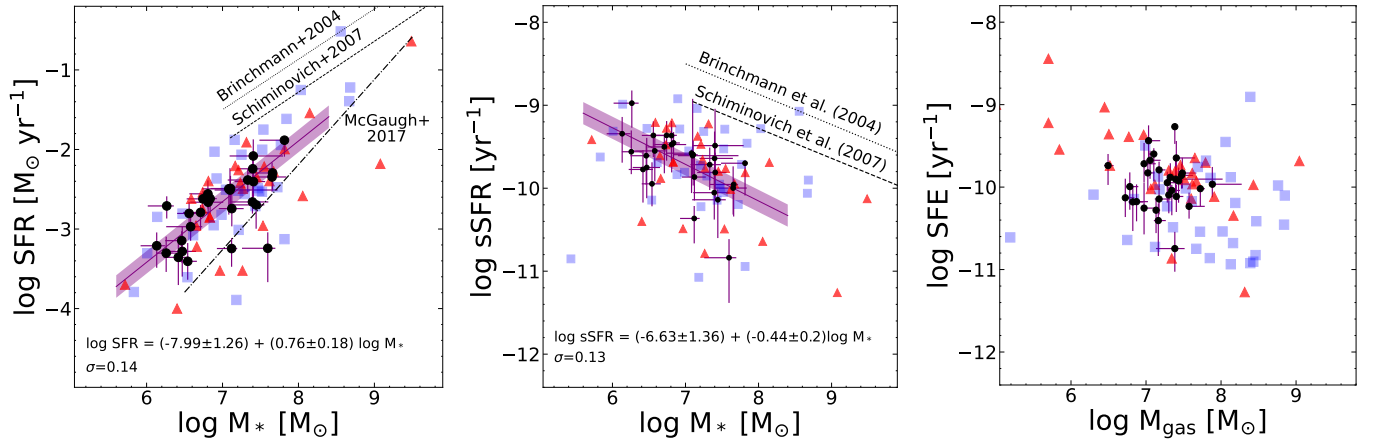


**Figure 8.** Left: Recent SFRs as a function of stellar mass. Best-fit line to the SHIELD data and the  $1 - \sigma$  dispersion are shown in the panel. The  $\log \text{SFR} - \log M_*$  relations extrapolated from more massive galaxies (Brinchmann et al. 2004; Schiminovich et al. 2007) and from LSB galaxies in the low-mass galaxy regime (McGaugh et al. 2017) are also shown. Middle: recent SFRs normalized by stellar mass (sSFR) as a function of stellar mass. The same relations normalized by stellar mass are shown except for the LSB sample which has a flat slope. Right: SFE as a function of gas mass; the SFE axis limits are set to the same range as the sSFRs to allow a direct comparison between normalizations. Symbols are the same as in Figure 7.

sizing. Interestingly, if we consider only the SHIELD galaxies with a birthrate parameter less than 1, we find  $\log \text{SFR} = (-9.85 \pm 2.30) + (0.99 \pm 0.32) \cdot \log M_*$ , with an intrinsic scatter of  $\sigma = 0.21$ , in excellent agreement with the LSB relation. Thus, while the full SHIELD sample is consistent with a shallower slope more typical of spiral galaxies, a subset with lower recent star formation is consistent with the star-formation properties of LSB galaxies in this mass regime.

The stellar mass is likely not the dominant factor in regulating star formation in low-mass galaxies. Instead, it is likely that the star formation process has a greater

dependency upon both the overall gas mass and gas fraction. To investigate this further, we normalize the SFRs by *gas masses*, which is often referred to as the star formation efficiency (SFE) as it calculates the inverse timescale of converting gas to stars.

The SFE as a function of gas mass is shown in the right panel of Figure 8. To allow for a direct comparison with the normalization by stellar mass, the axis ranges for the SFE are the same as those used for the sSFR in the middle panel of Figure 8. The SFEs are increasing for galaxies with lower gas masses, but with a large spread of nearly 2 orders of magnitude at  $M_* \sim 10^7$

$M_{\odot}$ . The gas depletion timescales, calculated by taking the inverse of the SFEs of the galaxies, range from 2–56 Gyr, with a mean approximately equal to a Hubble time (12 Gyr). Thus, the SHIELD galaxies have enough gas to continue fueling star formation over long timescales, in contrast to spiral galaxies with short gas depletion timescales that imply gas accretion is required to maintain star formation activity over comparable timescales.

In summary, the stellar content, gas content, and star forming properties of the gas-rich, low mass galaxies of the SHIELD, VLA/ANGST, LITTLE THINGS, and FIGGS samples, are qualitatively similar to one another. Overall observed trends show higher gas fractions and higher birthrate parameters at lower masses, but with significant scatter. Based on the quantitative fits to the SHIELD galaxies, galaxies in the mass range  $\sim 10^6 - 10^7 M_{\odot}$  are consistent with extrapolations from more massive star-forming galaxies with a lower SFE normalization. Low SFEs are expected at lower surface mass densities by nearly all models of star formation (e.g., Krumholz et al. 2012, and reference therein). SHIELD galaxies with low birthrate parameters follow the SFR –  $M_*$  trend identified for LSB galaxies.

## 8. SUMMARY

The SHIELD program includes a complete sample of low-mass, gas-rich galaxies from the cosmological volume in the local universe observed in the ALFALFA survey. The SHIELD galaxies populate the under-explored regime of very low-mass galaxies, offering the opportunity to bridge our knowledge of classical gas-rich dwarfs (i.e.,  $M_* \sim 10^8 M_{\odot}$ ) to the intrinsically faint and low-surface brightness frontier of galaxies discoverable in, for example, the Rubin Observatory Large Survey of Space and Time (LSST) and SKA eras.

Using newly obtained HST optical imaging of the resolved stars and WSRT observations of the neutral hydrogen, we measure the TRGB distances, star formation activity, and gas properties for 18 of the 82 SHIELD galaxies. Combined with existing similar measurements of an additional 12 SHIELD systems, we begin to quantify the properties at the faint end of the luminosity function with statistical confidence.

We introduce a new technique for measuring the rotational velocity and spatial extent of the HI gas in low mass galaxies when the HI has a limited extent and the velocity field is not suitable for dynamical modelling (§3.5 and Appendix C). Applying this technique to 30 SHIELD galaxies, we report on their gas kinematics (Table 3); future work will include a comparison of these results with other measures of the HI rotation in low mass galaxies (J. Fuson et al. in preparation).

The TRGB distances place the galaxies in the Local Volume, but at distances farther than estimates from parametric flow models (§4). The majority of the SHIELD galaxies are located in under-dense environments (§6), with several residing in voids (Pustilnik et al. 2019).

From measurements of the resolved stars and HI data, we find the log of the HI and stellar masses, in units of  $M_{\odot}$ , range from 6.25 – 7.75 and 5.75 – 8.0, respectively (Figure 6). The galaxies are predominantly gas-rich with  $\langle M_{\text{HI}}/M_* \rangle = 1.9$ , excluding the extreme system AGC 198691, which has a  $M_{\text{HI}}/M_*$  value of 25. Recent SFRs ( $t \sim 200$  Myr) range from  $4 \times 10^{-4}$  to  $8 \times 10^{-3} M_{\odot} \text{ yr}^{-1}$  (§7).

Overall, the properties of the SHIELD I and II galaxies, as well as the properties of galaxies in the LITTLE THINGS, VLA/ANGST, and FIGGS surveys, appear to be a continuation from higher masses when considering their SFRs, HI and stellar masses, gas fractions, and specific SFRs (Figures 7–8), although with lower implied star formation efficiencies. When SHIELD galaxies with low birthrate parameters are considered separately, the SFR –  $M_*$  relation is steeper and consistent with the trend measured for LSB galaxies (McGaugh et al. 2017).

Despite the low baryonic masses, the ongoing star formation in the SHIELD galaxies suggests sufficiently deep potential wells that both enable the galaxies to retain some gas and promote the concentration of gas needed for star formation. Simulations predict that galaxies in this mass regime may have a range of baryon-to-dark matter mass. If the baryon fraction (i.e.,  $M_{\text{baryon}} / M_{\text{halo}}$ ) is lower than the typical fractions estimated in more massive galaxies, this would offer an explanation for the continuation of the scaling relations. In an upcoming paper, we explore the location of the SHIELD galaxies in the Baryonic Tully Fisher Relation and their implied dark matter content (K. McQuinn et al. in preparation).

The number density of these surveys suggest that current samples are significantly incomplete below  $M_* \sim 10^7 M_{\odot}$ ; upcoming facilities such as the Rubin Observatory and the SKA have the potential for discovering larger samples below this mass threshold (§2.3).

*Facilities:* Hubble Space Telescope, Westerbork Synthesis Radio Telescope

*Software:* Astropy (Astropy Collaboration et al. 2013, 2018)

## 9. ACKNOWLEDGMENTS

KBWM would like to thank Hunter Thu for a helpful exploration of the surface brightness properties of

the galaxies. We would also like to thank the referee for helpful comments that improved the manuscript. Support for program HST-GO-13750 was provided by NASA through a grant from the Space Telescope Science Institute, which is operated by the Associations of Universities for Research in Astronomy, Incorporated, under NASA contract NAS 5-26555 and by a COX grant from the University of Texas at Austin. KBWM is supported by related grant HST-GO-15243. MPH is supported by grants NSF/AST-1714828 and from the Brinson Foundation. JMC is supported by NSF/AST-2009894 and by Macalester College. EAKA is supported by the WISE research programme, which is financed by the Netherlands Organisation for Sci-

entific Research (NWO). KLR is supported by NSF grant AST-1615483. The Westerbork Synthesis Radio Telescope is operated by the ASTRON (Netherlands Institute for Radio Astronomy) with support from the Netherlands Foundation for Scientific Research (NWO). This research has made use of NASA Astrophysics Data System Bibliographic Services and the NASA/IPAC Extragalactic Database (NED), which is operated by the Jet Propulsion Laboratory, California Institute of Technology, under contract with the National Aeronautics and Space Administration.

This work is dedicated in loving memory to Anne B. Wingfield.

## REFERENCES

- Adams, E. A. K., & Oosterloo, T. A. 2018, *A&A*, 612, A26
- Anderson, J., & Bedin, L. R. 2010, *PASP*, 122, 1035
- Astropy Collaboration, Robitaille, T. P., Tollerud, E. J., et al. 2013, *A&A*, 558, A33
- Astropy Collaboration, Price-Whelan, A. M., SipHocz, B. M., et al. 2018, *aj*, 156, 123
- Barnes, D. G., Staveley-Smith, L., de Blok, W. J. G., et al. 2001, *MNRAS*, 322, 486
- Beaton, R. L., Bono, G., Braga, V. F., et al. 2018, *SSRv*, 214, 113
- Begum, A., Chengalur, J. N., Karachentsev, I. D., Sharina, M. E., & Kaisin, S. S. 2008, *MNRAS*, 386, 1667
- Bothwell, M. S., Kennicutt, R. C., & Lee, J. C. 2009, *MNRAS*, 400, 154
- Bressan, A., Marigo, P., Girardi, L., et al. 2012, *MNRAS*, 427, 127
- Brinchmann, J., Charlot, S., White, S. D. M., et al. 2004, *MNRAS*, 351, 1151
- Bullock, J. S., & Boylan-Kolchin, M. 2017, *ARA&A*, 55, 343
- Cannon, J. M., Giovanelli, R., Haynes, M. P., et al. 2011, *ApJL*, 739, L22
- Carlsten, S. G., Greco, J. P., Beaton, R. L., & Greene, J. E. 2020, *ApJ*, 891, 144
- Choi, J., Dotter, A., Conroy, C., et al. 2016, *ApJ*, 823, 102
- Dalcanton, J. J., Williams, B. F., Seth, A. C., et al. 2009, *ApJS*, 183, 67
- Di Teodoro, E. M., & Fraternali, F. 2015, *MNRAS*, 451, 3021
- Dolphin, A. E. 2000, *PASP*, 112, 1383
- . 2002, *MNRAS*, 332, 91
- . 2012, *ApJ*, 751, 60
- . 2013, *ApJ*, 775, 76
- Drlica-Wagner, A., Bechtol, K., Mau, S., et al. 2020, *ApJ*, 893, 47
- Ferrara, A., & Tolstoy, E. 2000, *MNRAS*, 313, 291
- Ford, H. C., Bartko, F., Bely, P. Y., et al. 1998, in *Society of Photo-Optical Instrumentation Engineers (SPIE) Conference Series*, Vol. 3356, *Space Telescopes and Instruments V*, ed. P. Y. Bely & J. B. Breckinridge, 234–248
- Geha, M., Wechsler, R. H., Mao, Y.-Y., et al. 2017, *ApJ*, 847, 4
- Giovanelli, R., Haynes, M. P., Kent, B. R., et al. 2005, *AJ*, 130, 2598
- Girardi, L., Williams, B. F., Gilbert, K. M., et al. 2010, *ApJ*, 724, 1030
- Gnedin, N. Y. 2000, *ApJ*, 542, 535
- Gonzaga, S. 2012, *The DrizzlePac Handbook*
- Greco, J. P., Greene, J. E., Strauss, M. A., et al. 2018, *ApJ*, 857, 104
- Haurberg, N. C., Salzer, J. J., Cannon, J. M., & Marshall, M. V. 2015, *ApJ*, 800, 121
- Haynes, M. P., Giovanelli, R., Martin, A. M., et al. 2011, *AJ*, 142, 170
- Haynes, M. P., Giovanelli, R., Kent, B. R., et al. 2018, *ApJ*, 861, 49
- Hirschauer, A. S., Salzer, J. J., Skillman, E. D., et al. 2016, *ApJ*, 822, 108
- Hoefl, M., Yepes, G., Gottlöber, S., & Springel, V. 2006, *MNRAS*, 371, 401
- Hunter, D. A., Ficut-Vicas, D., Ashley, T., et al. 2012, *AJ*, 144, 134
- Ikeuchi, S., & Ostriker, J. P. 1986, *ApJ*, 301, 522
- Jang, I. S., & Lee, M. G. 2017, *The Astrophysical Journal*, 835, 28

- Jones, M. G., Haynes, M. P., Giovanelli, R., & Moorman, C. 2018, *MNRAS*, 477, 2
- Karachentsev, I. D., Makarov, D. I., & Kaisina, E. I. 2013, *AJ*, 145, 101
- Kennicutt, R. C., Lee, J. C., Akiyama, S., Funes, J. G., & Sakai, S. 2005, in *American Institute of Physics Conference Series*, Vol. 783, *The Evolution of Starbursts*, ed. S. Hüttmeister, E. Manthey, D. Bomans, & K. Weis, 3–16
- Kennicutt, Jr., R. C. 1998, *ARA&A*, 36, 189
- Kennicutt, Jr., R. C., Tamblyn, P., & Congdon, C. E. 1994, *ApJ*, 435, 22
- Kourkchi, E., Courtois, H. M., Graziani, R., et al. 2020, *AJ*, 159, 67
- Kroupa, P. 2001, *MNRAS*, 322, 231
- Krumholz, M. R., Dekel, A., & McKee, C. F. 2012, *ApJ*, 745, 69
- Lee, J. C., Gil de Paz, A., Tremonti, C., et al. 2009, *ApJ*, 706, 599
- Lee, M. G., Freedman, W. L., & Madore, B. F. 1993, *ApJ*, 417, 553
- Mac Low, M., & Ferrara, A. 1999, *ApJ*, 513, 142
- Makarov, D., Makarova, L., Rizzi, L., et al. 2006, *AJ*, 132, 2729
- Mao, Y.-Y., Geha, M., Wechsler, R. H., et al. 2020, arXiv e-prints, arXiv:2008.12783
- Marigo, P., Girardi, L., Bressan, A., et al. 2008, *A&A*, 482, 883
- Massey, R., Stoughton, C., Leauthaud, A., et al. 2010, *MNRAS*, 401, 371
- Masters, K. L. 2005, PhD thesis, Cornell University, New York, USA
- McGaugh, S. S., Schombert, J. M., & Lelli, F. 2017, *The Astrophysical Journal*, 851, 22
- McGaugh, S. S., & Wolf, J. 2010, *ApJ*, 722, 248
- McNichols, A. T., Teich, Y. G., Nims, E., et al. 2016, *ApJ*, 832, 89
- McQuinn, K. B. W., Boyer, M., Skillman, E. D., & Dolphin, A. E. 2019a, *ApJ*, 880, 63
- McQuinn, K. B. W., Skillman, E. D., Cannon, J. M., et al. 2009, *ApJ*, 695, 561
- McQuinn, K. B. W., Skillman, E. D., Dolphin, A. E., & Mitchell, N. P. 2015a, *ApJ*, 808, 109
- McQuinn, K. B. W., van Zee, L., & Skillman, E. D. 2019b, *ApJ*, 886, 74
- McQuinn, K. B. W., Skillman, E. D., Cannon, J. M., et al. 2010a, *ApJ*, 721, 297
- . 2010b, *ApJ*, 724, 49
- McQuinn, K. B. W., Cannon, J. M., Dolphin, A. E., et al. 2014, *ApJ*, 785, 3
- . 2015b, *ApJ*, 802, 66
- McQuinn, K. B. W., Berg, D. A., Skillman, E. D., et al. 2020, *ApJ*, 891, 181
- Meyer, M. J., Zwaan, M. A., Webster, R. L., et al. 2004, *MNRAS*, 350, 1195
- Okamoto, T., Gao, L., & Theuns, T. 2008, *MNRAS*, 390, 920
- Ott, J., Stilp, A. M., Warren, S. R., et al. 2012, *AJ*, 144, 123
- Pustilnik, S. A., Perepelitsyna, Y. A., & Kniazev, A. Y. 2016, *Monthly Notices of the Royal Astronomical Society*, 463, 670
- Pustilnik, S. A., Tepliakova, A. L., & Makarov, D. I. 2019, *MNRAS*, 482, 4329
- Rees, M. J. 1986, *MNRAS*, 218, 25P
- Rizzi, L., Tully, R. B., Makarov, D., et al. 2007, *ApJ*, 661, 815
- Sakai, S., Madore, B. F., & Freedman, W. L. 1996, *ApJ*, 461, 713
- Salaris, M., & Girardi, L. 2005, *MNRAS*, 357, 669
- Salpeter, E. E. 1955, *ApJ*, 121, 161
- Scalo, J. M. 1986, *FCPh*, 11, 1
- Schiminovich, D., Wyder, T. K., Martin, D. C., et al. 2007, *ApJS*, 173, 315
- Schlafly, E. F., & Finkbeiner, D. P. 2011, *ApJ*, 737, 103
- Schlegel, D. J., Finkbeiner, D. P., & Davis, M. 1998, *ApJ*, 500, 525
- Shaya, E. J., Tully, R. B., Hoffman, Y., & Pomarède, D. 2017, *ApJ*, 850, 207
- Smercina, A., Bell, E. F., Price, P. A., et al. 2018, *ApJ*, 863, 152
- Sternberg, A., McKee, C. F., & Wolfire, M. G. 2002, *ApJS*, 143, 419
- Teich, Y. G., McNichols, A. T., Nims, E., et al. 2016, *ApJ*, 832, 85
- Telford, O. G., Dalcanton, J. J., Williams, B. F., et al. 2020, *ApJ*, 891, 32
- Tollerud, E. J., Geha, M. C., Grcevich, J., et al. 2016, *ApJ*, 827, 89
- Tully, R. B., Rizzi, L., Dolphin, A. E., et al. 2006, *AJ*, 132, 729
- Tully, R. B., Courtois, H. M., Dolphin, A. E., et al. 2013, *AJ*, 146, 86
- Weisz, D. R., Dalcanton, J. J., Williams, B. F., et al. 2011, *ApJ*, 739, 5
- Zhang, H.-X., Hunter, D. A., Elmegreen, B. G., Gao, Y., & Schruba, A. 2012, *AJ*, 143, 47



## APPENDIX

We include three appendices. The first, Appendix A, is an atlas of the 3-color HST images, CMDs from the resolved stellar populations, and a comparison of the HI column densities with the stellar distributions. The second, Appendix B, is an atlas of the HI spectra, moment zero maps, moment one maps, and PV diagrams of the galaxies. The third, Appendix C, includes a detailed description of our new methodology for measuring the rotational velocity and spatial extent of the HI in data with limited spatial sampling, with applications to the SHIELD I and II galaxies.

## A. ATLAS OF HST IMAGES AND CMDs

We present an atlas of the HST optical images, CMDs, and HST images with WSRT 21-cm contours overlaid for the remaining SHIELD II galaxies. The figures follow the same format presented in Figure 3; we refer the reader to the description presented in §3.1 for details.

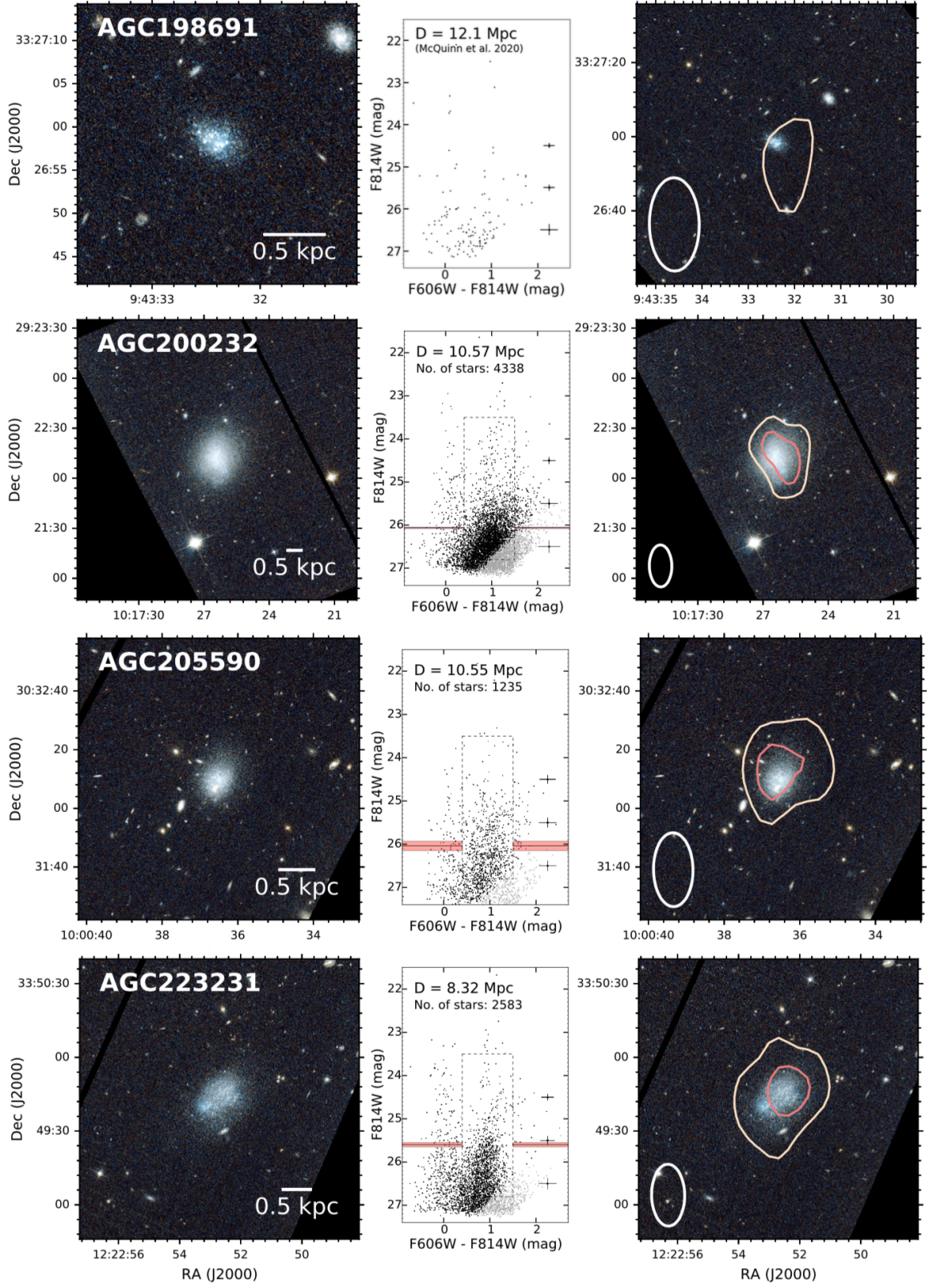


**Figure 9.** HST optical images, CMDs, and WSRT HI data for AGC 198691, AGC 200232, AGC 205590, AGC 223231. See Figure 3 caption for details.

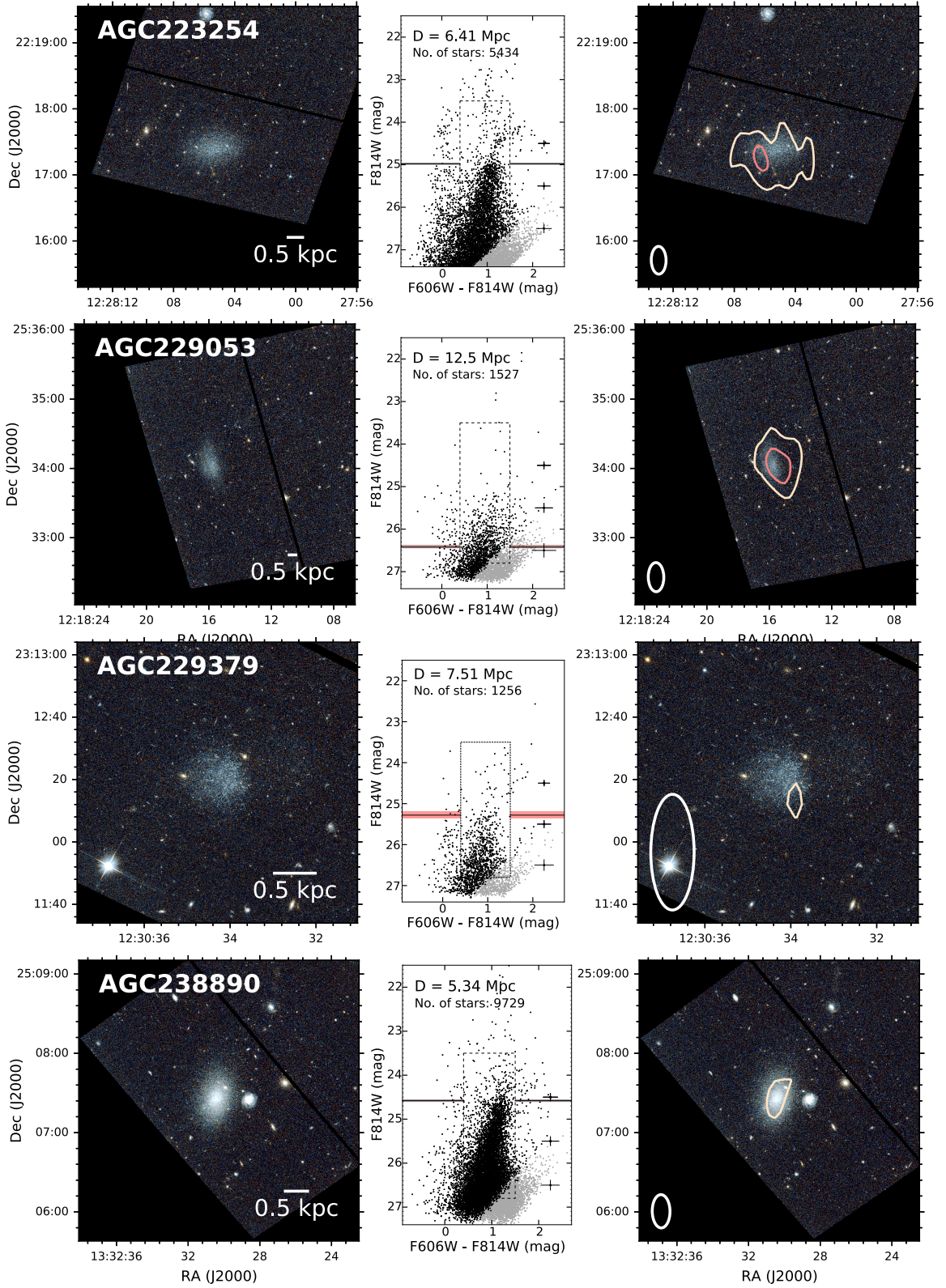


**Figure 10.** HST optical images, CMDs, and WSRT HI data for AGC 223254, AGC 229053, AGC 229379, AGC 238890. See Figure 3 caption for details.



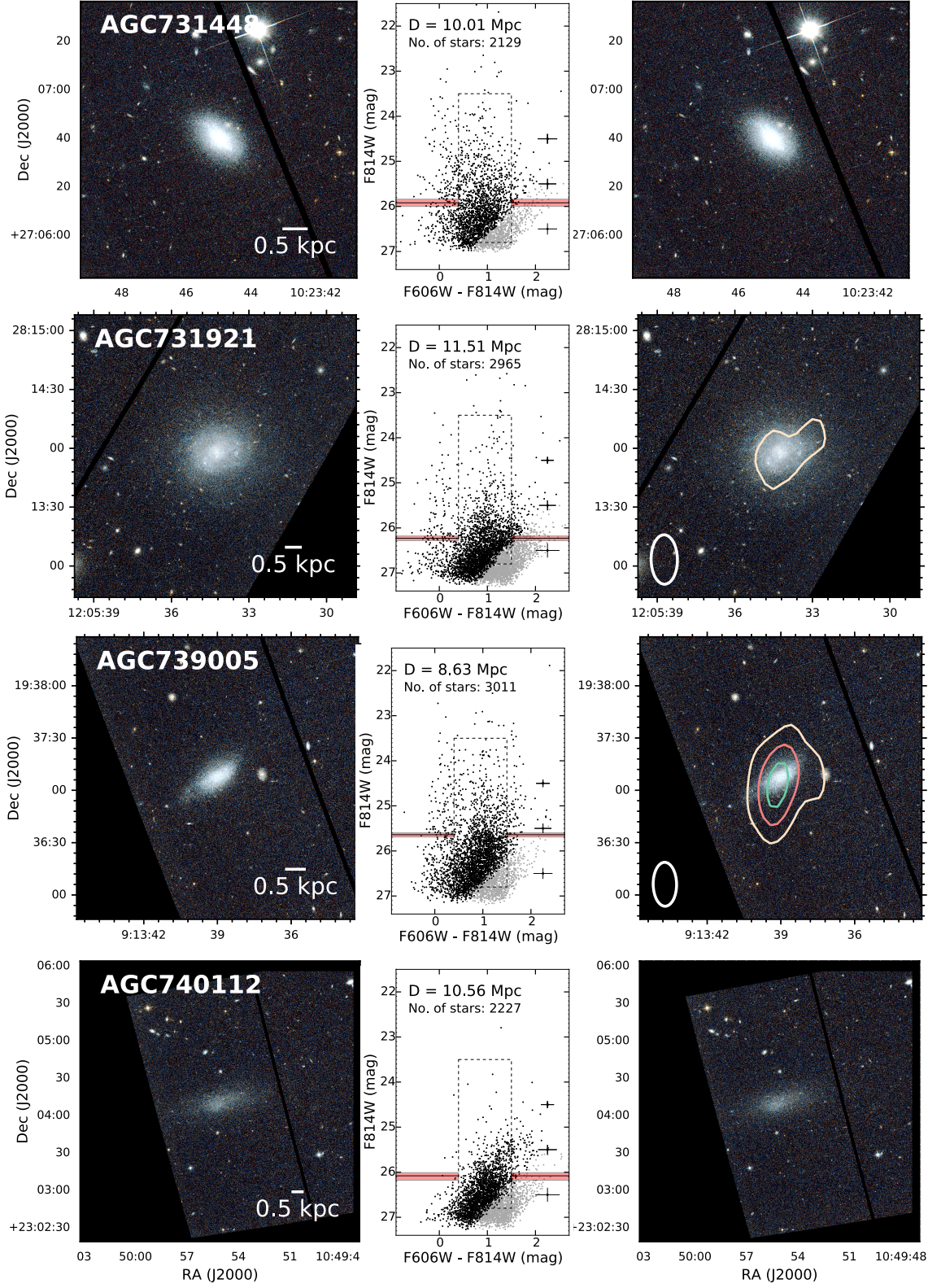


**Figure 11.** HST optical images, CMDs, and WSRT HI data for AGC 731448, AGC 731921, AGC 739005, AGC 740112. See Figure 3 caption for details. WSRT HI data are not available for AGC 731448 and AGC 740112; see §3.3 for details.



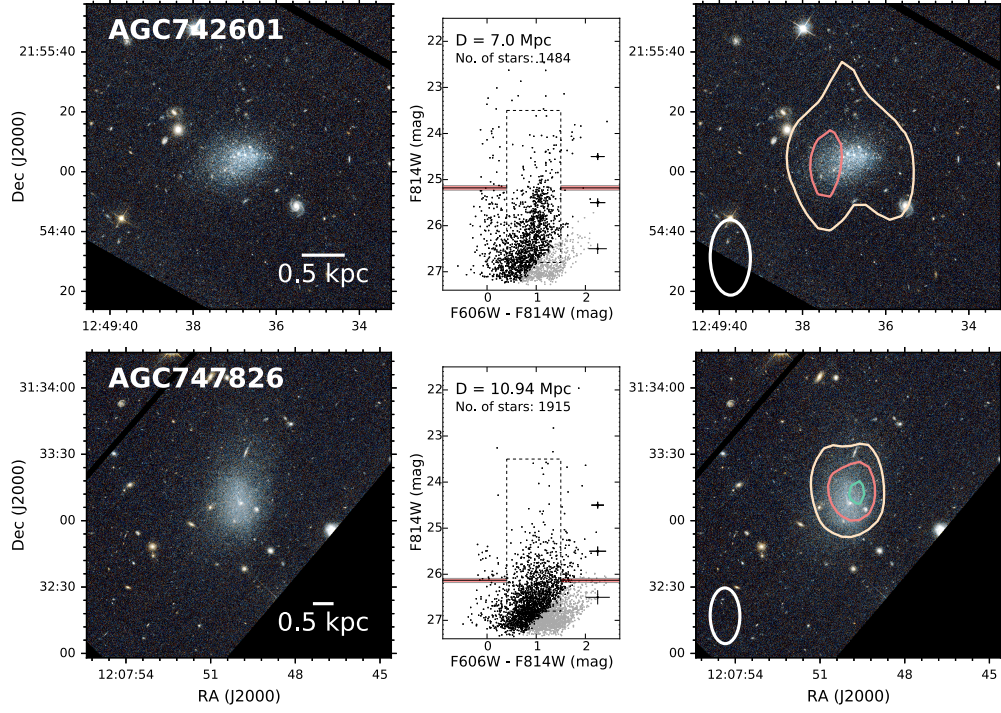


**Figure 12.** HST optical images, CMDs, and WSRT H I data for AGC 742601, AGC 747826. See Figure 3 caption for details.

## B. HI ATLAS

We present an atlas of the WSRT HI observations including the 21-cm spectra, HI column density maps (moment zero maps), HI velocity fields (moment one maps), and PV diagrams for the remaining SHIELD II galaxies with WSRT detections. The figures follow the same format presented in Figure 4; we refer the reader to the description presented in §3.3 for details.

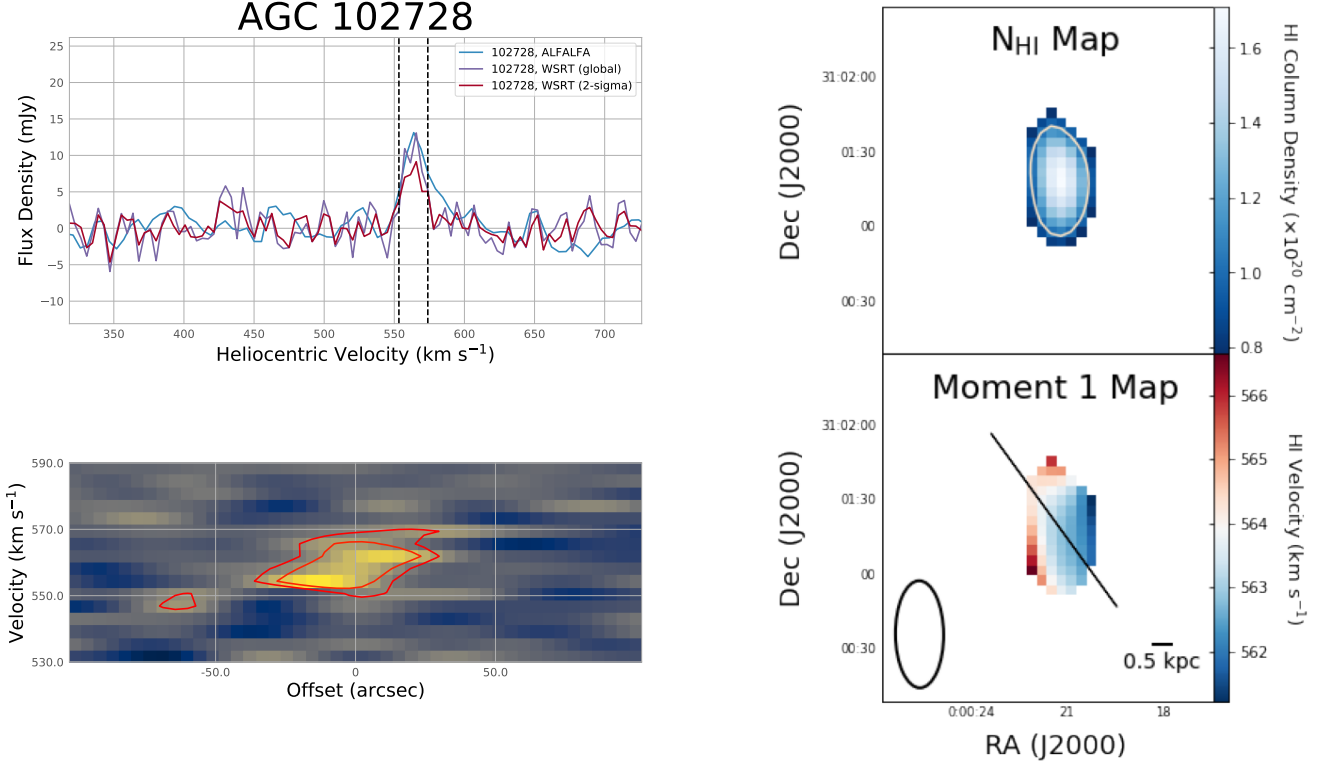


**Figure 13.** AGC 102728. There is a modest projected velocity gradient from southwest to northwest with a magnitude of 7  $\text{km s}^{-1}$ . The source is only marginally resolved by the HI beam.

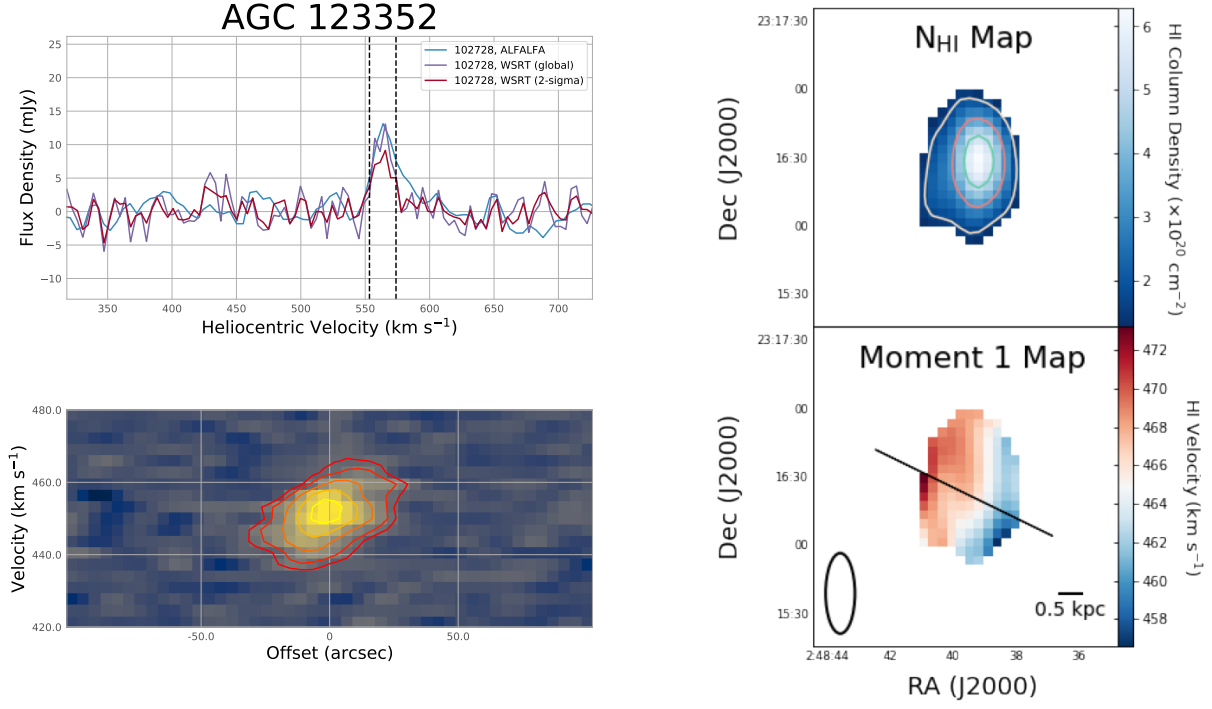


**Figure 14.** AGC123352. There is a clear projected velocity gradient from southwest to northwest with a magnitude of  $13 \text{ km s}^{-1}$ .

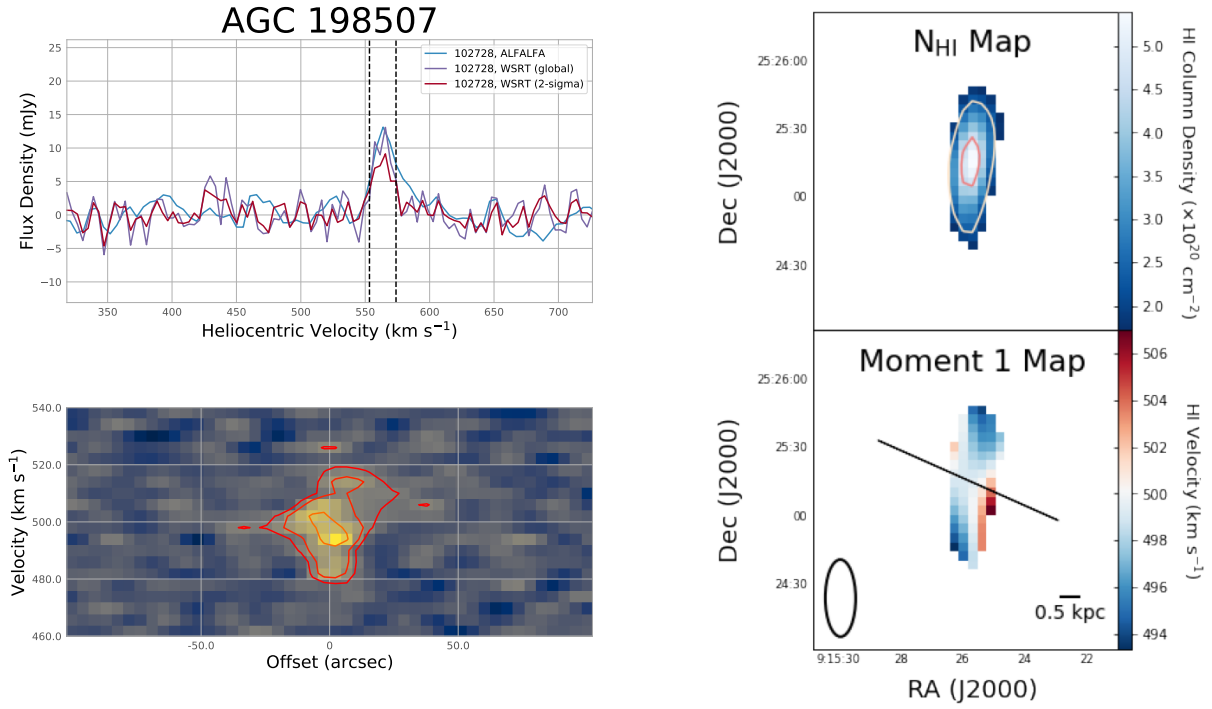


**Figure 15.** AGC198507. The HI morphology of this source is curious, with an extension of low surface brightness gas to the east and west. There is weak evidence for a projected velocity gradient.

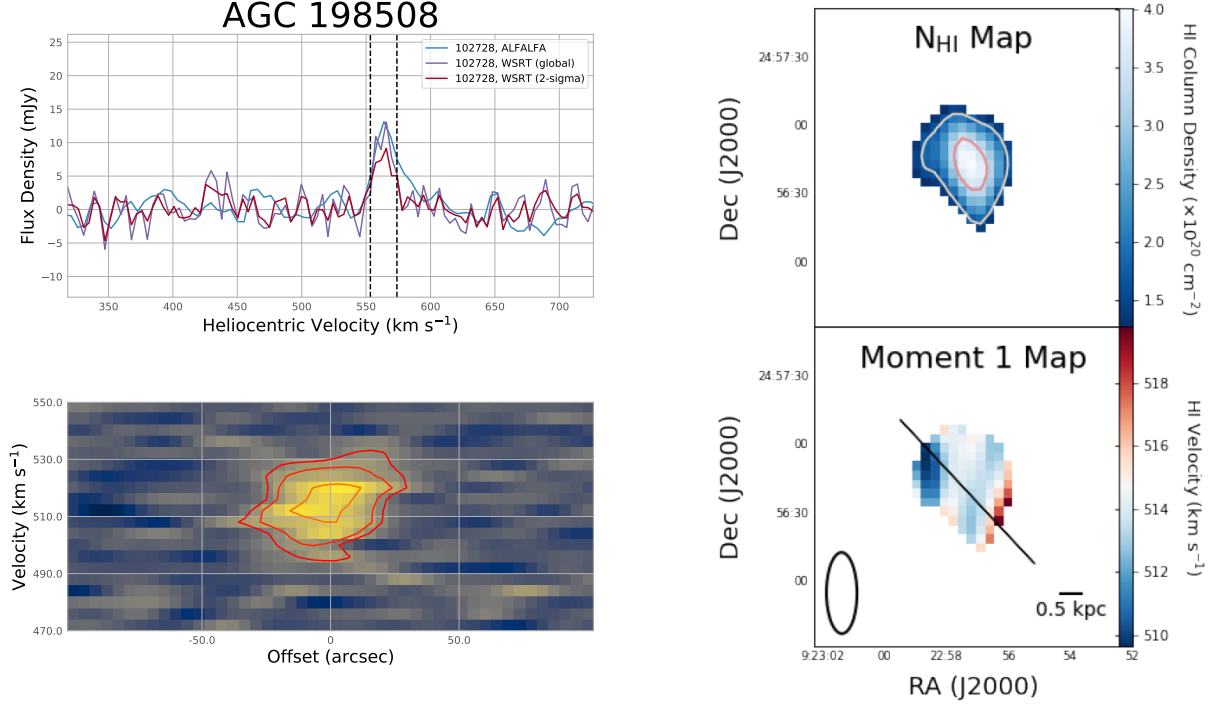


**Figure 16.** AGC 198508. There is a projected velocity gradient of  $10 \text{ km s}^{-1}$ .

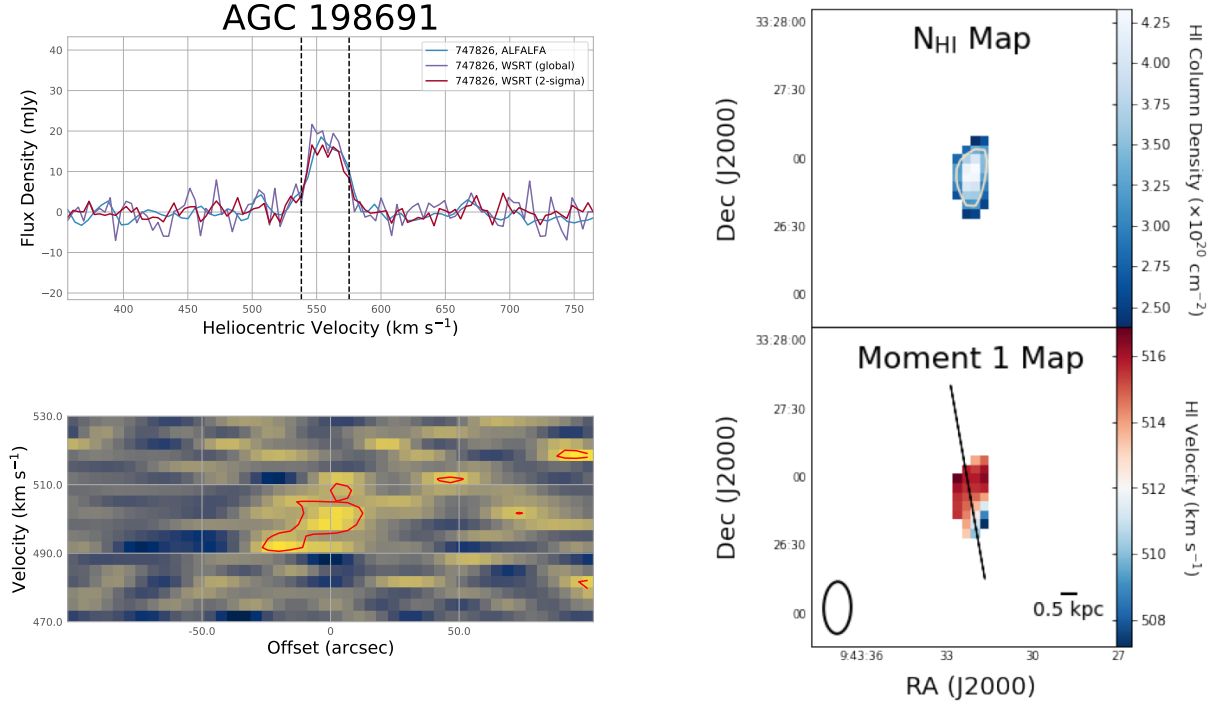


**Figure 17.** AGC 198691. The HI mass surface density is co-spatial with the stellar population of the source (for details see [McQuinn et al. 2020](#)). These WSRT images show no clear projected velocity gradient and suggest the presence of low surface density HI gas in the outskirts of the galaxy. Deep VLA HI images of this galaxy will be presented in Cannon et al. (in preparation).



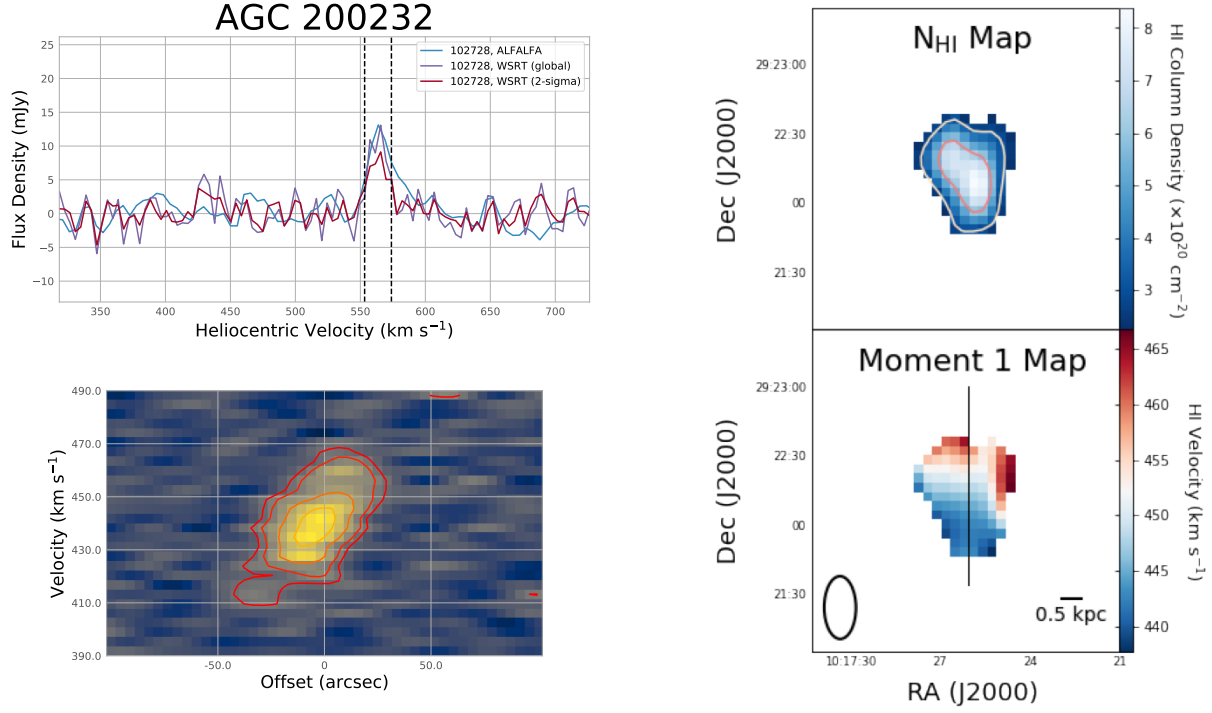


**Figure 18.** AGC 200232. There is a projected velocity gradient from south to north with a magnitude of  $22 \text{ km s}^{-1}$ .

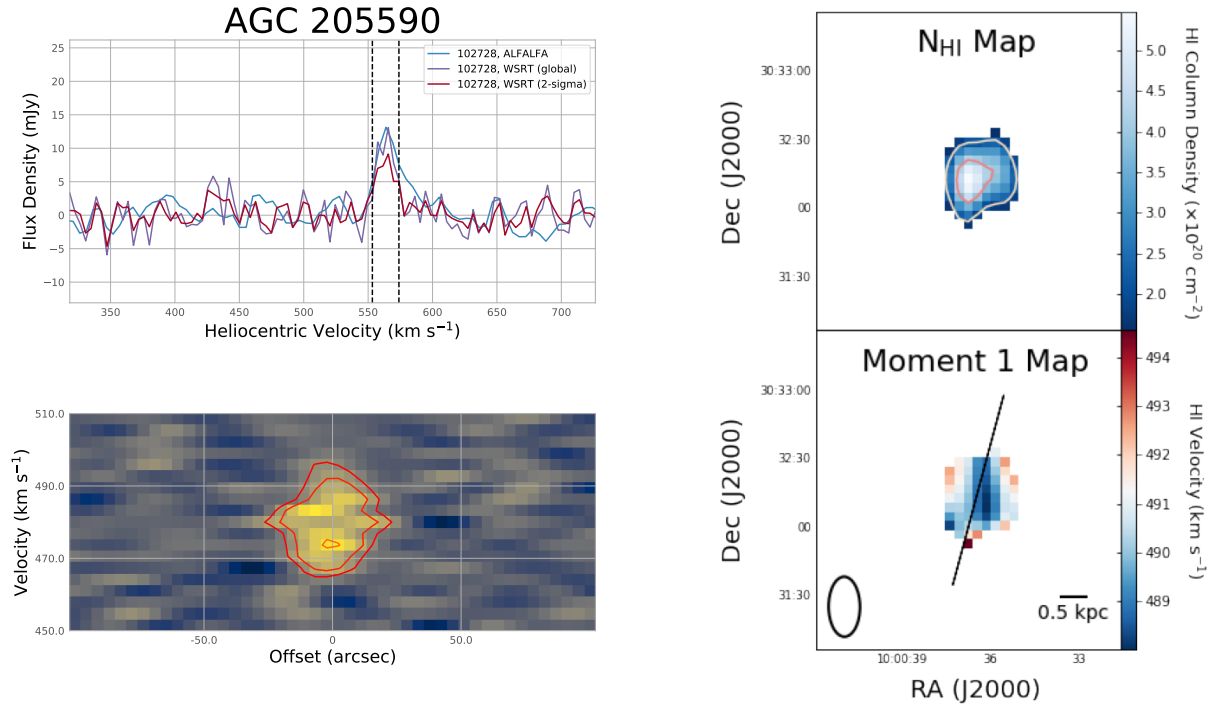


**Figure 19.** AGC 205590. There is a projected velocity gradient from south to north with a magnitude of  $5 \text{ km s}^{-1}$ .

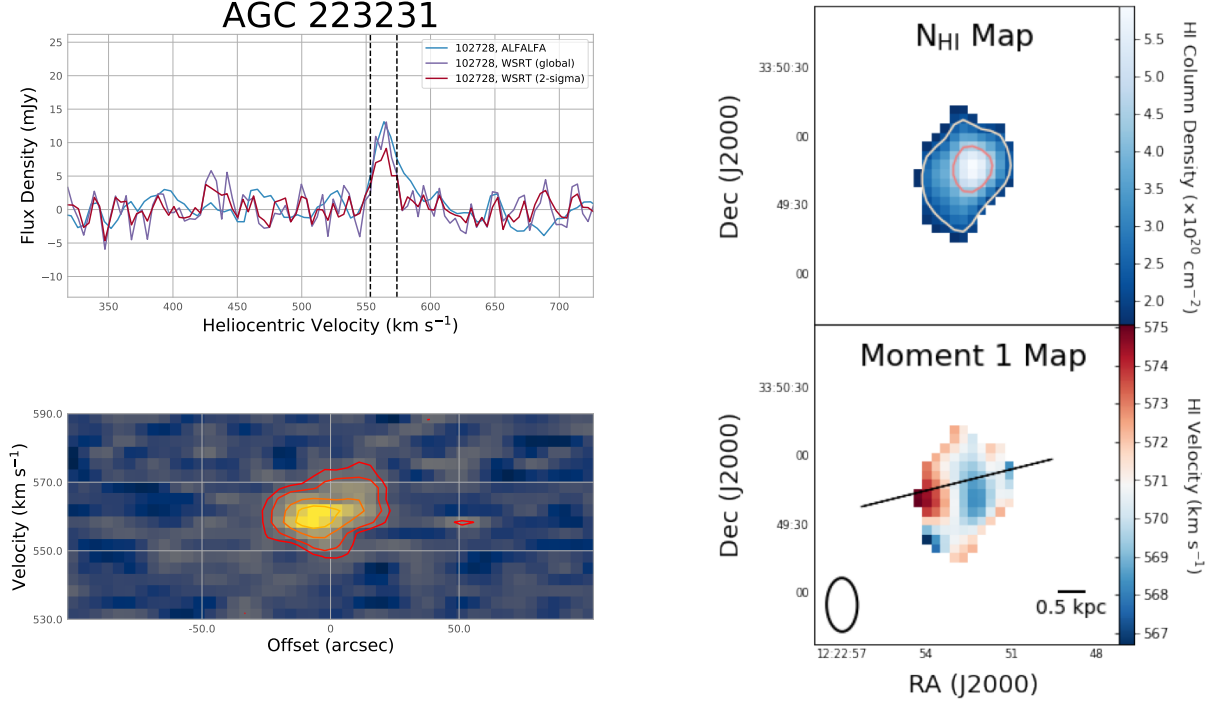


**Figure 20.** AGC 223231. While the source is resolved by the HI beam and the HI mass surface density maximum exceeds  $5 \times 10^{20} \text{ cm}^{-2}$ , there is only weak evidence for a coherent projected velocity gradient of  $4 \text{ km s}^{-1}$ .

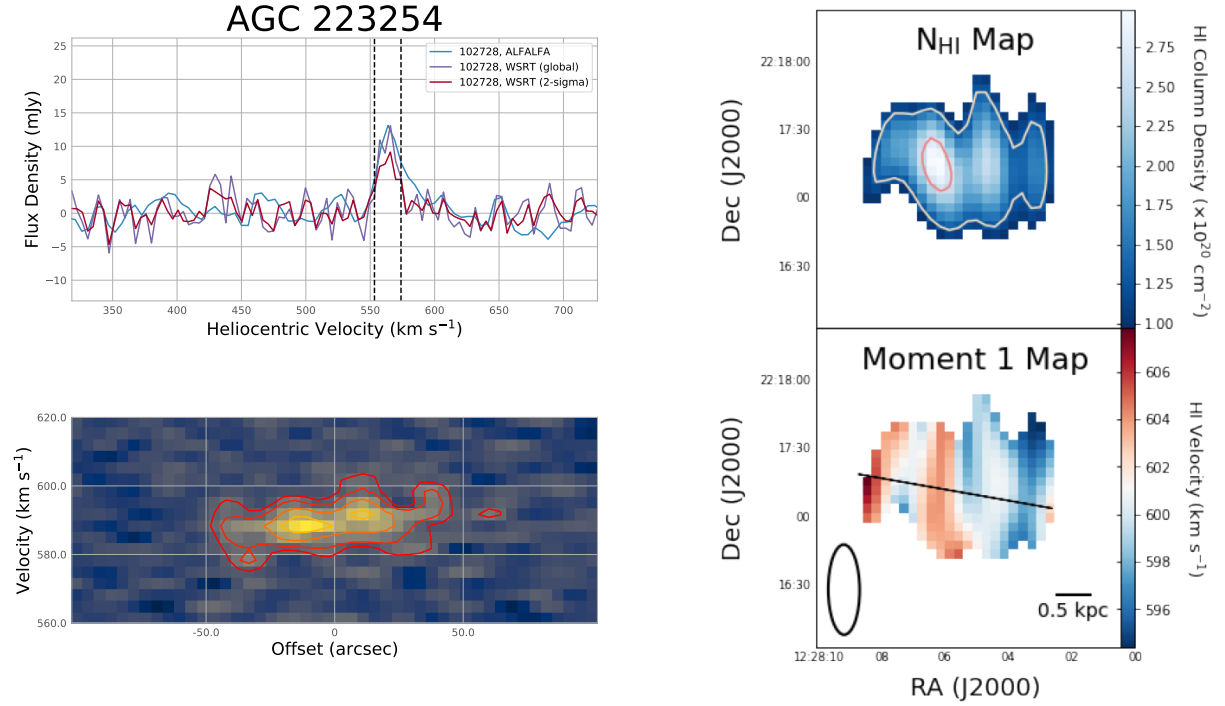


**Figure 21.** AGC 223254. There is a clear projected velocity gradient from west to east with a magnitude of  $9 \text{ km s}^{-1}$ .

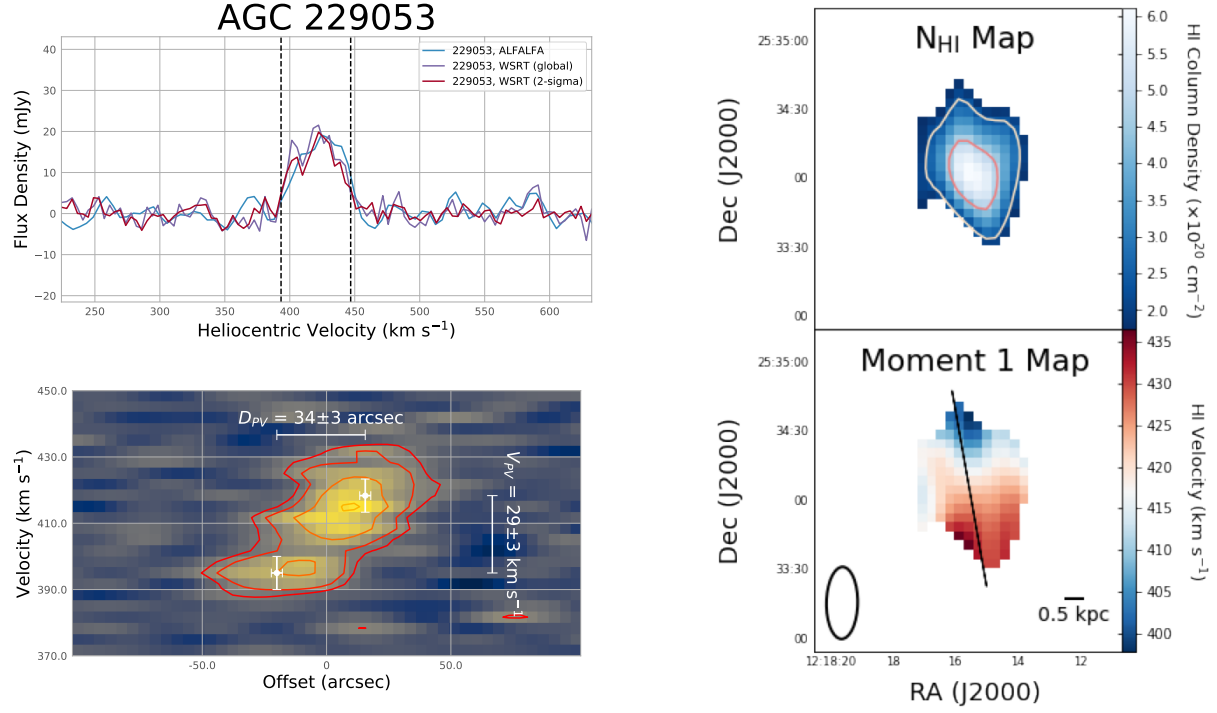


**Figure 22.** AGC 229053. There is a projected velocity gradient from north to south with a magnitude of  $29 \text{ km s}^{-1}$ .

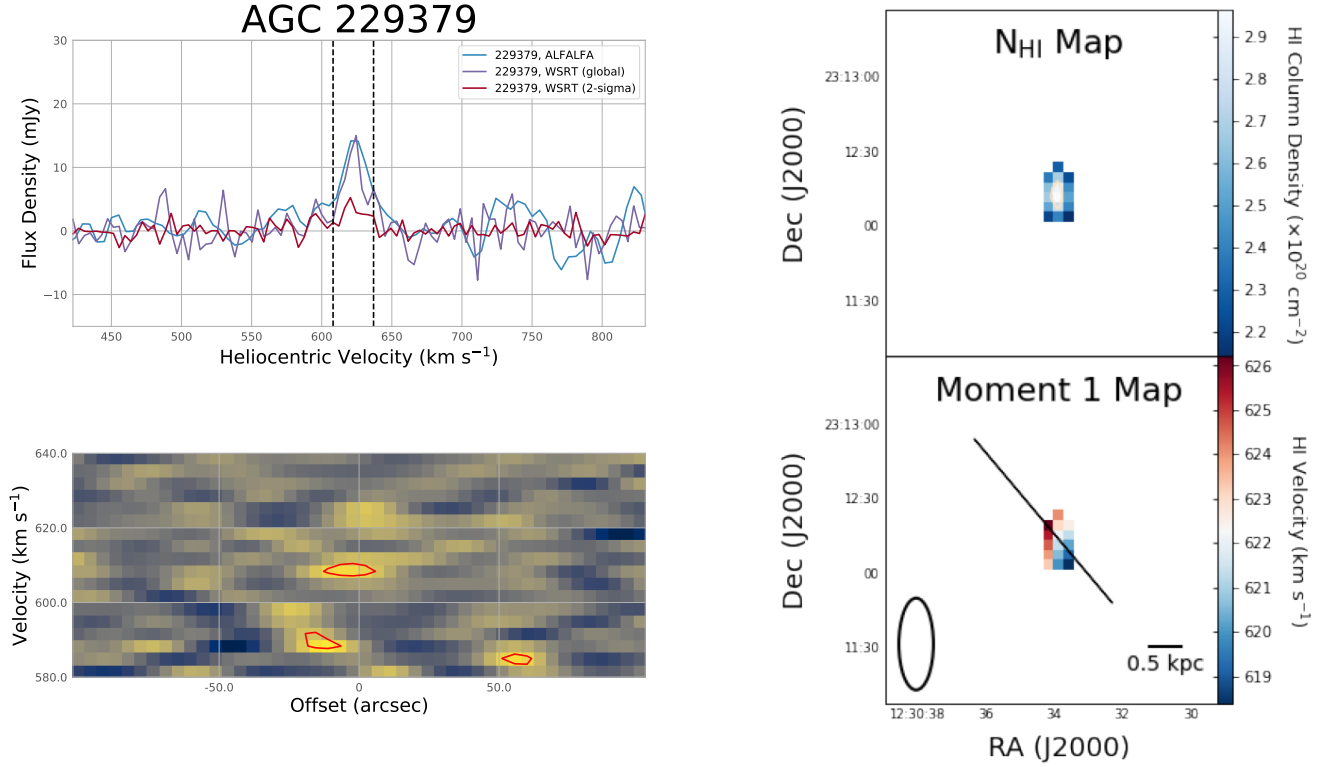


**Figure 23.** AGC 229379. This source is detected at low S/N; there is no evidence for a clear projected velocity gradient.

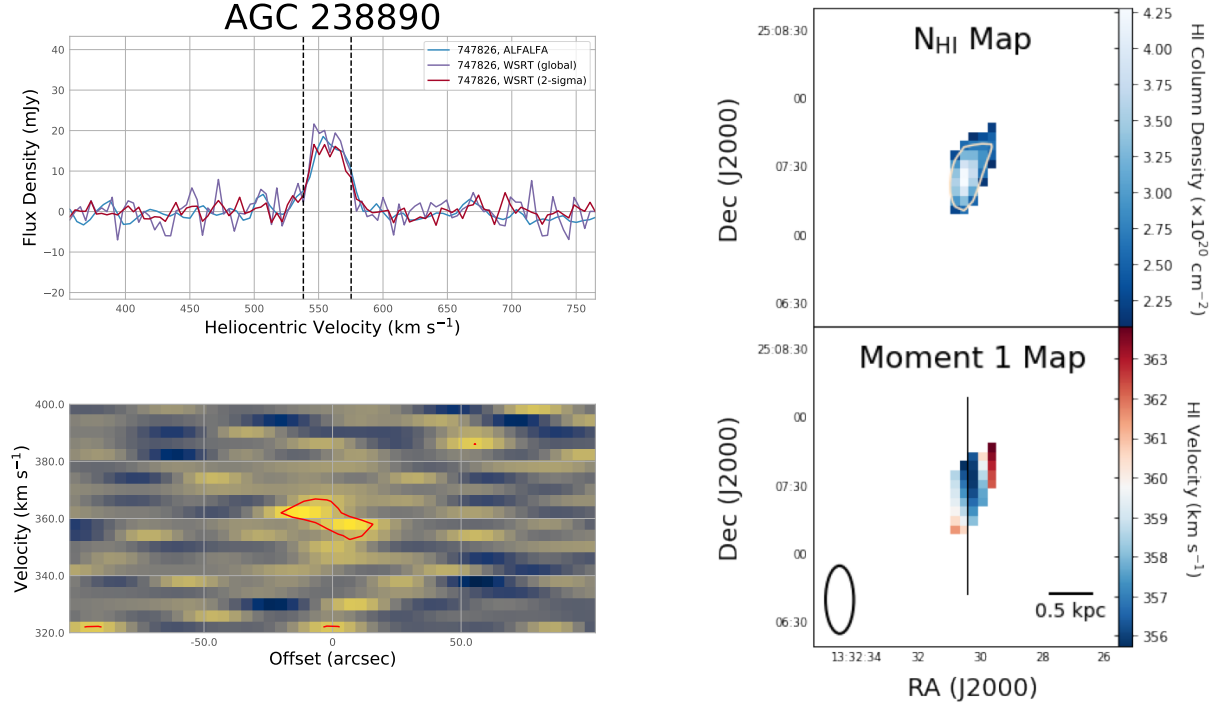


**Figure 24.** AGC 238890. There is no clear projected velocity gradient, and the source is only marginally resolved by the HI beam.

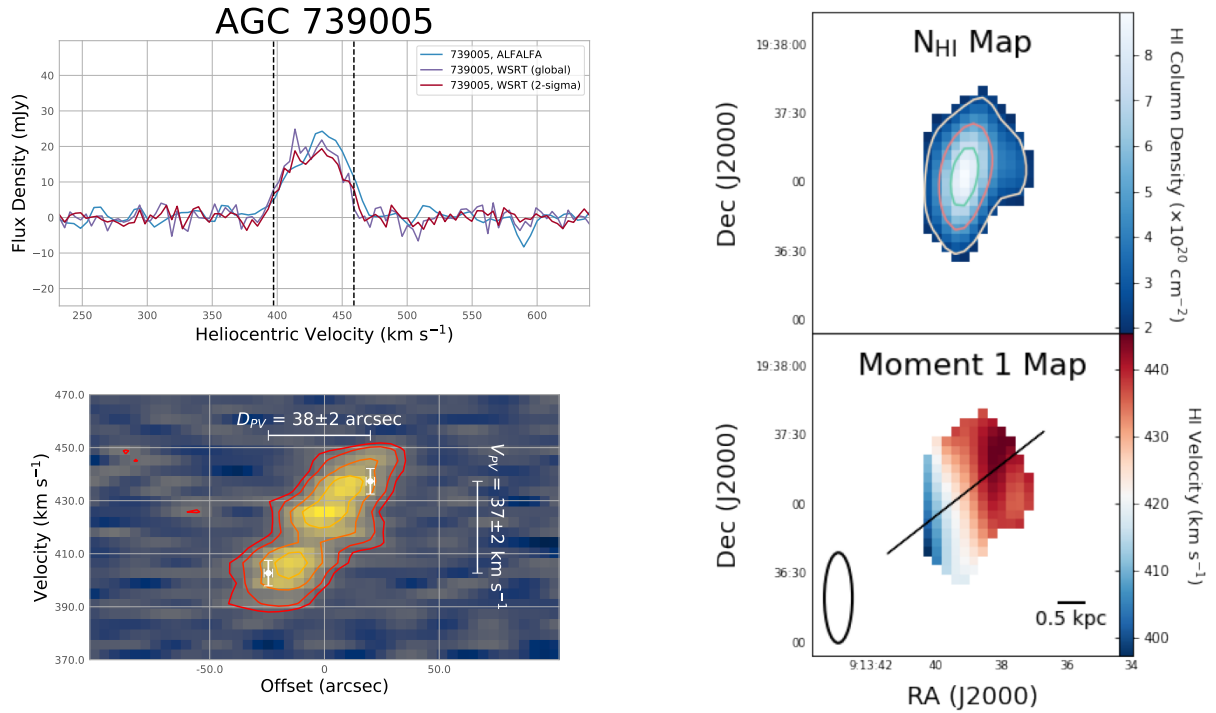


**Figure 25.** AGC 739005. There is a clear projected velocity gradient from east to west with a magnitude of 36 km s<sup>-1</sup>.



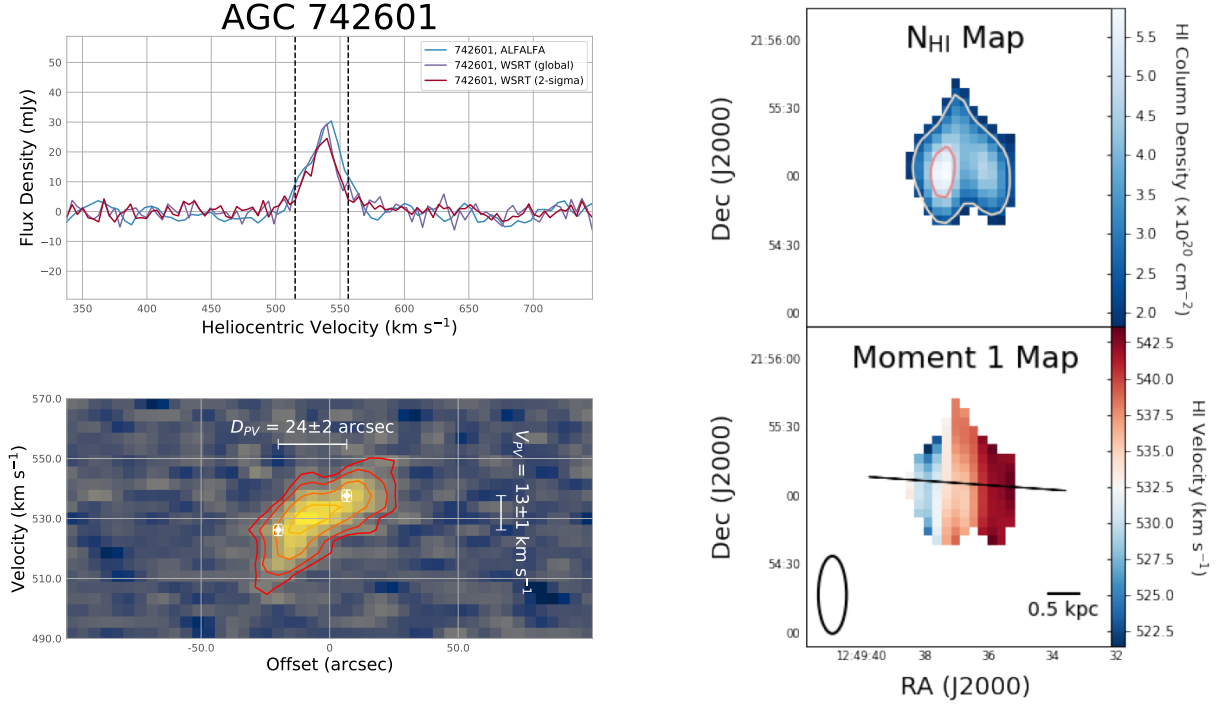


**Figure 26.** AGC 742601. There is a clear projected velocity gradient from east to west with a magnitude of 12 km s<sup>-1</sup>.

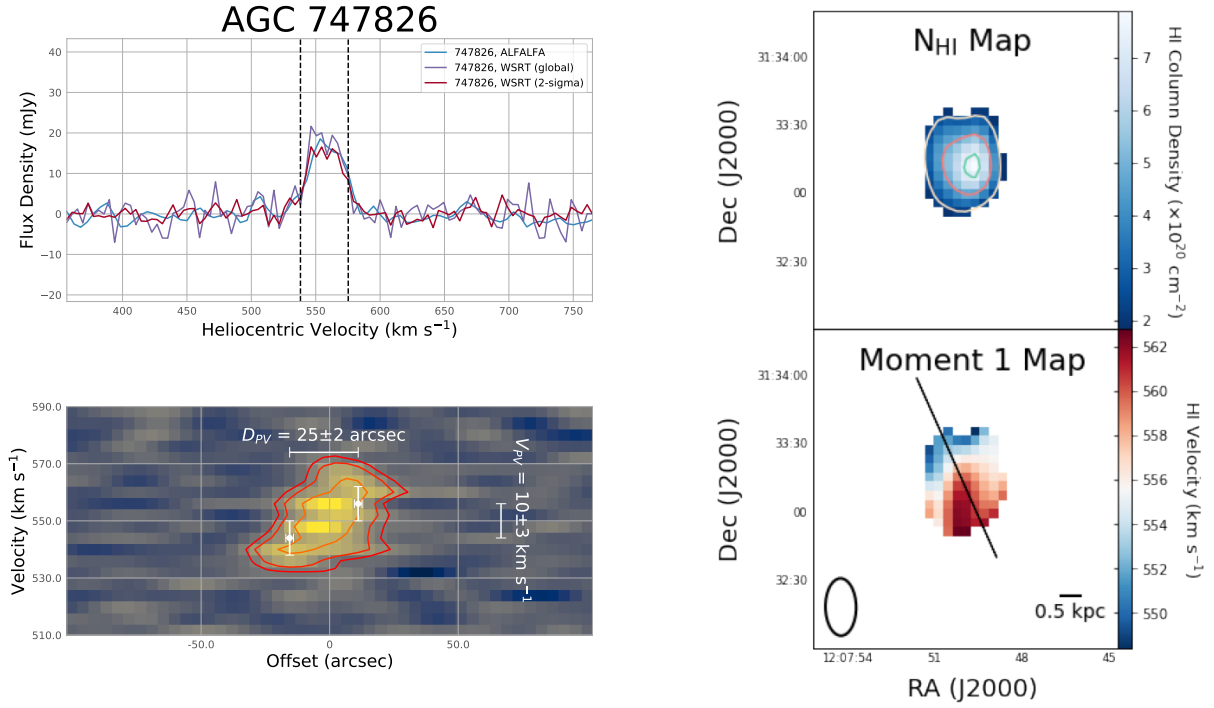


**Figure 27.** AGC 747826. There is a clear projected velocity gradient from east to west with a magnitude of 10 km s<sup>-1</sup>.

### C. A NOVEL APPROACH FOR ROBUST MAXIMUM VELOCITY AND EXTENT DETERMINATIONS FROM POSITION-VELOCITY SLICES

We have developed a new methodology for robustly constraining the maximum velocity and spatial extent from position-velocity (PV) slices. The idea behind using PV slices is to take advantage of the information available in resolved HI data to provide a better estimate of rotation velocity and the physical extent at which it is measured when modelling a rotation curve from a velocity field is problematic, for example, due to limited spatial sampling and/or in cases where the gas rotational motion is comparable to the dispersion. This new methodology fits Gaussians to orthogonal samples from the PV diagrams to derive maximum velocity and spatial extents, based on the centroid of the Gaussian in different bins. The goal of developing this new methodology was three-fold:

1. Provide a robust measure of the maximal velocities and positions of the HI gas: The previous methodology applied to SHIELD I galaxies in [McNichols et al. \(2016\)](#) visually determined the maximum velocity extent that contained emission within the  $2\text{-}\sigma$  level in a PV slice; however, this method conflates the velocity dispersion in the gas with the rotational velocity motion. While dispersion support is important in dwarf galaxies, our new method of fitting the centroid of emission returns a velocity measure that is conceptually more similar to a rotation velocity, where an asymmetric drift correction can then be applied.
2. Provide a method where the results are reproducible: The previously used methodology is responsive to the sensitivity of the data and the subjective determination of the extent. Thus, with different data quality, the results are not necessarily reproducible.
3. Provide a meaningful error on the values of the maximal velocities and positions of the HI gas: Fitting a function to the data allows the opportunity to return an error on the accuracy of the fit, providing meaningful uncertainties.

Below, we briefly describe this new methodology. J. Fuson et al. (in preparation) will present a detailed comparison of this methodology to values derived from kinematic modelling and analyze its overall effectiveness as an estimate of rotation velocity and extent. They will also present the code used to undertake this fitting.

#### C.1. *Deriving the velocity extent*

In order to derive the maximum velocity extent, the PV diagram is binned along the offset axis. The binning is specified by the user in arcseconds and rounded down to a unit number of pixels for numerical ease. A bin is considered eligible for fitting if the maximum value of the velocity spectrum is at least 3 times the rms. This cut-off level was determined through experimentation and comparison with well-determined velocity fields. In cases meeting this criterion, a Gaussian is fit using a Markov Chain Monte Carlo (MCMC) approach implemented via the `emcee` functionality in the `lmfit` python module. The center of the Gaussian is taken as the velocity of the gas in that offset bin. The MCMC approach allows a derivation of uncertainties on the accuracy of the fitting.

The left panels of Figures 28 and 29 shows the results of fitting the velocity in this way for two example cases. The velocity extent is determined as the difference between the minimum and maximum velocity values fitted along the offset axis, which we label  $V_{PV}$ . The uncertainty in  $V_{PV}$  is a combination of the reported uncertainties in the center of the Gaussian fits for the minimum and maximum velocity values. The rotational velocity of the gas can then be determined from half of the value of  $V_{PV}$  corrected for inclination (i.e.,  $V_{\text{rot}} = \frac{1}{2} V_{PV} / \sin i$ ). Note that one shortcoming of this approach is that rotational velocities determined from  $V_{PV}$  will not account for asymmetries in a velocity field.

#### C.2. *Deriving the spatial extent*

The spatial extent is determined in an analogous way to the velocity extent, except that the slicing is done in the orthogonal direction, with bins along the velocity axis of the PV diagram. The binning is specified by the user in  $\text{km s}^{-1}$  and rounded down to a unit number of pixels for numerical ease. A bin is considered for fitting if the maximum value of the bin along the offset axis is at least 3 times the rms. In those cases, a Gaussian is fit as above, where the center of the Gaussian is taken as the offset extent for that velocity bin.

The right panels of Figures 28 and 29 shows the results of fitting the spatial position offset in this way for two example cases. The spatial extent corresponding to the measurement of  $V_{PV}$  is determined as the difference between the minimum and maximum offset values that are returned from the Gaussian fitting, which we label  $D_{PV}$ . The

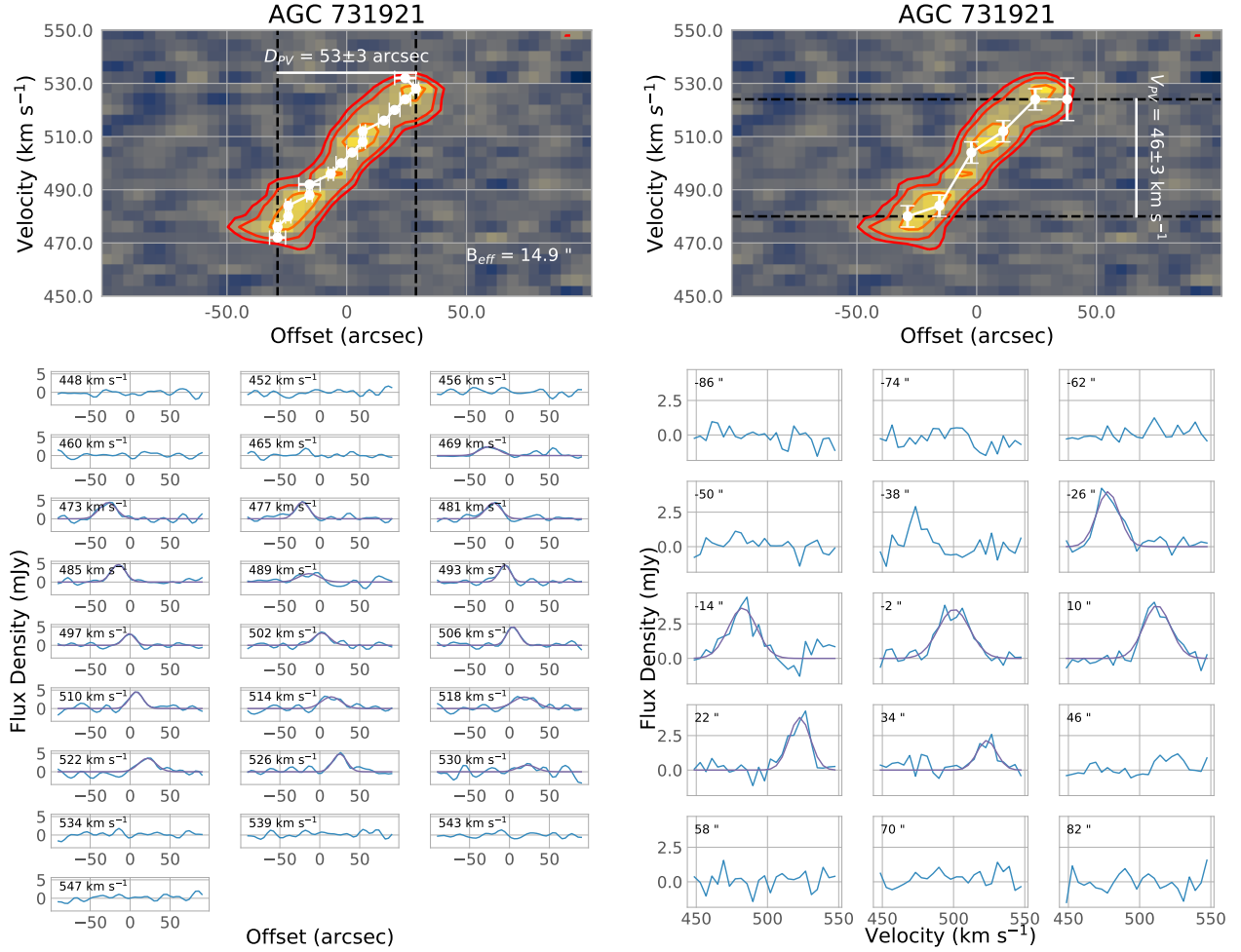


**Figure 28.** Examples of deriving the spatial (left) and velocity (right) extent for a well-resolved case (AGC 731921). Top panels: the PV diagrams overlaid with HI column density contours at the 2, 3, 5- $\sigma$  detection levels. The measured spatial and velocity extents are indicated on each panel with black dashed lines; final values of the velocity ( $V_{PV}$ ) and diameter ( $D_{PV}$ ), with uncertainties, as well as the calculated effective beam size ( $B_{eff}$ ) are also listed. Bottom panels: The "spectra" for each bin (blue), with Gaussian fits when the peak value is  $> 3 \times \text{rms}$  (purple). The location of each bin in velocity and spatial position offsets are marked with filled white circles in the top panels; uncertainties are based on the reported uncertainty in the fits to the center of the Gaussian.

uncertainty in  $D_{PV}$  is a combination of the reported uncertainties in the center of the Gaussian fits for the minimum and maximum offset values.

### C.3. Accepting a fit

A fit is only accepted if the derived spatial extent is at least as large as the effective beam across the PV diagram. Otherwise, the data is not well resolved and the fitting is considered not meaningful. In order to determine the effective resolution across the PV diagram, we first defined an effective position angle of the slice relative to the beam:

$$\phi = PA - B_{PA} \quad (C1)$$

where PA is the angle of the PV slice (listed in Table 3) and  $B_{PA}$  is the position angle of the restoring beam (listed in Table 2). Then, the effective diameter of the beam across the PV slice is:

$$B_{eff} = \sqrt{(B_{maj} \cdot \cos \phi)^2 + (B_{min} \cdot \sin \phi)^2} \quad (C2)$$

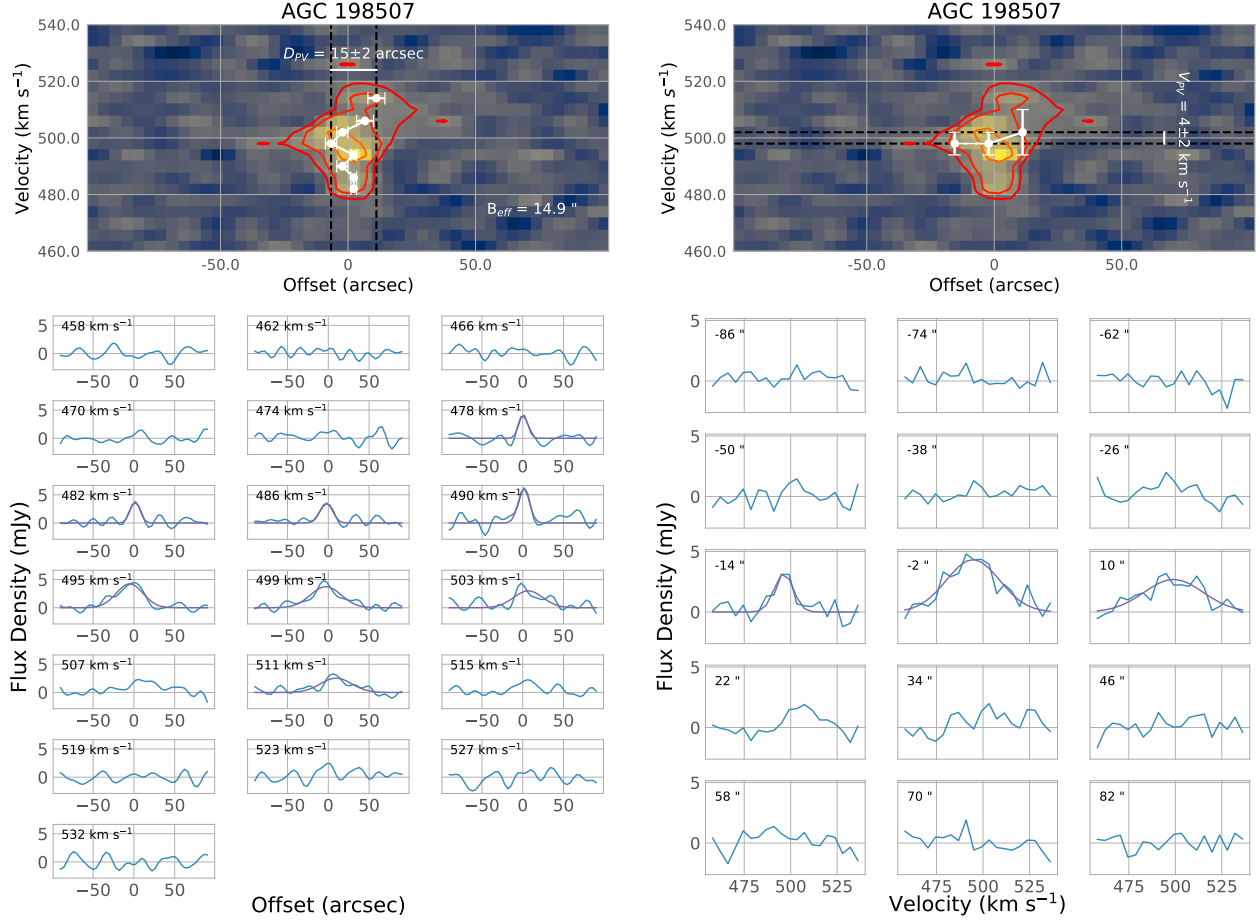


**Figure 29.** Examples of deriving the spatial (left) and velocity (right) extent for an unresolved case (AGC 198507). The format and labels are the same as in Figure 28. As the spatial position offset,  $D_{PV}$ , is less than the effective beam,  $B_{eff}$ , the measured velocity and spatial extents are not meaningful.

It is worth noting that in many cases when a galaxy is not resolved by this criterion, the returned velocity extent is also suspiciously small, i.e.,  $5 \text{ km s}^{-1}$  or less. This is consistent with the idea that the data are not resolved enough to provide meaningful measurements using this methodology. It could also be an indication that the smallest dwarf galaxies will always pose a challenge for meaningful measures of rotational velocity.

Figure 28 demonstrates a well-resolved case, where the derived values clearly track well with the PV emission. Figure 29 shows an unresolved case with the measured spatial extent less than the effective beam size; the results of the fitting are clearly not robust. In the latter case for AGC 198507, while we show the measured velocity and spatial extents, these are not well-measured values of the bulk motion of the gas or its extent and should not be used as representative kinematic information. New VLA observations in the B configuration have recently been obtained on a subset of the full SHIELD sample; we expect these higher resolution data will enable rotational velocities and spatial extents of the HI to be measured with confidence for a higher fraction of SHIELD galaxies using our new technique (VLA Large Program 20a-330; PI Cannon).

#### C.4. Application to the SHIELD II galaxies

The PV slices used to derive velocities and extents for the SHIELD II galaxies are described in Section 3.3 and presented in Appendix B. The offset binning used for the derivation of the maximum velocity extent is  $12''$ , slightly smaller than the WSRT minor axis HI beam size. The velocity binning used for deriving the spatial extent is  $8 \text{ km s}^{-1}$ , which is approximately the intrinsic velocity dispersion. AGC 223254 was excluded a priori from the derivation of velocity and spatial extents as both its velocity field and PV diagram indicate a disordered system. Three SHIELD II galaxies (AGC 198691, AGC 229379, AGC 238890) were not fit as they have insufficient S/N in at least two bins for

each slicing direction. We rejected the fits for seven SHIELD II galaxies (AGC 102728, AGC 123352, AGC 198507, AGC 198508, AGC 200232, AGC 205590, AGC 223231) as the derived extent is not resolved along the PV slice direction. It is worthwhile to note that some of these latter systems are close to being resolved and appear to have well-behaved fits; with higher quality, namely higher spatial resolution data, we expect to be able to robustly derive velocity and spatial extents from the PV diagrams.

### C.5. Application to the SHIELD I galaxies

New PV slices were created for the SHIELD I galaxies from the data presented in McNichols et al. (2016). Shown in Figures 30 & 31, these new PV slices have the same center and angle as those given in McNichols et al. (2016), but the width is  $50''$ , to be analogous to the PV slices derived for SHIELD II (see Section 3.3.)

The offset binning used for the derivation of the maximum velocity extent is  $12''$ , which is roughly the typical SHIELD I beam size and is consistent with the binning use for the SHIELD II galaxies. The velocity binning used for deriving the spatial extent is  $8 \text{ km s}^{-1}$ , which is approximately the intrinsic velocity dispersion. When the derived velocity and spatial extents are robustly derived, we overplot these values on the PV diagrams in Figures 30 & 31. Four SHIELD I galaxies (AGC 182595, AGC 731457, AGC 748778, AGC 749241) were not fit as there was insufficient S/N in our required minimum of two bins for each slicing direction. We rejected the fits for three SHIELD I galaxies (AGC 111946, AGC 111977, AGC 174585) as the measured spatial extents were not resolved.

### C.6. Comparison to ALFALFA velocity widths

As a verification of this new approach, we undertook a comparison of our measured velocity extents,  $V_{PV}$ , to the HI velocity widths from the ALFALFA data,  $W_{50}$ . Figure 32 shows this comparison, with sources color-coded by whether their measured spatial extent is resolved or unresolved; the disorder system AGC 223254 is noted separately. While we do not report the velocities fit for the unresolved cases, we included them here for completeness. A one-to-one comparison is shown as a solid line; it is evident that velocity extents measured with our new methodology are systematically smaller than the ALFALFA  $W_{50}$  values. This is to be expected given that the measured velocity widths include both the rotational velocity motion and the velocity dispersion of the gas. To account for this, we calculated the relationship between the measured velocity width, the velocity extent, and the velocity dispersion assuming that these values are all well-represented by Gaussians in the low-mass dwarf regime where both  $W_{50}$  and  $V_{PV}$  measure the full-width at half-maximum of their respective Gaussians. Specifically:

$$\sigma_{W_{50}}^2 = \sigma_{V_{PV}}^2 + \sigma_{disp}^2 \quad (\text{C3})$$

This relationship is represented as a dashed line in Figure 32 for a typical velocity dispersion of  $8 \text{ km s}^{-1}$ ; the lower and upper bounding dotted lines are for  $\sigma_{disp}$  values of 6 and  $10 \text{ km s}^{-1}$ , respectively. The fiducial line for a dispersion of  $8 \text{ km s}^{-1}$  nicely provides an upper limit to our measured values, indicating our measured velocity extents are consistent with the single-dish  $W_{50}$  values. As our velocity values are measured at a limited spatial extent whereas the  $W_{50}$  values include all the emission from the galaxies, it is not surprising that in many cases our values are below the line. This is especially worth keeping in mind for the galaxies where the spatial extents are smaller than the effective beam (i.e., the unresolved cases shown in orange).



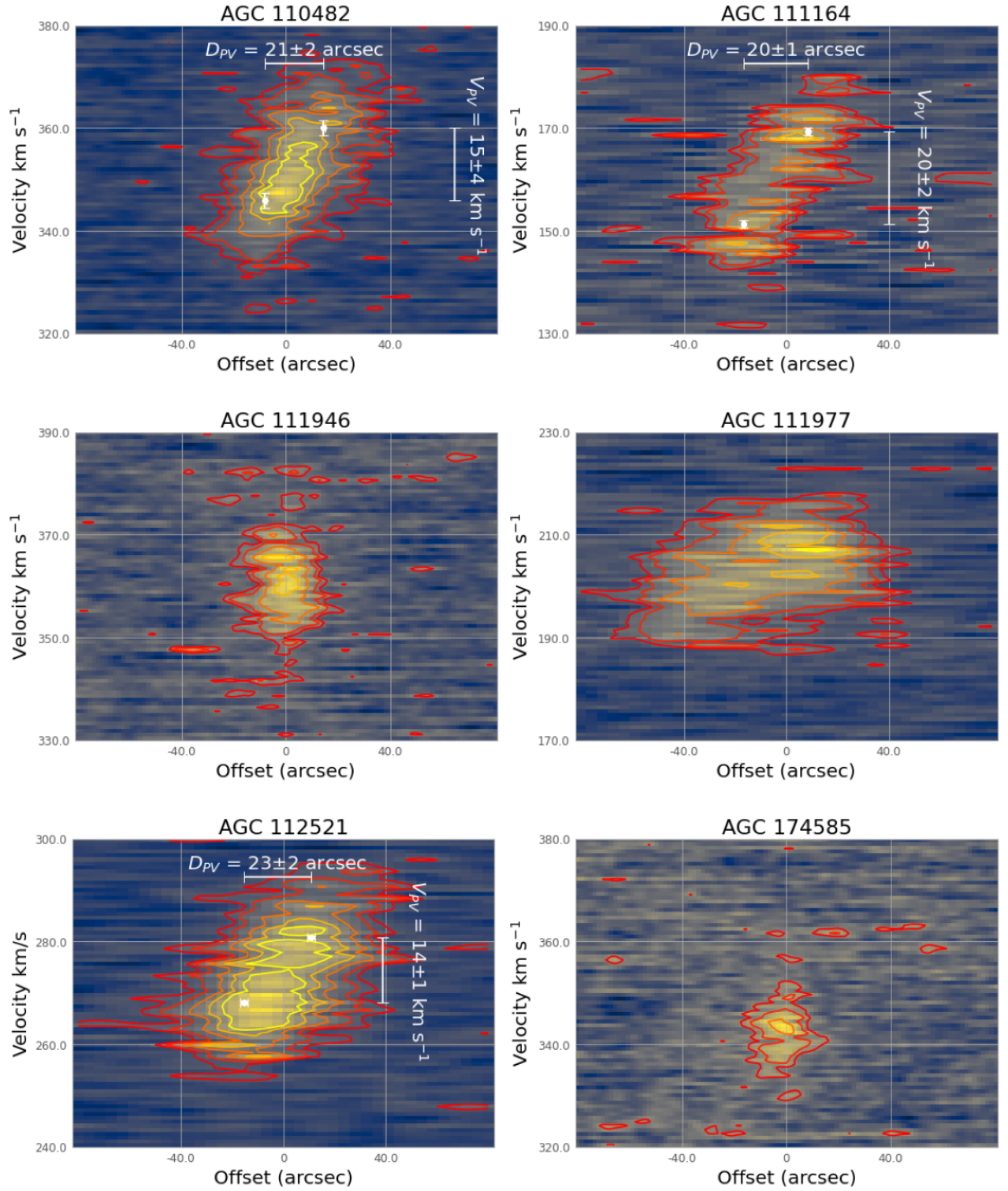


**Figure 30.** PV diagrams for six of the twelve SHIELD I galaxies, derived as described in C.5. The newly derived velocity and spatial extents are shown for the galaxies which meet our criteria for robustly derived values.

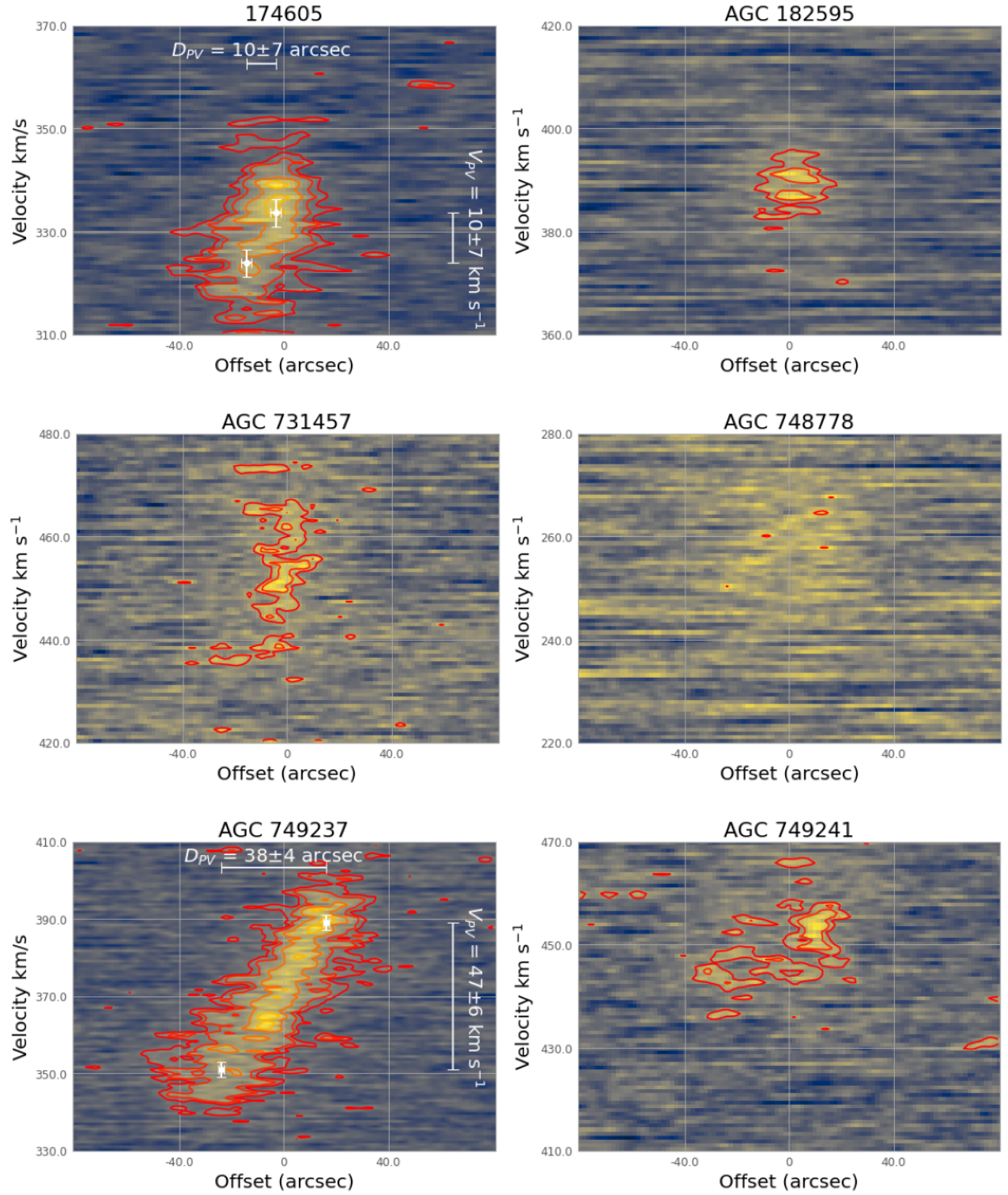


**Figure 31.** PV diagrams for the remaining six SHIELD I galaxies, derived as described in C.5. The newly derived velocity and spatial extents are shown for the galaxies which meet our criteria for robustly derived values.

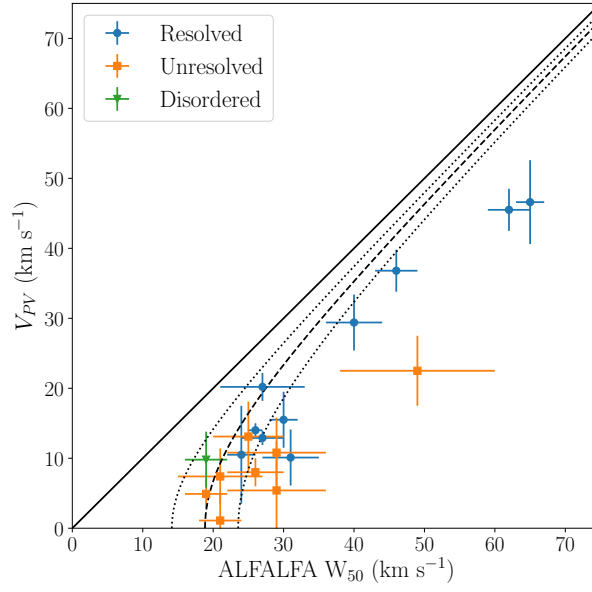


**Figure 32.** The velocity extents,  $V_{PV}$ , derived here compared to the velocity widths measured from single-dish observations, ALFALFA  $W_{50}$ . The solid line indicates the one-to-one relation, the dashed line indicates the relation accounting for an intrinsic velocity dispersion value of  $8 \text{ km s}^{-1}$ , and the lower and upper bounding dotted lines show the range assuming velocity dispersion values of  $6$  to  $10 \text{ km s}^{-1}$  respectively. See text for details.